Title
Boron-rich Clusters as Molecular Cross-linkers for Hierarchical Hybrid Materials

Author
Jung, Dahee

Publication Date
2019

UNIVERSITY OF CALIFORNIA

Los Angeles

Boron-rich Clusters as Molecular Cross-linkers for Hierarchical Hybrid Materials

A dissertation submitted in partial satisfaction of the

requirements for the degree Doctor of Philosophy

in Chemistry

by

Dahee Jung

2019

ABSTRACT OF THE DISSERTATION

Boron-rich Clusters as Molecular Cross-linkers for Hierarchical Hybrid Materials

by

Dahee Jung

Doctor of Philosophy in Chemistry

University of California, Los Angeles, 2019

Professor Alexander Michael Spokoyny, Chair

Covalent cross-linking plays an important role for materials to form robust networks with enhanced thermal/mechanical properties compared to pristine materials. However, there are a limited number of cross-linkers that can produce rigid 3-dimensional networks, leading to significant modifications of properties in materials. Our group has developed a "molecular cross-linking" approach whereby perhydroxylated dodecaborate clusters ($[B_{12}(OH)_{12}]^{2-}$) are incorporated in the network of metal oxides to create hierarchical hybrid materials. These clusters, capable of withstanding harsh thermal and oxidizing conditions required for the synthesis of many metal oxides, allow the formation of hybrid metal oxides. We showcase how the robust $[B_{12}(OH)_{12}]^{2-}$ cluster can be successfully cross-linked with TiO_2 with dramatically altered photo-physical and electrochemical properties. The comprehensive structural characterization of this material reveals the formation of a hybrid molecular boron oxide material that consists of a cross-linked network of intact boron clusters and TiO_2 nanocrystals in the anatase phase. The unique structure of this hybrid metal oxide consequently engenders unprecedentedly superior electro- and photochemical properties than that of pristine TiO_2. Furthermore, we expand this molecular cross-linking approach to other metal oxides such as WO_3 for energy storage applications.

In addition, we explore the possibility to cross-link $[B_{12}(OH)_{12}]^{2-}$ clusters to organic monomers to create densely cross-linked polymeric materials. We found out the molecular boron-rich cluster can act as an inorganic polyol equivalent in the synthesis of polyurethane-based materials, serving as a molecular cross-linker. We highlight incorporating $[B_{12}(OH)_{12}]^{2-}$ building blocks can effectively improve the thermal stability of the resultant polyurethane materials compared to analogous polymers made from carbon-based polyols. The successful modification of the materials ranging from inorganic metal oxides to organic polymeric materials highlights the value of molecular cross-linking as a noble strategy to alter the properties of materials for diverse applications.

The dissertation of Dahee Jung is approved.

Yongjie Hu

Richard B. Kaner

Jeffrey I. Zink

Alexander Michael Spokoyny, Committee Chair

University of California, Los Angeles

2019

DEDICATION

I love you Lord, my strength.

TABLE OF CONTENTS

CHAPTER 1. BACKGROUND: CROSS-LINKING DOTS ON HYBRID MATERIALS

CHAPTER 2. A MOLECULAR CROSS-LINKING APPOACH FOR HYBRID METAL OXIDES MATERIALS

CHAPTER 3. CROSS-LINKED TUNGSTEN OXIDES FOR ENERGY STORAGE APPLICATIONS

CHAPTER 4. CROSS-LINKED POROUS POLYURETHANE MATERIALS FEATURING DODECABORATE CLUSTERS AS INORGANIC POLYOL EQUIVALENTS

LIST OF FIGURES

CHAPTER 1. BACKGROUND: CROSS-LINKING DOTS ON HYBRID MATERIALS

CHAPTER 2. A MOLECULAR CROSS-LINKING APPROACH FOR HYBRID METAL OXIDES

CHAPTER 3. CROSS-LINKED TUNGSTEN OXIDES FOR ENERGY STORAGE APPLICATIONS

CHAPTER 4. CROSS-LINKED POROUS POLYURETHANE MATERIALS FEATURING DODECABORATE CLUSTERS AS INORGANIC POLYOL EQUIVALENTS

LIST OF TABLES

CHAPTER 1. BACKGROUND: CROSS-LINKING DOTS ON HYBRID MATERIALS

ACKNOWLEDGEMENTS

I would like to appreciate my advisor, Professor Alexander M. Spokoyny, for his intellectual guidance and generous support throughout my PhD studies. I also thank the Spokoyny group members for being good friends in the U.S. A special gratitude goes to Dr Liban M. A. Saleh who was patiently waiting until I got used to performing research and provided me with priceless advice in PhD life. I am also grateful to Dr Johnny W. Pang who trusted in me as a teaching assistant. I appreciate Kyung Seo Church members in Korea for their endless support and prayer for me. I thank University Presbyterian Church members for their encouragement and prayers. A special mention goes to Dr Ignacio Martini and Ivo Atanasov who helped me a lot use all kinds of instruments in UCLA and not being mad whenever I did something wrong. I would like to thank my family: my parents (Jong Hoon Jung and Sun Ja Park) and to my sister (Saet Byeol Jeong) for their financial and emotional support and encouragement so that I can complete my degree without any worries. Last but not least, I would like to express my special gratitude to Kyungin Nam, who has shown his unconditional love and endless support to me.

PREVIOUS PUBLICATION AND CONTRIBUTIONS OF CO-AUTHORS

Chapter 1 is a version of Roshini Ramachandran, Dahee Jung, and Alexander M. Spokoyny, "Crosslinking Dots on Metal Oxides." R.R., D.J., and A.M.S. co-wrote the manuscript.

Chapter 2 is a version of Dahee Jung, Liban M. A. Saleh, Zachariah J. Berkson, Maher F. El-Kady, Jee Youn Hwang, Nahla Mohamed, Alex I. Wixtrom, Ekaterina Titarenko, Yanwu Shao, Kassandra McCarthy, Jian Guo, Ignacio B. Martini, Stephan Kraemer, Evan C. Wegener, Philippe Saint-Cricq, Bastian Ruehle, Ryan R. Langeslay, Massimiliano Delferro, Jonathan L. Brosmer, Christopher H. Hendon, Marcus Gallagher-Jones, Jose Rodriguez, Karena W. Chapman, Jeffrey T. Miller, Xiangfeng Duan, Richard B. Kaner, Jeffrey I. Zink, Bradley F. Chmelka and Alexander M. Spokoyny, "A Molecular Cross-linking Approach for Hybrid Metal Oxides." A.M.S. developed the concept of molecular cross-linking and supervised the project. D.J., L.M.A.S and A.M.S. co-designed the experiments; D.J. and L.M.A.S performed the synthetic experimental work; D.J. performed the majority of the structural characterization and data analysis. Z.J.B. and B.F.C. designed, conducted, and interpreted the solid-state NMR experiments and data. M.F.E-K, J.Y.H and, N.M performed the electrochemical studies and interpreted the data with R.B.K. D.J., L.M.A.S, E.K., Y.S. and K. M. performed the dye degradation experiments. A.I.W. performed the EPR measurements. J.G. performed the resistivity measurements and interpreted the data with X.D. I.B.M. performed the SQUID measurements. S.K. designed and performed the STEM measurements. E.C.W. performed the XANES and EXAFS measurements and analyzed the data with J.T.M. P.S-.C. and B.R performed the mechanistic photochemical work and analyzed the data with J.I.Z. R.R.L. and M.D. performed the TGA-MS and TPD ammonia experiments. J.L.B. performed the Raman spectroscopic measurements. C.H.H. performed the computational modeling. M.G-J. and J.R performed the TEM measurements and created the 3D reconstruction. K.W.C. collected the high energy X-ray scattering data and interpreted the data. D.J., L.M.A.S., A.M.S., Z.J.B., and

B.F.C. co-wrote the manuscript. All authors discussed the results and commented on the manuscript during its preparation.

Chapter 3 is a work of Dahee Jung, Gustavo Marin, Roshini Ramachandran, Mit Muni, Maher F. El-Kady, Richard B. Kaner, and Alexander M. Spokoyny. D.J. and G.M. performed the synthesis and characterizations of the material. D.J., G.M., and R.R analyzed the data with A.M.S. M.M. and M.F.E-K. carried out the electrochemical measurements and interpreted the data with R.B.K.

Chapter 4 is a version of Dahee Jung, Fernando Raffan-Montoya, Roshini Ramachandran, Yuanyuan Zhang, Timur Islamoglu, Gustavo Marin, Elaine A. Qian, Rafal M. Dziedzic, Omar K. Farha, Stanislav I. Stoliarov and Alexander M. Spokoyny, "Cross-Linked Porous Polyurethane Materials Featuring Dodecaborate Clusters as Inorganic Polyol Equivalents." D.J. and A.M.S. co-designed the experiments and D.J. performed the synthesis and characterizations of the material. D.J., R.R., and G.M. analyzed the data with A.M.S. R-M. and S.I.S. designed the micro combustion calorimetry test and interpret the data. D.J and Y.Z performed the supercritical CO_2 drying and BET measurements and interpret data with T.I. and O.K.F. E.A.Q carried out ESI-MS. R.M. performed ^{13}C solution NMR experiments.

VITA

2011	B.S., Chemistry Sookmyung Women's University Seoul, Republic of Korea
2013	M.S., Chemistry Sookmyung Women's University Seoul, Republic of Korea
2015	M.S., Chemistry University of California, Los Angeles Los Angeles, California
2016	Ph.D. candidate in Chemistry University of California, Los Angeles Los Angeles, California

PUBLICATIONS

1. **Jung, D.**; Raffan-Montoya, F.; Ramachandran, R.; Zhang, Y.; Islamoglu, T.; Marin, G.; Qian, E. A.; Dziedzic, R. M.; Farha, O. K.; Stoliarov, S. I.; Spokoyny, A. M. "Cross-linked Porous Polyurethane Materials Featuring Dodecaborate Clusters as Inorganic Polyol Equivalents", *Chem. Commun. In press* (Special Issue on Emerging Investigators).
2. Barton, J.; Wixtrom, A. I.; Kowalski, J.; Qian, E. A.; **Jung, D.**; Brushett, F. R. Spokoyny, A. M. "Perfunctionalized Dodecaborate Clusters as Stable Metal-Free Active Materials for Charge Storage", *ACS Appl. Energy Mater. In Press.*
3. Ramachandran, R.; **Jung, D.**; Spokoyny, A. M. "Cross-Linking the Dots on Metal Oxides", *NPG Asia Mater.* **2019**, *11:*19.
4. Ramachandran, R.; **Jung, D.**; Bernier, N. A.; Logan, J. K.; Waddington, M. A.; Spokoyny, A. M. "Synthesis of Ultra-Small Boron Oxide Nanoparticles", *Inorg. Chem.* **2018**, *57, 8037-8041.*
5. Wixtrom, A. I.; Parvez, Z.; Savage, M. A.; Qian, E. A.; **Jung, D.**; Khan, S. I.; Rheingold, A. L.; Spokoyny, A. M. "Tuning the Electropotential of Perfunctionalized Dodecaborate Clusters Through Vertex Differentiation", *Chem. Commun.* **2018**, *54,* 5867-5870.
6. **Jung, D.**; Saleh, L. M. A.; Berkson, Z. J.; El-Kady, M. F.; Hwang, J. Y.; Mohamed, N.; Wixtrom, A. I.; Titarenko, E.; Shao, Y.; McCarthy, K.; Guo, J.; Martini, I. B.; Kraemer, S.; Wegener, E. C.; Saint-Cricq, P.; Ruehle, B.; Langeslay, R. R.; Delferro, M.; Brosmer, J. L.; Hendon, C. H.; Gallagher-Jones, M.; Rodriguez, J.; Chapman, K. W.; Miller, J. T.; Duan, X.; Kaner, R. B.; Zink, J. I.; Chmelka, B. F.; Spokoyny, A. M. "A Molecular Cross-Linking Approach for Hybrid Metal Oxides", *Nature Mater.* **2018**, *17*, 341-348. *Highlighted by Argonne National Lab, Chemistry World, C&EN, UCLA Newsroom, EurekaAlert, Materials Today, and PhysOrg.*

7. Kirlikovali, K. O.; Cho, E.; Downard, T. J.; Grigoryan, L.; Han, Z.; Hong, S.; **Jung, D.**; Quintana, J. C.; Reynoso, V.; Ro, S.; Shen, Y.; Swartz, K.; Ter Sahakyan, E.; Wixtrom, A. I.; Yoshida, B.; Rheingold, A. L.; Spokoyny, A. M. "Buchwald-Hartwig Amination Using Pd(I) Dimer Precatalysts Supported by Biaryl Phosphine Ligands", *Dalton Trans*. **2018**, *47,* 3684-3688.
8. Qian, E. A.; Wixtrom, A. I.; Axtell, J. C.; Saebi, A.; **Jung, D.**; Rehak, P.; Han, Y.; Moully, E. H.; Mosallaei, D.; Chow, S.; Messina, M.; Wang, J.-Y.; Royappa, A. T.; Rheingold, A. L.; Maynard, H. D.; Kral, P.; Spokoyny, A. M. “Atomically Precise Organomimetic Cluster Nanomolecules Assembled via Perfluoroaryl-Thiol SNAr Chemistry”, *Nature Chem*. **2017**, *9*, 333-340.
9. Axtell, J. C.; Kirlikovali, K. O.; **Jung, D.**; Dziedzic, R. M. Rheingold, A. L.; Spokoyny, A. M. "Metal-Free Peralkylation of the *closo*-Hexaborate Anion", *Organometallics* **2017**, *36*, 1204-1210.
10. Axtell, J. C.; Kirlikovali, K. O.; Djurovich, P. I.; **Jung, D.**; Nguyen, V. T.; Munekiyo, B.; Royappa, A. T.; Rheingold, A. L.; Spokoyny, A. M. "Blue Phosphorescent Zwitterionic Iridium(III) Complexes Featuring Weakly Coordinating Carborane-based Ligands", *J. Am. Chem. Soc.* **2016**, *138*, 15758-15765.
11. Wixtrom, A. I.; Shao, Y.; **Jung, D.**; Machan, C. W.; Kevork, S. N.; Qian, E. A.; Axtell, J. C.; Khan, S. I.; Kubiak, C. P.; Spokoyny, A. M. "Rapid Synthesis of Redox-Active Dodecaborane $B_{12}(OR)_{12}$ Clusters Under Ambient Conditions", *Inorg. Chem. Front.* (Emerging Investigator Issue) **2016**, *3*, 711-717.

PRESENTATIONS

- Oral Presentation: 10th International Mesostructured Materials Symposium, University of California, Los Angeles, September 10-13, **2018**. “A Molecular Cross-linking Approach for Hierarchical Hybrid Materials”
- Poster: Material Research Society Spring Meeting & Exhibit, Phoenix, April 2-6, **2018**. “A Molecular Cross-linking Approach for Hybrid Metal Oxides”
- Oral Presentation: 1st Annual Nelson/Spokoyny Main Group Symposium, Las Vegas, December 8-10, **2017**. “A Molecular Cross-linking Approach for Hybrid Metal Oxide Materials”
- Oral Presentation: ACS 253rd National Meeting, San Francisco, April 2-6, **2017**. “A Molecular Doping Approach for Hybrid Metal Oxide Materials”
- Poster: UCLA ACS Research Showcase, San Francisco, April 4, **2017**. “A Molecular Doping Approach for Hybrid Metal Oxide Materials”
- Poster: Seaborg Symposium, Los Angeles, November 12, **2016**. “Molecular Doping Approach for Hybrid Metal Oxide Sensitization”
- Oral Presentation: Southern California Inorganic Photophysics (SCIP), Catalina Island, September 16-18, **2016**. “Molecular Doping Approach for Metal Oxide Sensitization”
- Poster: University of California Symposium for Chemical Sciences (UCSCS), Lake Arrowhead, March 21-23, **2016**. “Hybrid Metal Oxides Featuring Robust Organomimetic Boron Clusters”
- Poster: Seaborg Symposium, Los Angeles, October 19, **2015**. “From UV to IR: Prodigious light absorption enhancement of titanium dioxide in a hybrid TiO_2/B_{12}-cluster material”

CHAPTER 1

BACKGROUND: CROSS-LINKING DOTS ON HYBRID MATERIALS

This chapter is a version of Ramachandran, R.; Jung, D.; Spokoyny, A. M. "Cross-Linking the Dots on Metal Oxides", *NPG Asia Mater.* **2019**, *11:*19.

Abstract

Metal oxides are ubiquitous in our daily lives as they are robust and possess versatile electrochemical properties. Despite their popularity, these materials present limitations with respect to effective large-scale implementation. Recently, there has been a growing interest in creating hybrid metal oxides to tailor the morphology and properties of these materials. In this perspective, we highlight several recent developments in cross-linked hybrid metal oxides, focusing on chemical cross-linking techniques to enrich their properties. We discuss future directions of this cross-linking approach that could enable elaborate manipulation of these materials further.

Article:

Earth-abundant metal oxides are materials whose versatile properties allow them to be utilized in applications ranging from energy storage to catalysis.[1,2] Despite decades of research surrounding this class of materials, new syntheses and applications are still emerging, including novel hybrid metal oxide materials. Through nanostructuring[3], fabricating composite materials[4], or introducing new surface modifications[5], a tremendous amount of work has been done on expanding the functionality of metal oxides. In the past year alone, 1055 scientific articles relating to hybrid metal oxides were published![6] Hybrid metal oxides present several notable advantages over their parent materials, one of which is the breadth of new processing options that emerge for these materials. Especially in the case of hybrid polymer-metal oxide materials, the flexibility of the polymer is imparted to the system which allows for facile processing into macrostructures.[7] Furthermore, the construction of hybrid metal oxides can be manipulated to fashion unique architectures on the nanoscale. Various metal oxide hybrids have been tailored with novel 2D and 3D morphologies that demonstrate superior properties (e.g., electrochemical activity) relative to their bulk counterparts.[1,8] However, there is still room for improvement to address critical issues, like low electrical conductivity, poor ion transport, and lack of homogeneity, before metal oxides can be implemented on a large scale. In this perspective article, we discuss the recent scientific advances in the area of hybrid metal oxides that address these limitations.

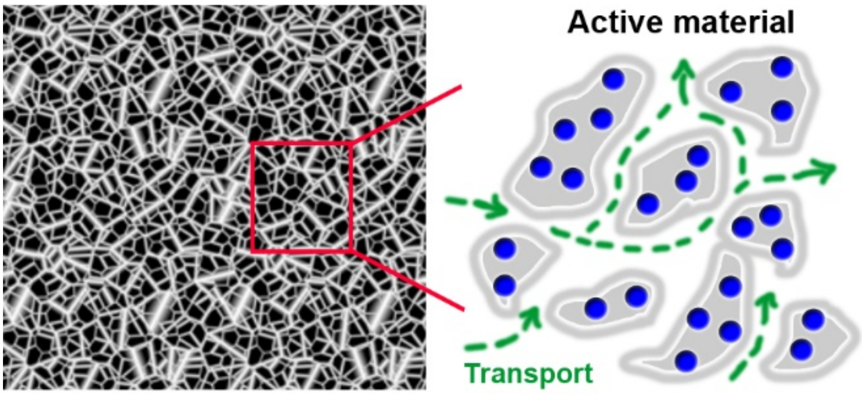

Figure 1.1 Illustration of effective ion-transport in porous materials through a smooth diffusion and penetration of ions.

Porosity plays a vital role in enhancing the electrochemical properties of materials; this was recently illustrated by *Feng et al.* in their work on mesoporous Co_3O_4.[9] Additionally, *Kang et al.* demonstrated that cross-linking alginate polysaccharide chains with Mn^{2+} ions produces a hierarchical porous MnO/C hybrid that comprises ultrasmall MnO nanoparticles in a porous carbon matrix.[10] This extensively cross-linked MnO/C hybrid showed outstanding capacity and cycling performance as an electrode material for lithium-ion batteries. A similar study by *Wang et al.* highlighted the excellent electrochemical properties of cross-linked nanoporous Co_3O_4/C hybrids.[11] Indeed, one would expect cross-linked hybrid metal oxides to exhibit a high degree of porosity due to the interconnected networks that are formed within the material. These networks are conducive for effective charge transport by facilitating a smooth diffusion and penetration of ions (Fig. 1.1). It should be noted that the covalent cross-linking of inorganic-organic materials with metal oxides is superior in this regard compared to the physical blending of constituent materials as in composites. For instance, *Yilmaz et al.* prepared highly porous V_2O_5/graphene aerogels with thiourea as a covalent cross-linker, observing a homogenous elemental distribution in contrast to a V_2O_5/graphene aerogel that was synthesized without the cross-linker.[12] The covalently cross-linked V_2O_5/graphene aerogel displayed an enriched electrochemical performance with a high specific capacitance of 484.0 F/g at 0.6 A/g; the non-crosslinked analogue showed a specific capacitance of about half of that value at the same current density.[12]

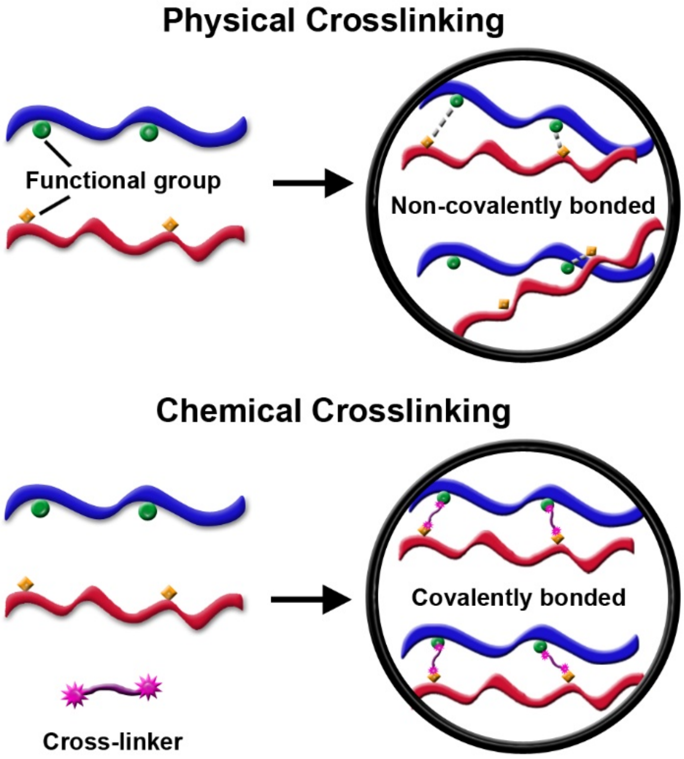

Figure 1.2 Graphical representation of physical and chemical crosslinking illustrating the type of bonding within the material.

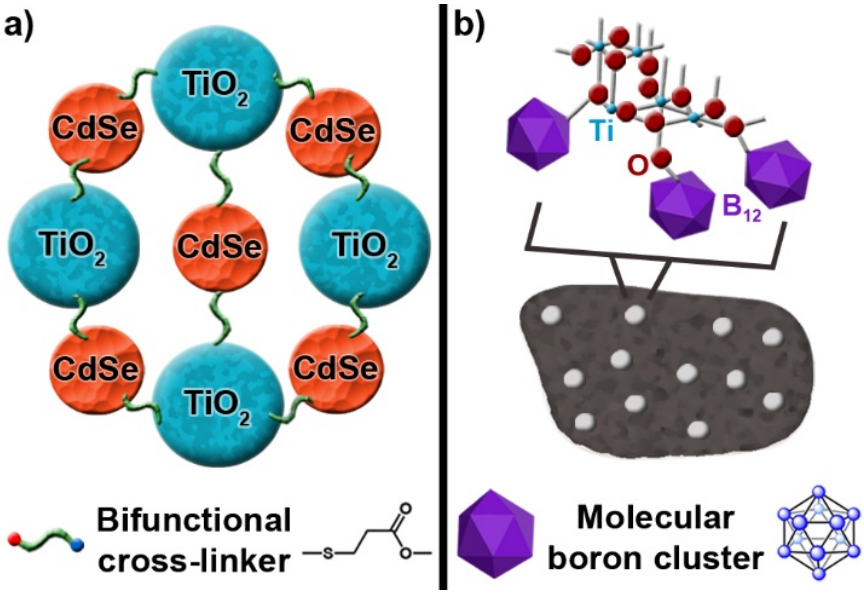

Figure 1.3 Illustration of cross-linked hybrid TiO_2 via (a) Traditional cross-linking with an organic cross-linker (b) Molecular cross-linking utilizing boron-rich clusters.

In addition to producing a homogenous composition, covalent cross-linking offers a synergy of the constituent materials and cross-linking agent. In fact, the incorporation of sulfur in the cross-linked V_2O_5/graphene aerogels contributed to its superior electrochemical performance.[12] Moreover, the strong chemical bonding between the individual material components (Fig. 1.2) reinforces robustness and chemical stability, as opposed to physically cross-linked materials which can lose structural integrity after several electrochemical cycles.[13,14] Particularly in metal oxide hybrids consisting of organic-inorganic constituents, cross-linkers ensure a more efficient ion-transport at the material interface, improving their electrochemical properties.[8] The choice of cross-linking agent is crucial, as it provides routes to generate previously unattainable functionalization for an existing metal oxide system. Several properties such as charge separation, recombination, and transport can be assisted by the cross-linker. For example, *Chen et al.* synthesized hybrid materials containing CdSe nanocrystals and TiO_2 nanoparticles using mercaptopropionic acid as a bifunctional cross-linking agent.[15] The resulting CdSe/TiO_2 heterostructure (Fig. 1.3a) displayed an enhanced photocatalytic hydrogen generation, which was attributed to the efficient charge separation and faster electron transfer between CdSe and TiO_2 in the cross-linked structure.[15]

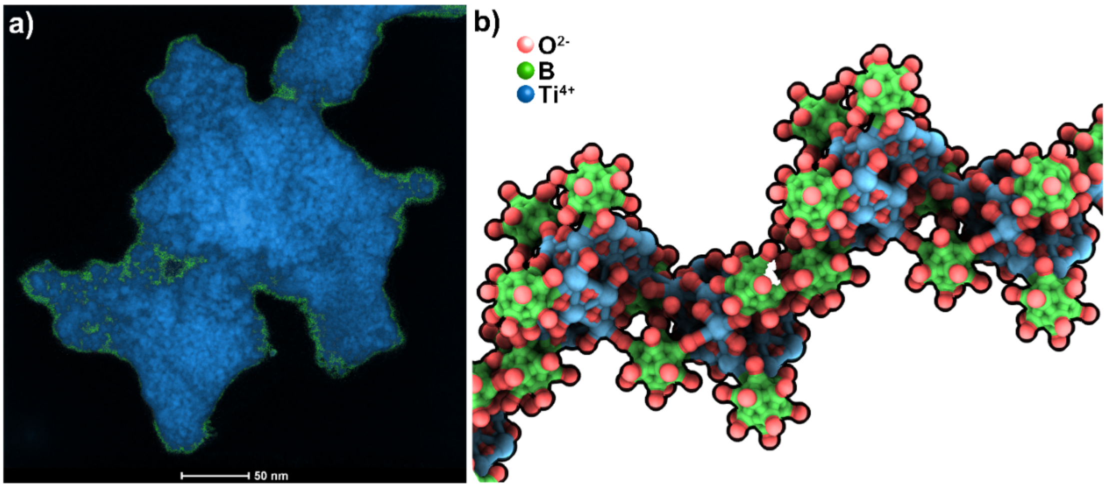

Figure 1.4 (a) Scanning transmission electron microscopy (STEM) image of the molecular cross-linked titanium dioxide hybrid material. TiO_2 nanoparticles (blue) are densely packed in the molecular boron oxides material (green). (b) Simplified and non-rigorous model of the hybrid molecular boron oxide material containing TiO_2 nanocrystals (Adapted from Reference 16).

Titanium dioxide, one of the most recognizable metal oxides, has remained a focus of much investigation. Recently, *Jung et al*. reported a bottom-up approach to manipulate metal oxides through "molecular cross-linking" whereby 3D molecular boron clusters were incorporated in a TiO_2 network (Fig. 1.3b).[16] The product featured a unique structure composed of boron-rich clusters covalently cross-linked to TiO_2 nanocrystals (Fig. 1.4). This cross-linking method not only created a porous structure as predicted, but also unexpectedly introduced an enhanced conductivity to the hybrid material. Furthermore, this new material exhibited dramatically altered light absorption properties and superior electrochemical behavior in comparison to that of pristine TiO_2, merely via the introduction of the molecular boron cross-linker.[16]

The work by *Jung et al.* poses an important question: can the introduction of a cross-linking agent do more than just enrich the existing properties of a metal oxide? In this particular case, it was speculated that the molecular cross-linking enabled a wide range of charge transfer excitations between boron clusters in different valence states, and between the clusters and the boron/titanium oxides. While the generality of this phenomenon remains to be seen, this work suggests that cross-linking can be utilized to introduce new properties to a material through appropriate choice of cross-linker.

Table 1.1 Summary of the recent advances in cross-linked hybrid metal oxides

Hybrid Metal Oxide	Cross-linker	Morphology	Properties	Limitations	Ref
MnO/C	Alginate	Ultra-small MnO nanoparticles in porous carbon	▪ High specific capacity ▪ Enhanced rate performance ▪ Long cycle life	▪ Aggregation of larger particles during cycling ▪ Capacity fading after first discharge cycle	10
Co_3O_4/C	Alginate	Hierarchical nanoporous structures	▪ High rate performance ▪ Minimal capacitance loss ▪ High cycling stability	▪ Lower specific capacitance at higher carbonization temperatures due to particle aggregation ▪ Decreased specific capacitance at increased scan rates	11
V_2O_5/ graphene	Thiourea	3-dimensional porous aerogels	▪ High specific capacitance ▪ Good long-term cycling	▪ Decreased interlayer spacing of graphene sheets upon annealing	12

				▪ Incomplete phase transition of crystalline V_2O_5 at 300 °C	
$CdSe/TiO_2$	Mercapto-propionic acid	Network of CdSe quantum dot-TiO_2 nanocrystal heterostructure	▪ Photocatalytic hydrogen generation	▪ Decomposition of cross-linkers during the long-term photocatalytic reaction	15
TiO_2/boron oxide	Perhydroxylated dodecaborate clusters	Hybrid molecular boron oxide material containing embedded TiO_2 nanocrystals	▪ Fast electron transfer rate ▪ Energy storage capability ▪ Photocatalytic activity under visible light	▪ Low electrical conductivity compared to other metal oxides	16

The advantages and properties of cross-linked metal oxide hybrids from recent advances have been summarized in Table 1.1. Future prospects of hybrid metal oxides entail the meticulous manipulation of these materials; the covalent cross-linking approach opens a distinct path to integrate new functionality into metal oxides as well as to compensate the shortcomings of existing metal oxide systems. Given a wide range of potential cross-linkers possessing different functionalities available, one can easily envision generating new hybrid metal oxides with diverse applications. Particularly, the utilization of hyper-cross-linkers possessing multiple cross-linking sites[17] can encourage a multifunctional approach towards tuning the properties of the material. This endeavor would combine practical implications along with a fundamental approach of probing these materials at the molecular level: to control material properties, such as solubility and redox potential, or even impart new dimensions by employing innovative cross-linkers, such as metal complexes to generate favorable magnetic, plasmonic, or catalytic behavior.[17–20] This information can guide researchers to make predictable modifications to metal oxides using well-defined cross-linkers in order to continually improve metal oxides. Gaining predictability in influencing the properties of hybrid metal oxides is paramount to shaping their tunability, and especially in evaluating different metal oxides for exclusive applications.

References

1. Jiang, J., Li, Y., Liu, J., Huang, X., Yuan, C. & Lou, X. W. Recent Advances in Metal Oxide-based Electrode Architecture Design for Electrochemical Energy Storage. *Adv. Mater*. 24, 5166−5180 (2012).
2. McFarland, E. W. & Metiu, H. Catalysis by Doped Oxides. *Chem. Rev.* 113, 4391−4427 (2013).
3. Wu, H. B., Chen, J. S., Hng, H. H. & Lou, X. W. Nanostructured Metal Oxide-based Materials as Advanced Anodes for Lithium-ion Batteries. *Nanoscale*, 4, 2526−2541 (2012).
4. Sreeprasad, T. S., Mailiyekkal, S. M., Lisha, K. P. & Pradeep, T. Reduced Graphene Oxide–Metal/Metal Oxide Composites: Facile Synthesis and Application in Water Purification. *J. Hazard. Mater*. 186, 921−931 (2011).
5. Chen, X., Liu. L., Yu, P. Y. & Mao, S. S. Increasing Solar Absorption for Photocatalysis with Black Hydrogenated Titanium Dioxide Nanocrystals. *Science* 331, 746−750 (2011).
6. Web of Science Core Collection keyword search on "hybrid metal oxide", September 5th 2018.
7. Sarkar, S., Guibal, E., Quignard, F. & SenGupta, A.K. Polymer-supported Metals and Metal Oxide Nanoparticles: Synthesis, Characterization, and Applications. *J. Nanopart. Res.* 14, 1−24 (2012).
8. Bouclé, J., Ravirajan, P. & Nelson, J. Hybrid Polymer-metal Oxide Thin Films for Photovoltaic Applications. *J. Mater. Chem.* 17, 3141−3153 (2007).
9. Feng, D., Gao, T.N., Fan, M., Li, A., Li, K., Wang, T., Huo, Q. & Qiao, Z.A. A General Ligand-assisted Self-assembly Approach to Crystalline Mesoporous Metal Oxides. *NPG Asia Mater.* (e-pub ahead of print 15 September 2018; doi: 10.1038/s41427-018-0072-z).

10. Kang, D., Liu, Q., Si, R., Gu, J., Zhang, W. & Zhang, D. Crosslinking-derived MnO/carbon Hybrid with Ultrasmall Nanoparticles for Increasing Lithium Storage Capacity During Cycling. *Carbon* 99, 138−147 (2016).

11. Wang, N., Liu, Q., Kang, D., Gu, J., Zhang, W. & Zhang, D. Facile Self-cross-linking Synthesis of 3D Nanoporous Co_3O_4/carbon Hybrid Electrode Materials for Supercapacitors. *ACS Appl. Mater. Interfaces* 8, 16035−16044 (2016).

12. Yilmaz, G., Lu, X. & Ho, G.W. Cross-linker Mediated Formation of Sulfur-functionalized V_2O_5/graphene Aerogels and Their Enhanced Pseudocapacitive Performance. *Nanoscale* 9, 802−811 (2017).

13. Zeng, S., Li, L., Xie, L., Zhao, D., Wang, N. & Chen, S. Conducting Polymers Crosslinked with Sulfur as Cathode Materials for High-Rate, Ultralong-Life Lithium–Sulfur Batteries. *ChemSusChem*. 10, 3378−3386 (2017).

14. Wan, W., Li, L., Zhao, Z., Hu, H., Hao, X., Winkler, D.A., Xi, L., Hughes, T.C. and Qiu, J., 2014. Ultrafast fabrication of covalently cross- linked multifunctional graphene oxide monoliths. *Advanced Functional Materials*, *24*(31), pp.4915-4921.

15. Chuang, C.H., Qin, Z., Shen, S., Doane, T. & Burda, C. Electron-transfer Dependent Photocatalytic Hydrogen Generation Over Cross-linked CdSe/TiO_2 Type-II Heterostructure. *Nanotechnology* 28, 084002 (2017).

16. Jung, D., Saleh, L. M. A., Berkson, Z. J., El-Kady, M. F., Hwang, J. Y., Mohamed, N., Wixtrom, A. I., Titarenko, E., Shao, Y., McCarthy, K., Guo, J., Martini, I. B., Kraemer, S., Wegener, E. C., Saint-Cricq, P., Ruehle, B., Langeslay, R. R., Delferro, M., Brosmer, J. L., Hendon, C. H., Gallagher-Jones, M., Rodriguez, J., Chapman, K. W., Miller, J. T., Duan, X., Kaner, R. B., Zink, J. I., Chmelka, B. F. & Spokoyny, A. M. A Molecular Cross-Linking Approach for Hybrid Metal Oxides. *Nat. Mater*. 17, 341−348 (2018).

17. Zhou, N., Cao, Z. & Xu, B. Functional Hyper-Crosslinkers. *Chem. Eur. J.* 23, 15844−15851 (2017).

18. Axtell, J. C., Saleh, L. M. A, Qian, E. A., Wixtrom, A. I. & Spokoyny, A. M. Synthesis and Applications of Perfunctionalized Boron Clusters. *Inorg. Chem*. 57, 2333−2350 (2018).

19. Wixtrom, A. I., Parvez, Z. A., Savage, M. D., Qian, E. A., Jung, D., Khan, S. I., Rheingold, A. L. & Spokoyny, A. M. Tuning the Electrochemical Potential of Perfunctionalized Dodecaborate Clusters Through Vertex Differentiation. *Chem. Commun.* 54, 5867−5870 (2018).

20. Abb, M., Wang, Y., Papasimakis, N., De Groot, C. H. & Muskens, O. L. Surface-enhanced Infrared Spectroscopy Using Metal Oxide Plasmonic Antenna Arrays. *Nano Lett.* 14, 346−352 (2013).

CHAPTER 2

A MOLECULAR CROSS-LINKING APPROACH FOR HYBRID METAL OXIDES

This chapter is a version of Jung, D.; Saleh, L. M. A.; Berkson, Z. J.; El-Kady, M. F.; Hwang, J. Y.; Mohamed, N.; Wixtrom, A. I.; Titarenko, E.; Shao, Y.; McCarthy, K.; Guo, J.; Martini, I. B.; Kraemer, S.; Wegener, E. C.; Saint-Cricq, P.; Ruehle, B.; Langeslay, R. R.; Delferro, M.; Brosmer, J. L.; Hendon, C. H.; Gallagher-Jones, M.; Rodriguez, J.; Chapman, K. W.; Miller, J. T.; Duan, X.; Kaner, R. B.; Zink, J. I.; Chmelka, B. F.; Spokoyny, A. M. "A Molecular Cross-Linking Approach for Hybrid Metal Oxides", *Nature Mater.* **2018**, *17*, 341-348.

Abstract

There is significant interest in the development of methods to create hybrid materials which transform capabilities; in particular, earth abundant metal oxides such as TiO_2 with improved or new properties relevant to a broad spectrum of applications. Here, we introduce an approach we refer to as “molecular cross-linking”, whereby a hybrid molecular boron oxide material is formed from polyhedral boron cluster precursors of the type $[B_{12}(OH)_{12}]^{2-}$. This new approach is enabled by the inherent robustness of the boron cluster molecular building block, which is compatible with the harsh thermal and oxidizing conditions that are necessary for the synthesis of many metal oxides. In this work, using a battery of experimental techniques and materials simulation, we show how this material can be successfully interfaced with TiO_2 and other metal oxides, resulting in boron-rich hybrid materials with intriguing photophysical and electrochemical properties.

Introduction

Rapid global industrialization has led to high stress on terrestrial elemental resources, particularly for elements that are capable of mediating transformative processes[1]. Because of

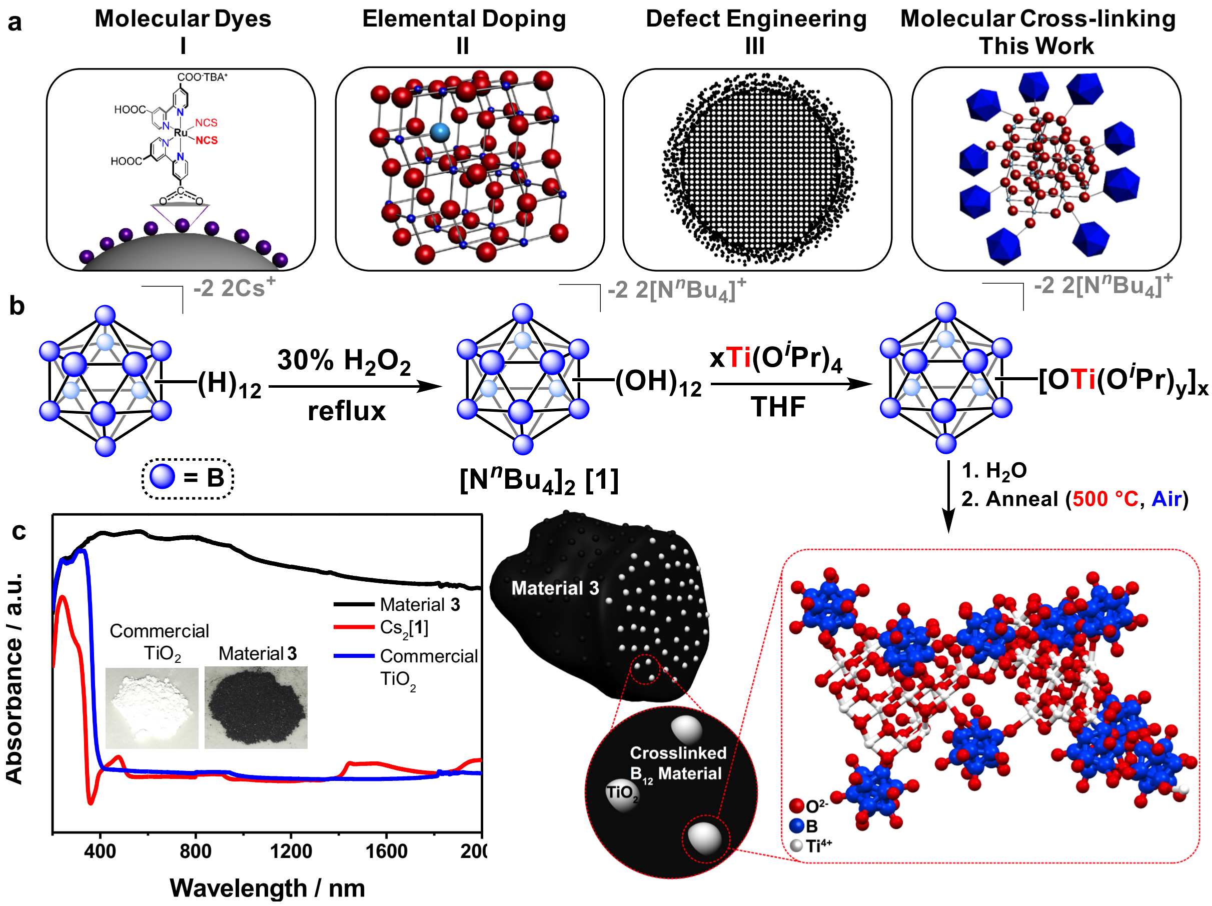

Figure 2.1 Overview of existing modification methods compared to molecular cross-linking and preparation of molecularly doped TiO_2 (3). a, Different approaches for the chemical modification of metal oxides. **I**, use of organic and inorganic dyes to sensitize metal oxide surfaces. **II**, elemental doping of metal oxides with light elements to induce changes in their bulk properties. **III**, the introduction of defects in ordered crystalline metal oxides to change their optical properties. **This work**, molecular cross-linking approach, whereby whole molecules are interfaced with metal oxides to effect changes in their photo- and electrochemical properties. **b**, Synthetic route towards the synthesis of material **3** utilizing the robust polyhedral boron cluster $[N^nBu_4]_2$[**1**] as a key precursor. **c**, (left) Diffuse-reflectance UV-Vis data for material **3**, plotted with data for TiO_2 and Cs_2[**1**] to highlight the dramatic difference in light absorption properties of all three materials; (right) simplified, non-rigorous cartoon model depicting the proposed structure of the hybrid molecular boron oxide material **3** and calculated local structure (inset).

this, oxides of elements such as iron, silicon, titanium and aluminum are extremely attractive as they are earth abundant, and their use has impacted a number of diverse and important areas, including energy storage[2], catalysis[3] and light harvesting[4]. However, despite their importance, the capability of these metal oxides to mediate transformative processes is limited, and the ability to fine-tune the properties of these materials through mild and operationally straightforward methods remains challenging, as there are a limited number of techniques available to do so[4-7]. As an example, titanium dioxide (TiO_2) has attracted significant attention in the field of renewable energy, due to its potential as a photocatalyst for important transformations such as solar energy to electricity and water-splitting[5-10]. However, its wide optical band-gap (~3.2 eV) renders it extremely inefficient as it can only capture ultraviolet (UV) light, and excludes visible light, which makes up 50 % of the solar spectrum[7]. In order to maximize the light absorptive capabilities of TiO_2, the oxide may be subjected to various chemical modifications (Fig. 2.1a). Most efforts have focused on the use of molecular organic and inorganic dyes to sensitize the surface of the oxide (Fig. 2.1a, Approach **I**), elemental doping with light elements (Approach **II**) or defect engineering (Approach **III**)[4,6,11-13].

By analogy with elemental doping, we hypothesized that it should be possible to cross-link robust molecules made of light elements within a framework of a metal oxide material. Such an endeavor would be prohibitive if restricted to more fragile organic molecules, such as used to dope organic semiconductors[14], but which are inherently unstable under most conditions required to prepare oxides such as crystalline TiO_2, which requires prolonged annealing at >500 °C in air[4]. We therefore viewed polyhedral boron-rich clusters as being potentially suitable molecules for such an undertaking (Fig. 2.1b), in particular, the anionic dodecaborate cluster ($B_{12}H_{12}^{2-}$), a three-dimensional aromatic analogue of benzene[15-23]. Whereas the electrons in benzene are delocalized over two dimensions, the electrons in dodecaborate are delocalized in three dimensions over the entire molecule. These unique properties result in a highly robust molecular scaffold, withstanding temperatures as high as 600 °C and resistant towards strong acids and bases[16,24]. We hypothesized that this combination of properties would allow for the unprecedented cross-linking of intact molecules to oxide materials, as they would be able to withstand the harsh preparation conditions. Here, we report the first successful synthesis of a hybrid boron cluster-containing boron oxide material using this "molecular cross-linking" strategy and its ability to interface with metal oxides. Importantly, this method creates a material with dramatically altered photophysical and electrochemical properties.

Results and Discussion

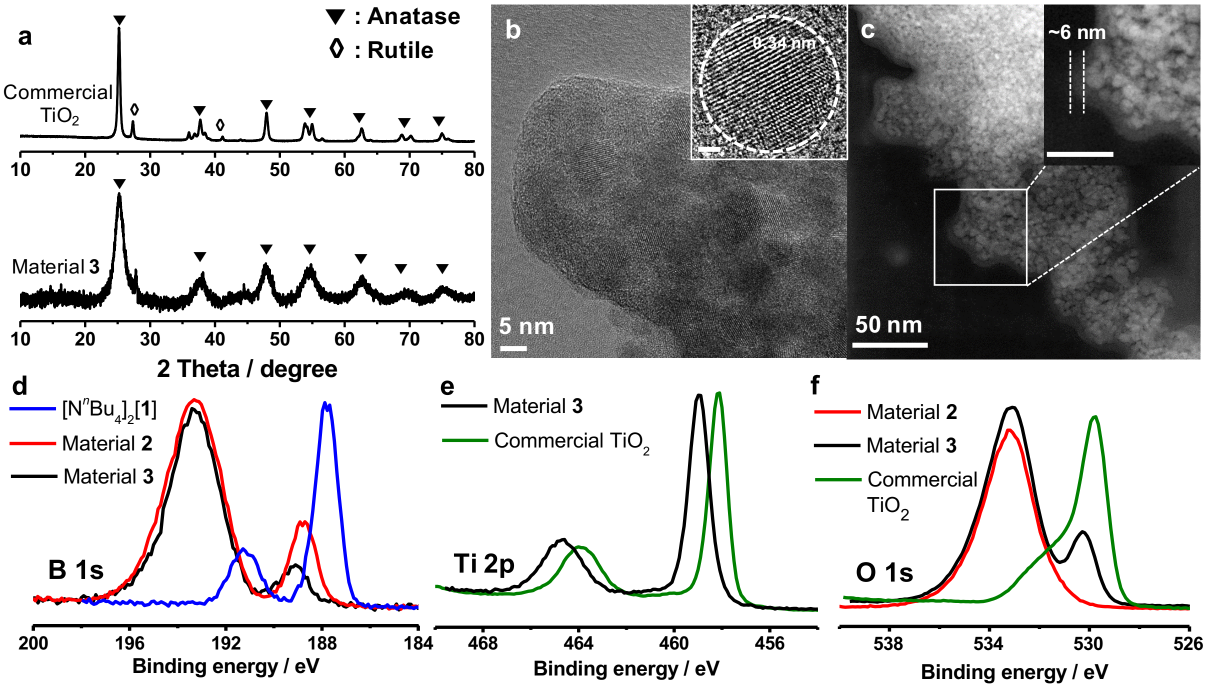

Figure 2.2 Structural data for material 3. **a**, PXRD of commercial TiO_2 and **3** revealed the presence of crystalline TiO_2 in the anatase phase, which is the expected phase when annealed at 500 °C, with the broadness of the peaks indicative of very small crystalline domains. **b**, TEM image of **3**. The inset shows the HRTEM of a crystalline TiO_2 domain free of disorder in **3** (scale bar= 2nm). **c**, STEM image of **3**, highlighting the densely packed TiO_2 nanoparticles which are embedded in material **2**. The inset shows an expansion of outer amorphous layer in

3, attributed to material **2** (scale bar= 25 nm). **d**, The boron 1*s* region of [$N^n Bu_4$]$_2$[**1**] shows two peaks at 187.8 eV and 191.2 eV, which can be explained by the ability of **1** and its derivatives to access multiple well-defined oxidation states (see main text for details). For materials **2** and **3**, the boron 1*s* region contains a peak at 189.2 eV corresponding to an intact cluster, and another at 193.1 eV corresponding to boron oxide. The *ca*. +2 eV change in binding energy observed for the peak associated with the intact cluster in **2** and **3** compared to [$N^n Bu_4$]$_2$[**1**] can be attributed to the intact cluster being more oxidized, possibly as a mixture of 2- and 1- oxidation states. **e**, The titanium 2*p* region of **3** shows peaks at 459.1 eV and 464.8 eV respectively, slightly shifted from pristine TiO_2, but indicative of Ti^{4+}. **f**, The oxygen 1*s* region for TiO_2, **2** and **3**.

We focused on the use of the perhydroxylated derivative of dodecaborate, $[B_{12}(OH)_{12}]^{2-}$ (referred to herein as **1**, Fig. 2.1b), as a precursor due to its amenability to further functionalization[25]. Thermogravimetric analysis (TGA) of the salt Cs_2[**1**] was carried out to assess the general robustness of the cluster, and revealed minimal mass loss for Cs_2[**1**] up to 900 °C (Supplementary Fig. 1). Similar analysis of the more synthetically useful derivative [$N^n Bu_4$]$_2$[**1**] was not possible due to its strongly hygroscopic nature, and so a bulk sample of [$N^n Bu_4$]$_2$[**1**] was annealed at 500 °C in air, with the intention to analyze the product by other methods. We were surprised to recover a black powder (referred to herein as **2**) rather than the expected white material as in the case of Cs_2[**1**]. This is extremely unusual, as the vast majority of boron-rich clusters are white powders and to the best of our knowledge there currently does not exist any material containing boron and oxygen that is black. Intrigued by the uniquely intense colour of **2**, we subjected the sample to diffuse-reflectance UV-Vis spectroscopic analysis. Material **2** demonstrated absorption from the UV range all the way to the near IR (NIR) range (Supplementary Fig. 2). Material **2** was further probed by powder X-ray diffraction (PXRD), scanning electron microscopy (SEM), and transmission electron microscopy (TEM) to acquire its structural information (Supplementary Figs. 2 and 3). X-ray photoelectron spectroscopic (XPS) analysis was employed to probe the elemental composition on the surface of **2,** excluding the presence of elemental boron (Supplementary Fig. 4). Here, a cross-linked polymer of intact clusters and boron oxide is formed, effectively trapping the carbon-containing fragments before they can be combusted in air during the annealing process (Supplementary Fig. 5 and Table 1).

With the hybrid molecular boron oxide material **2** in hand, we explored the possibility of interfacing **2** with earth abundant metal oxide nanoparticles, focusing on TiO_2. This interfacing would potentially engender properties not normally found in boron-rich materials. Given the previous effort in interfacing $[N^nBu_4]_2$[**1**] with organic functional groups via perfunctionalization leading to $[B_{12}(OR)_{12}]^{2-}$ motifs featuring B–O–C bonding connectivities[25-28], we hypothesized that one can develop a strategy leading to the formation of B–O–Ti interactions from **1**. A common precursor for the synthesis of TiO_2 is titanium tetraisopropoxide ($Ti(O^iPr)_4$), an air and moisture sensitive liquid. Controlled hydrolysis of this liquid, followed by annealing at the appropriate temperature is a common route to produce various phases of crystalline TiO_2[4]. We hypothesized that reacting $[N^nBu_4]_2$[**1**] with $Ti(O^iPr)_4$ would result in protonolysis, the elimination of *iso*propyl alcohol and the formation of a B–O–Ti linkage (Fig. 2.1b). A test reaction mixture of $[N^nBu_4]_2$[**1**] with $Ti(O^iPr)_4$ was subjected to ^1H solution nuclear magnetic resonance (NMR) spectroscopic analysis, with the resultant spectrum clearly showing the presence of *iso*propyl alcohol (Supplementary Fig. 6), verifying B–O–Ti bond formation. Reaction of $[N^nBu_4]_2$[**1**] with $Ti(O^iPr)_4$ produces a clear red-orange solution, which is subsequently hydrolyzed to form a red-orange gel (Supplementary Fig. 7). After calcining at 120 °C, the now dark orange solid is annealed at 500 °C in air to produce material **3** as a shiny black solid, contrasting sharply with both the white colour of pristine TiO_2 and the pre-annealed $[N^nBu_4]_2$[**1**] (Fig. 2.1c). Material **3** is remarkably stable as evidenced by our inability to dissolve it even after prolonged exposure to a variety of organic solvents, strong acids, strong bases and 3% H_2O_2 consistent with its hypothesized highly cross-linked composition (Supplementary Fig. 8).

Diffuse-reflectance UV-Vis spectroscopic analysis of **3** produced similar results to that found for material **2**, with strong and sustained absorption from the UV to NIR range (Fig. 2.1c). Structural information for **3** was then obtained from PXRD, SEM and high-resolution TEM (SEM, Supplementary Fig. 9, and HRTEM, Fig. 2.2 and Supplementary Fig. 10). PXRD of material **3** provides evidence for crystalline anatase TiO_2, while the HRTEM images display crystalline TiO_2 domains with no evidence of disorder (inset, Fig. 2.2b). Further evidence for anatase is provided by selected area electron diffraction (SAED) and d-spacing measurements (Supplementary Fig. 11). Additional structural information was provided by scanning TEM (STEM, Fig. 2.2c) and a 3D reconstruction (Supplementary Fig. 12) providing a cross-sectional view of the material, depicted as a cartoon model in Figure 1c. Specifically, densely embedded TiO_2 nanocrystals are observed, with an additional *ca*. 6 nm thick band of amorphous material on the edges, which is attributed to interfaced material **2**. To interrogate the content of the amorphous component in **3**, we first examined this material using Raman spectroscopy. The six Raman active modes for anatase TiO_2[12] were not detected, where instead only bands associated with the boron cluster at 1370 and 1600 cm^{-1} are observed (Supplementary Fig. 13), suggesting that the TiO_2 is not present in any significant quantity on the surface of **3**. XPS measurements of material **3** were carried out, with measurements of $[N^nBu_4]_2$[**1**] and TiO_2 providing benchmark values (Fig. 2.2d-f). The boron 1*s* region reveals the presence of intact boron clusters at 189.2 eV and boron oxide at 193.1 eV (Fig. 2.2d and Supplementary Fig. 14). The higher binding energy for the intact clusters in **3** suggests they are more oxidized than the clusters in the starting material $[N^nBu_4]_2$[**1**], which have a lower binding energy of 187.8 eV (Fig. 2.2d). XPS also shows the presence of residual carbon at 284.5 eV in the sample despite annealing in air at 500 °C (Supplementary Fig. 15). While some of the carbon content can be attributed to the unavoidable presence of adventitious carbon from air, combustion analysis confirms the presence of ~8.7 % carbon in the material, assigned as graphitic carbon based on the XPS binding energy (Supplementary Table 2). The appearance of graphitic carbon suggests a likely templating effect imposed by the clusters, reminiscent of the cross-linked "molecular frameworks" recently reported by Bao and co-workers[29,30], albeit with significantly lower carbon content in the case of **3**. To clarify the proposed trapping events during the synthesis and annealing processes leading to **3**, we subjected pre-annealed material **3** to TGA-MS analysis measured in air (Supplementary Fig. 16–18). The experimental conditions for forming material **3** favour retaining carbon despite the high temperatures and oxygenated atmosphere ultimately suggesting trapping through templation (Supplementary Table 3).

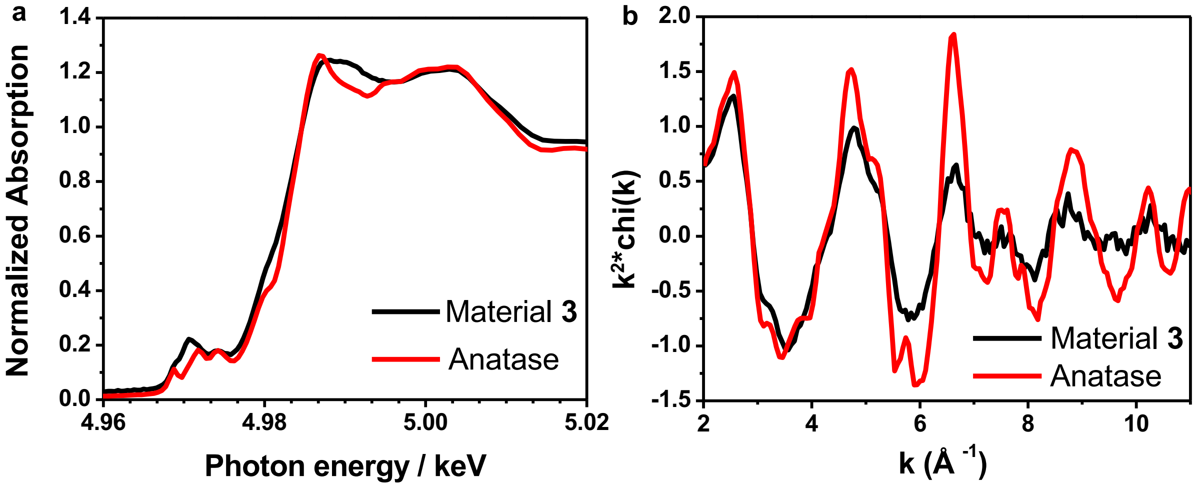

Figure 2.3 XANES and EXAFS data for anatase TiO_2 and material 3. a, XANES measurements on **3** were compared to that measured for anatase TiO_2. The Ti K edge structure for **3** matches that found for anatase, confirming the presence of anatase with titanium exclusively in the 4+ oxidation state. **b**, The k-squared weighted EXAFS function of material **3** and anatase. From this data, an average Ti–O bond distance of 1.95 Å for TiO_2 in **3** can be extracted, which is expected for TiO_2 in the anatase phase.

As the penetration depth of the XPS beam reaches *ca*. 10 nm, the titanium 2*p* peaks could be observed for material **3** (Fig. 2.2e) consistent with the presence of Ti(IV) in the sample. To confirm the oxidation state of Ti in bulk **3**, X-ray Absorption Near-Edge Spectroscopy (XANES) measurements were performed (Fig. 2.3, summarized in Supplementary Table 4). The obtained data confirms the presence of Ti(IV) with no observable Ti sites in lower oxidation states.

While the data obtained thus far supports the model depicted in Figure 2.1c, identification of the presence of intact clusters in material **3** remained indirect. Furthermore, while we could also conclude that no borides or carbides are present in material **3** on the surface, they are well known to form from boron cluster materials in the bulk, albeit at high temperatures and under reducing inert environment[31,32]. We therefore turned to solid state NMR (SSNMR) spectroscopy to further probe the bulk structural features of **3** (Figs. 2.4a and b, and Supplementary Figs. 19–22). The presence of intact B_{12}-based clusters in material **3** is demonstrated directly by one-dimensional (1D) and two-dimensional (2D) solid-state ^{11}B magic-angle-spinning (MAS) NMR measurements, which are sensitive to the local environments of ^{11}B atoms in the material. The 1D single-pulse ^{11}B MAS NMR spectrum of material **3** (Fig. 2.4a, top) shows a relatively broad (13 ppm full-width half-maximum, FWHM) signal at -16 ppm, which is assigned to intact B_{12}-based clusters, based on comparison to a reference material containing intact B_{12}-based clusters, Cs_2[**1**], (Supplementary Fig. 19). Two additional ^{11}B signals are detected at 2 and 17 ppm, the latter of which is assigned on the basis of its ^{11}B shift position to boron oxides or borates in the material[33] The relatively narrow signal at 2 ppm (ca. 3 ppm FWHM) is assigned to intact or partially intact B_{12}-based clusters at particle surfaces, similar to that observed in the literature for ^{11}B MAS NMR measurements of B-doped TiO_2[33]. The presence of hydroxylated moieties, such as surface bound hydroxyls or residual water, is demonstrated by the 1D $^{11}B\{^1H\}$ CP-MAS spectrum of material **3** (Fig. 2.4a, bottom), which shows that the ^{11}B signals at 17 and 2 ppm are enhanced by ^{1}H-^{11}B cross-polarization transfer. The relative intensity of the signal at -16 ppm is greatly reduced in the ^{11}B{^{1}H} CP-MAS spectrum, compared to the single-pulse ^{11}B spectrum, indicating that the majority of the molecular B_{12}-based clusters in material **3** are not hydroxylated.

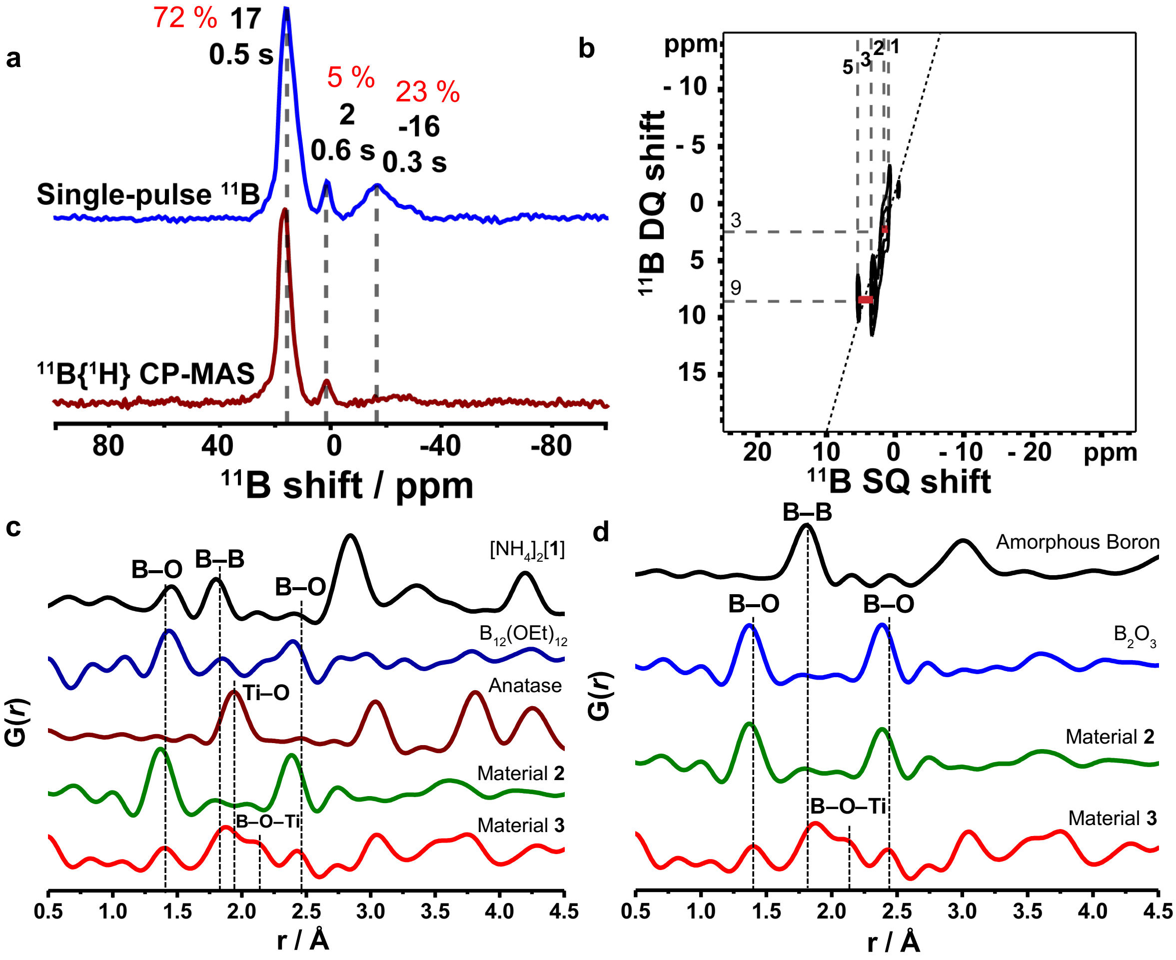

Figure 2.4 Solid-state ^{11}B MAS NMR and PDF analysis. a, Solid-state 1D single-pulse ^{11}B MAS NMR (top) and ^{11}B{^{1}H} CP-MAS (bottom) spectra of material **3** acquired at 18.8 T and 298 K, showing three resolved ^{11}B signals at -16, 2, and 17 ppm, assigned to subsurface boron clusters, surface boron clusters, and boron oxide/borates, respectively, and the corresponding percentages are 23, 5, and 72 %, respectively. **b**, 2D *J*-mediated (through-bond) ^{11}B{^{11}B} correlation spectrum of **3**. Correlated ^{11}B signals detected across the diagonal dotted line establish unambiguously the through-bond covalent connectivities of distinct ^{11}B species. The

correlated signal pairs at ^{11}B (SQ,DQ) shifts of (5 ppm, 9 ppm) and (3 ppm, 9 ppm) and (2 ppm, 3 ppm) and (1 ppm, 3 ppm) (red lines) thus confirm the presence of B–B bonds in **3**. **c**, PDF analysis of materials **2** and **3**, directly compared with $[NH_4]_2$[**1**] and $[B_{12}(OEt)_{12}]^0$ controls to provide data on B–O and B–B bond distances in intact clusters in various oxidation states, and anatase TiO_2 to directly assess Ti–O bond distances. Clear correlations can be observed confirming the presence of both B–O and B–B bonds in materials **2** and **3**, with the presence of B–B bonds significant as they are diagnostic for the presence of intact clusters. **d**, Additional PDF analysis of materials **2** and **3** with B_2O_3 and amorphous elemental boron controls to provide data on B–O and B–B bond distances in the oxide and element respectively. While the PDF analyses for material **2** and B_2O_3 look superficially similar, more careful observation reveals the presence of B–B bonds in **2**.

Distinct surface moieties in the B_{12}-based clusters in material **3** are connected via covalent bonds, as determined by the solid-state 2D $^{11}B\{^{11}B\}$ *J*-mediated (through-covalent-bond) MAS NMR spectrum in Fig. 2.4b. The spectrum is presented as a 2D contour plot having single-quantum (SQ) and double-quantum (DQ) ^{11}B shift axes with pairs of signals from *J*-coupled ^{11}B species that are correlated across the diagonal at SQ shift positions Ω_1 and Ω_2 and at the same DQ shift ($\Omega_1+\Omega_2$). Such 2D *J*-mediated measurements are sensitive principally to *J*-couplings (ca. 20 Hz) between directly-bonded $^{11}B–^{11}B$ spin-pairs; *J*-couplings between next-nearest-neighbor ^{11}B species (e.g., $^{11}B–O–^{11}B$) are an order of magnitude weaker (ca. 2 Hz)[34]. The 2D *J*-mediated $^{11}B\{^{11}B\}$ NMR spectrum in Fig. 2.4b of material **3** shows two pairs of correlated signal intensity at (SQ, DQ) shift coordinates of (5 ppm, 9 ppm) and (3 ppm, 9 ppm) and at (2 ppm, 3 ppm) and (1 ppm, 3 ppm) (red lines), establishing that the corresponding ^{11}B species are covalently linked. These 2D results establish unambiguously that underlying the ^{11}B signal at 2 ppm in Fig. 4b are at least four very narrow (ca. 0.5 ppm FWHM) ^{11}B signals that arise from distinct covalently-connected ^{11}B moieties in locally-ordered environments at the particle surfaces. No *J*-correlated signals are observed for the peaks at 17 and -16 ppm, consistent with the weak ^{11}B–O–^{11}B *J*-couplings associated with the boron oxide moieties and the influence of paramagnetic relaxation. The local bonding environments and proximities of these species can nevertheless be determined from analogous dipolar-mediated spectra that exploit much stronger dipolar interactions between nearby ^{11}B atoms. In addition to the same 2D intensity correlations, a complementary 2D dipolar-mediated (through-space, <1 nm) ^{11}B{^{11}B} MAS NMR spectrum (Supplementary Fig. 22) shows an additional correlated ^{11}B signal at (-27 ppm, 14 ppm). This intensity correlation is associated with the B_{12}-based clusters and the boron oxide species, and thus, establishes their nanoscale proximities in material **3**.

Finally, to further our understanding of the clusters in **2** and **3**, we conducted pair distribution function (PDF) analysis of the high energy X-ray scattering data obtained for the cluster-based materials (Fig. 2.4c and d), which is a powerful method that provides atomic-scale local structural information within a material, with peaks within the PDF corresponding directly to bond distances and atom-atom distances. Crucially, information about a material may be extracted directly from the PDF independent of a structural model, allowing identification of local bonding and coordination environments even in amorphous materials[35]. Features corresponding to B–O bond distances (~1.40 Å) can clearly be observed for material **2** (Supplementary Fig. 23), while features corresponding to cluster-based B–B bond distances (~1.75 Å to ~1.87 Å) are significantly reduced in intensity when compared to the molecular cluster control samples, likely due to the cross-linked clusters adopting a more random arrangement. For material **3**, peaks corresponding to B–O, B–B and Ti–O distances can be found, with an additional peak observed at ~2.13 Å which corresponds to the distance expected for a Ti–O–B linkage. Overall, the measurements are consistent with the findings from the SSNMR data in confirming the presence of intact boron clusters in both **2** and **3**.

The combined comprehensive structural characterization of material **3** validates the proposed model for **3** as being a hybrid molecular boron oxide material consisting of a cross-linked network of intact boron cluster units and boron oxide, within which are embedded TiO_2 nanocrystals in the anatase phase (Supplementary Figs. 24–31 and 39).

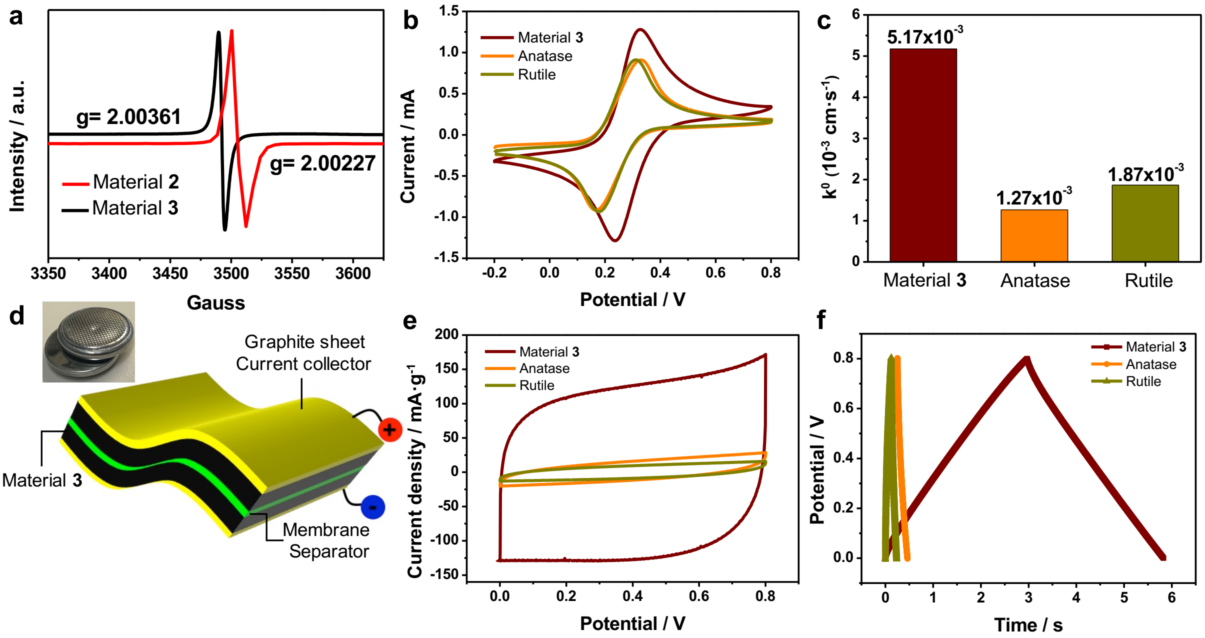

Figure 2.5 Data for the electrochemical properties of material 3. a, Electroparamagnetic resonance (EPR) spectroscopy at room temperature of materials **2** and **3**. Each material produces a peak, with corresponding *g*-values of 2.00361 and 2.00227, very close to that found for single molecular boron cluster radicals. The origin of the paramagnetism is related to **2** and the paramagnetism is perturbed when TiO_2 is introduced to **2**. **b**, CV for the ferri/ferrocyanide redox couple, comparing the heterogeneous electron transfer rate of **3** to anatase and rutile TiO_2. Material **3** produces the smallest peak-to-peak separation in the CV, indicating an enhancement in electrochemical performance with respect to TiO_2. **c**, Bar chart showing the electron transfer rate constants for **3**, anatase and rutile TiO_2. The electron transfer rate for material **3** is three to four times faster than that for pure phases of TiO_2**. d**, A schematic illustration of a pouch-cell supercapacitor. **e**, CV curves obtained at a scan rate of 1000 mV/s for the pouch-cell supercapacitors consisting of material **3**, anatase, and rutile TiO_2. The integrated area is dramatically increased in material **3**. **f**, Galvanostatic charge/discharge curves of material **3**,

anatase, and rutile TiO_2 supercapacitors at the current density of 0.04 mA/cm^2. The charge/discharge curves of material **3** exhibit an ideal triangular and symmetric shape, indicating a good energy storage capability.

Previously, **1** and several functionalized derivatives of it were shown to display pseudo-metallic redox-active behavior[36]. The potential presence of clusters in **3** in different redox states prompted us to probe the electronic properties of material **3**. First, we subjected **3** to electroparamagnetic resonance (EPR) spectroscopy (Fig. 2.5a), observing a spectrum featuring a characteristic singlet with *g*-values very close to that found for single molecular boron cluster radicals[26,37]. SQUID magnetometry performed on material **3** (Supplementary Fig. 32) revealed a decrease in magnetic susceptibility with increasing temperature, indicating material **3** was paramagnetic. EPR spectroscopy of material **2** also produced a singlet with a similar *g*-value to **3**, suggesting that the origin of the paramagnetism is related to the cross-linked hybrid molecular boron oxide material **2**.

The potential redox activity of material **3** prompted us to further investigate this material electrochemically (Supplementary Figs. 33–38, and 42–47). Use of the ferri/ferrocyanide redox couple can provide useful information about the electron transfer capability of electrochemically-active materials and their potential competence as an electrocatalyst[38]. The electron transfer rate constant of **3** is significantly faster than that observed for both forms of TiO_2 (Fig. 2.5c), material **2** and graphitic carbon (Supplementary Figs. 33–35). The results of these measurements on material **3** highlight the ability of the hybrid molecular boron oxide material to confer favorable electronic properties on metal oxides (Supplementary Figs. 40–41).

Given the electrochemically-active nature and high electrical conductivity of material **3**, we further assembled pouch-cell supercapacitors using **3** as an active layer component (Fig.

2.5d). The pouch-cell supercapacitor consisting of **3** exhibited outstanding performances in comparison to both forms of TiO_2 (Fig. 2.5e and f). The CV curve of **3** displayed a quasi-rectangular shape, and the charge/discharge curves followed the ideal triangular and symmetric profiles. The calculated gravimetric capacitance of material **3** was found to be 112.2 mF/g at the scan rate of 1000 mV/s, which is significantly greater than both anatase (33.3 mF/g) and rutile TiO_2 (15.0 mF/g). These excellent performances compared to pristine TiO_2 can be attributed the cross-linking in **3**, which renders this material more conductive[39]. Moreover, nano-sized TiO_2 (< 10 nm) not only provides a larger electrode-electrolyte contact area, but also effectively decreases the ion diffusion length, leading to reduced ionic diffusion resistance and charge transfer resistance[40] (Supplementary Fig. 47). These results highlight a promising energy storage capability of material **3**.

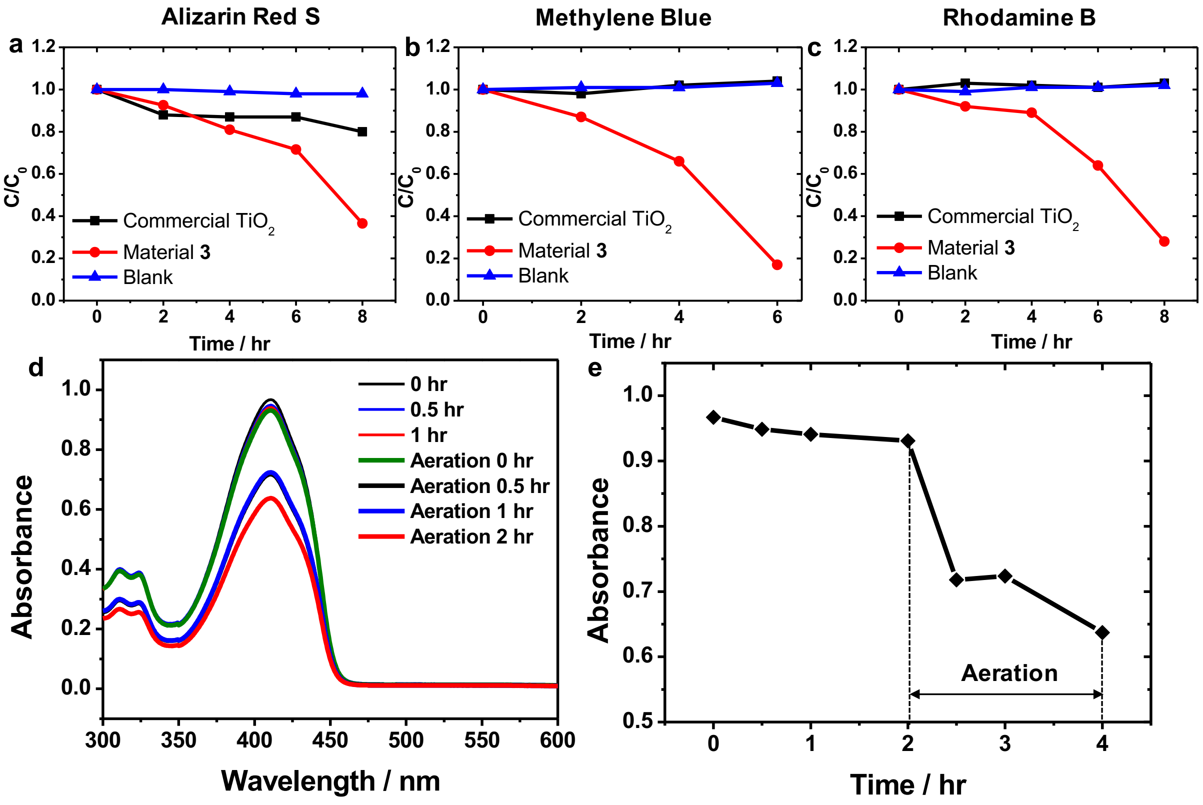

Figure 2.6 Photochemical data for material 3. a-c, Photocatalytic degradation of three dyes, Alizarin Red S (**a**), Methylene Blue (**b)** and Rhodamine B (**c**), under red (~630 nm) LED light conditions. In each case, **3** was found catalyze the photodegradation of the dye at substantially

faster rates than commercial TiO_2. **d**, UV-Vis spectrum depicting the progression of the consumption of diphenylisobenzofuran (DPBF) in the presence of **3** and irradiation with red (~630 nm) LED lights. DPBF is a sensitive fluorescent probe for ROS, and a decrease in its absorbance at 410 nm is indicative of the production of ROS. Aeration of the reaction mixture leads to increased rates of consumption of DPBF, consistent with ROS production. **e**, A chart showing the rate of consumption of DPBF.

Given the substantial interest in visible-light assisted photochemical processes featuring photosensitized TiO_2 materials[4,5,12,13], we hypothesized whether the remarkable light absorption properties of **3** (Fig. 2.1c) could be leveraged for photochemical processes mediated by visible light. We investigated the use of **3** as a photocatalyst for the visible-light driven photocatalytic decomposition of a variety of water contaminants (Fig. 2.6a-c). Using simple, low power red (630 nm) LEDs as the light source, photodegradation of three common dye contaminants were observed to proceed at faster rates for **3** than for pristine TiO_2 used as a control. The mechanistic study of the observed photodegradation suggests that **3** can be photoexcited with visible light and engage in an efficient electron transfer with oxygen gas molecules producing reactive oxygen species (ROS) capable of degrading organic contaminants (Figures 2.6d and e, and Supplementary Fig. 48)[41]. Importantly, given that material **3** contains no precious metal components (only Ti, B, C and O), this presents a potentially powerful and cost-effective approach for waste remediation.

Outlook

The successful modification of TiO_2 demonstrates the value of molecular cross-linking as a new and previously unattainable strategy for effecting change in the properties of metal oxide materials, enabled by the inherent robustness of an inorganic molecular cluster[42-45]. Our preliminary experiments suggest that one can expand the repertoire for this method toward hybrid materials containing ZrO_2. Importantly, these hybrids feature similar cross-linked morphology observed in the case of TiO_2 (Supplementary Figs. 49–58). This approach expands on the existing strategies allowing the incorporation of molecular fragments within inorganic materials[46-49]. The exhaustive structural characterization of material **3** supports its description as a cross-linked hybrid molecular boron oxide material embedded with TiO_2 nanoparticles. The unique structure of the material engenders dramatically improved electro- and photochemical behavior, evidenced by fast electron-transfer rates, low resistivity and the ability to photo degrade common dye contaminants under visible light conditions, and molecular cross-linking of TiO_2 is indeed responsible for all the observed features. The simplicity and potential generality of the route, where interfacing molecular clusters to a metal oxide via a facile reaction proceeding at room temperature using readily available precious metal-free precursors, makes this potentially amenable to a wide range of other metals and associated applications.

Methods

General Synthetic Methods

Dry-box manipulations were carried out under an atmosphere of dinitrogen in a Vacuum Atmospheres NexGen dry-box. THF was dried prior to use by sparging with argon, and then loaded on a Solvent Purification System (JC Meyer Solvent Systems). THF was then collected and stored over activated 4 Å molecular sieves in a dry-box under dinitrogen atmosphere. ^1H solution NMR spectra were recorded in THF-d_8, which was dried and stored over activated 4 Å molecular sieves. NMR samples were prepared under dinitrogen in 5 mm Norell S-5-400-JY-7 tubes fitted with J. Young Teflon valves. ^1H solution NMR spectra were recorded on

AV300 spectrometers in ambient conditions and referenced internally to residual protio-solvent and are reported relative to tetramethylsilane ($\delta = 0$ ppm). Chemical shifts are quoted in δ (ppm). Combustion analyses of materials **2** and **3** were carried out by the Microanalytical Facility at the College of Chemistry, University of California, Berkeley (Berkeley, CA). Annealing of samples were carried out in an Across International CF1100 muffle furnace.

The following chemicals and materials were sourced from commercial vendors: $Ti(O^iPr)_4$ (titanium tetraisopropoxide (TTIP), ACROS Organics), TiO_2 (J. T. Baker), pure anatase (Sigma Aldrich), pure rutile (Sigma Aldrich), Ti_2O_3 (Sigma Aldrich), TiO (Sigma Aldrich), Ti foil (Sigma Aldrich), TiB_2 (Materion), TiC (Strem Chemicals), Graphite (Carbon Graphite Materials, Inc.), Crystalline Boron (Advanced Materials), Amorphous Boron (Fisher Scientific), B_2O_3 (J. T. Baker), Methylene Blue (ACROS Organics), Alizarin Red S (ACROS Organics), Rhodamine B (ACROS Organics). $Zr(O^iPr)_4 \bullet {}^iPrOH$ (Strem Chemicals), ZrO_2 (SPEX Industries, INC.)

Cesium and $[N^nBu_4]^+$ salts of $[B_{12}(OH)_{12}]^{2-}$ (**1**) were synthesized by previously reported methods[50].

Material 2. $[N^nBu_4]_2$[**1**] was added to a 20 mL glass scintillation vial and transferred to a muffle furnace. The sample was annealed by heating from room temperature to 500 °C at a rate of 1°C/min and holding at 500 °C for six hours. After that, the furnace was cooled to room temperature at a rate of 1 °C/min and **2** is recovered as a black powder.

Material 3. The synthesis was carried out in an inert atmosphere dry-box. In a 20 ml glass scintillation vial, a clear solution of titanium tetraisopropoxide $Ti(O^iPr)_4$ (833 mg, 0.87 mL, 2.93 mmol), in THF (1 mL) was added to a stirring suspension of $[N^nBu_4]_2$[**1**] (200 mg, 0.244

mmol). The reaction mixture becomes orange upon addition, and was stirred for 6 h at room temperature. The clear red-orange reaction mixture is then brought outside of the dry-box, whereupon water (0.8 mL) is carefully added, forming an orange gel. The gel is then heat treated at 120 °C for two hours to remove volatiles to produce a glassy red-orange solid. The sample is annealed in the same way as material **2**, and **3** is recovered as a black powder.

Material 4. The synthesis was carried out in a similar fashion as material **3**. Zirconium tetraisopropoxide isopropanol complex (568 mg, 1.46 mmol), in THF (1 mL) was added to a stirring suspension of $[N^{n}Bu_4]_2[\mathbf{1}]$ (100 mg, 0.122 mmol). Upon adding 0.8 ml of water to the reaction mixture, a pink gel is formed. After annealing it at 500 °C in air, material **4** is recovered as a light brown powder.

Characterization Methods and Instrumentation

Diffuse reflectance UV-Vis spectra were collected using Cary 5000 UV-VIS Spectrometer. Powder X-ray diffraction (PXRD) was undertaken on a Panalytical X'Pert Pro X-ray Powder Diffractometer with Cu-Kα radiation. Diffraction spectra were collected from a 2θ angle of 10 to 80 degree with a step size of 0.04 degree at a rate of 1 degree/min. High-resolution transmission electron microscopy (HRTEM) was performed using a FEI Titan S/TEM operated at 300 kV. The samples were prepared by dropping an ethanol dispersion onto copper TEM grids (200 mesh, Formvar/Carbon, Ted Pella, Redding, CA) using 1 ml syringes and dried in air. For 3D tomography, samples were crushed into a fine powder by ball milling before being dispersed in 70% ethanol/dH_2O at a concentration of 1mg/ml. 2 µl of this suspension was dispersed onto a TEM grid coated with an ultra-thin Carbon film (Ted Pella) and allowed to air dry. Tomographic data acquisition was performed on a Titan S/TEM (FEI) operating in TEM mode at 300keV. Images were acquired on an Ultrascan, 2x2K digital camera (Gatan) at regular

2 degree tilts between -28 and 30 degrees. Tomographic reconstruction was performed in MATLAB (mathoworks) using the GENFIRE reconstruction algorithm[51,52]. Briefly images had their contrast inverted and a flat background was subtracted to remove the influence of the substrate. Images were then manually cropped and aligned to the images center of mass before being binned 3 x 3. Reconstructions were performed for 50 iterations with 5 rounds of orientation refinement.

A Bruker EMX EPR spectrometer was used to acquire EPR spectra, with all spectra collected on solid powder samples at room temperature. X-ray photoelectron spectroscopy (XPS) was performed using an AXIS Ultra DLD instrument (Kratos Analytical Inc., Chestnut Ridge, NY, USA). All XPS spectra were measured using a monochromatic Al K X-ray source (10 mA for both survey and high-resolution scans, 15 kV) with a 300 x 700 nm oval spot size. The pressure of analyzer chamber was maintained below 5×10^{-8} Torr during the measurement. Spectra were collected with 160 eV pass energy for survey spectra and 20 eV for high-resolution spectra of C 1*s*, O 1*s*, B 1*s*, and Ti 2*p* using a 200 ms dwell time. All XPS peaks were charge referenced to the adventitious carbon 1*s* signal at 284.6 eV. Scanning electron microscopy (SEM) images were obtained with a field-emission SEM (JEOL JSM 6700F). SQUID magnetometric data was measured by a Magnetic Property Measurement System (MPMS V XL, Quantum Design Company). Thermogravimetric analysis (TGA) was carried out on a Pyris Diamond TG/DTA (PerkinElmer instruments) at a heating rate of 5 °C /min from room temperature to 1000 °C under argon flow. Raman spectra were collected by a triple monochromator and detected with a CCD. Pellets of Cs_2[**1**], material **3**, and TiO_2 were excited by an argon ion laser at wavelength 457.9 nm at laser power of 100 mW. N_2 adsorption isotherms were obtained at 77 K on a TriStar volumetric adsorption analyzer (Micromeritics). Ammonia Temperature-Programmed Desorption (TPD) experiments were performed using an Altamira Instruments System (AMI-200) equipped with a Thermal Conductivity Detector

(TCD). Each sample (100 mg) was loaded into a quartz U-tube and the catalyst bed was held in place by quartz wool on both ends. The samples were flushed with helium (30 cc/min) for 10 min at 25 °C. While still flushing with helium, the temperature was increased to 200 °C, held for 60 min, then decreased to 100 °C and held for 15 min. The samples were saturated by flowing 1% NH_3 in argon (30 cc/min) for 60 min at 100 °C and subsequently flushed with helium (30 cc/min) for 70 min. The bed temperature was increased to 650 °C at a ramp rate of 10 °C/min under flowing helium and held for 60 min. During this time, the reactor effluent was monitored by the TCD detector. After each TPD experiment, the detector was calibrated by repeated pulsing of 1% NH_3 in argon through a blank sample loop.

Computational modeling

A representative pseudoamorphous model was constructed by first manually constructing anatase-TiO_2 particulates and then passivating with both protons and $B_{12}O_{12}H_{10/11}$ species to achieve an overall oxidation state of Ti(IV). The model was then initially relaxed using geometrically constrained DFT (PBEsol, 500 eV cutoff, PAW pseudopotentials in VASP), with the B-O-Ti distance allowed to relax. The resultant structure was then subjected to a heat and quench process at a rate of 0.1 K per 5 fs to 300K in a canonical ensemble, yielding one possible orientation of the otherwise amorphous material. Electron energy alignments were computed using HSE06 and a triple zeta basis set, as implemented in Gaussian09. Each cluster was geometrically optimized in its respective oxidation state and the electron energies were aligned to the vacuum from Janak's theorem.

X-ray absorption near edge spectroscopy (XANES)

***Data Collection*:** X-ray absorption measurements were acquired at the Ti K edge (4.9660 keV) on the bending magnet beam line of the Materials Research Collaborative Access Team

(MRCAT) at the Advanced Photon Source, Argonne National Laboratory. The X-ray ring at APS has a current of 102 mA and the beamline has a flux of 5 X 10^{10} photons/s. Photon energies were selected using a water-cooled, double-crystal Si(111) monochromator, which was detuned by approximately 50% to reduce harmonic reflections. The X-ray beam was 0.5×2.5 mm^2 and measurements were made in step-scan transmission mode. Data points were acquired in three separate regions: a pre-edge region (−250 to −50 eV, step size = 10 eV, dwell time = 0.25 s), the XANES region (−50 to -30 eV, step size = 5 eV, dwell time = 0.25 s and -30 to +30 eV, step size = 0.4 eV, dwell time = 0.5 s), and the EXAFS region (0-15 $Å^{-1}$, step size = 0.05 $Å^{-1}$, dwell time = 0.5 s). The ionization chambers were optimized for the maximum current with linear response (~10^{10} photons detected/s) with 10% absorption in the incident ion chamber and 70% absorption in the transmission detector. A third detector in series simultaneously collected a Ti foil reference spectrum with each measurement for energy calibration.

Samples were pressed into a cylindrical sample holder consisting of six wells, forming a self-supporting wafer. To achieve an absorbance (μx) of approximately 1.0, samples were diluted with boron nitride. The sample holder was placed in a quartz reactor tube (1–in. OD, 10–in. length) sealed with Kapton windows by two Ultra-Torr fittings through which gas could be flowed. The reactor was purged with He and measurements were taken at room temperature in He.

Analysis of XAS Data**:** XAS spectra were analyzed using *WinXAS 3.2* software. The data were obtained from -250 eV below the edge to 850 eV above the edge and normalized with linear and cubic fits of the pre-edge and post edge regions, respectively. The oxidation state of each sample was determined by the XANES edge energy as compared to Ti foil, TiO, Ti_2O_3, and TiO_2 reference compounds.

The EXAFS was extracted by performing as cubic spline fit of the normalized absorption spectrum with 5 nodes from 2.0 to 13 Å^{-1}. EXAFS coordination parameters were obtained through a least-squares fit in R-space of the k^2-weighted Fourier transform from 2.8 to 11.4 Å^{-1}. Experimental phase shift and back scattering amplitude fitting functions for Ti-O scattering pairs were determined form TiO_2.

Solid-state ^{11}B MAS NMR

The solid-state ^{11}B MAS NMR measurements at high magnetic field strength were performed on a Bruker AVANCE-III Ultrashield Plus 800 MHz (18.8 T) narrow-bore spectrometer operating at Larmor frequencies of 256.75 and 800.24 MHz for ^{11}B and ^{1}H, respectively, and using a Bruker 3.2 mm broadband Bruker Tri-Gamma H-X-Y probehead. The ^{11}B background signal from the MAS probehead was subtracted from the single-pulse ^{11}B MAS NMR spectra. Spinal-64[53] ^{1}H decoupling was applied during the acquisition period. The ^{11}B shifts were referenced to $BF_3O(CH_2CH_3)_2$ in $CDCl_3$ at 0 ppm, using solid BN as a secondary ^{11}B shift reference and as an external ^{11}B spin counting reference. The ^{11}B spin-lattice (T_1) relaxation times were measured by using a saturation recovery pulse sequence with a rotor-asynchronous saturating pulse train[54] and Hahn-echo acquisition. The resulting ^{11}B saturation recovery signal intensities were fit to a stretched exponential fitting function with a stretched exponent of 0.5, which describes the shape of the distribution of ^{11}B T_1 relaxation times[55]. The ^{11}B{^{1}H} CP-MAS spectra were acquired using a very short ^{11}B-^{1}H contact time of 100 μs to probe hydrated ^{11}B environments. The 2D *J*-mediated NMR spectrum of material **3** was acquired at 18.8 T, 10 kHz MAS, 298 K, and using a direct-excitation INADEQUATE sequence with an experimentally-optimized half-echo τ delay of 0.4 ms.

The low-temperature ^{11}B MAS NMR spectra of material **3** were acquired at 9.4 T, 8 kHz MAS, and 95 K, using a Bruker H-X-Y low-temperature MAS probehead operating at Larmor frequencies of 128.40 and 400.20 MHz for ^{11}B and ^{1}H, respectively. The low-temperature 2D dipolar mediated ^{11}B{^{11}B} spectrum of material **3** was acquired at 4.6 kHz MAS using a CP-mediated spin-refocused $SR26_4^{11}$ dipolar recoupling sequence[56] using an experimentally-optimized recoupling period of 1.74 ms (8 rotor periods) for excitation and reconversion of the double-quantum coherences.

Pair distribution function (PDF) analysis

Total scattering data suitable for PDF analysis were collected at beamline 11-ID-B at the Advanced Photon Source at Argonne National Laboratory using 58.6 keV (0.2115 Å) X-rays. Data were collected using an amorphous silicon area detector at approximately 18 cm from the sample. Calibration of sample-detector distance, detector tilt and reduction of data to one-dimensional patterns were performed using FIT2D. PDFs were obtained from the data with PDFgetX2 to a Q_{max} = 24 Å^{-1}. Structural models were refined against the data in PDFgui.

Electrochemical measurements

All electrochemical experiments were collected using a Biologic VMP3 electrochemical workstation (VMP3b-10), USA Science Instrument. A three-electrode configuration was employed for all of the measurements with a platinum foil counter electrode (Sigma-Aldrich) and Ag/AgCl, 3 M NaCl reference electrode (Bioanalytical Systems Inc., USA). The redox system used for the evaluation of the electron transfer kinetics was 5 mM $K_3[Fe(CN)_6]/K_4[Fe(CN)_6]$ (1:1 molar ratio) dissolved in 1.0 M KCl solution. The working electrodes were material **3**, anatase TiO_2 (Sigma-Aldrich) and rutile TiO_2 (Sigma-Aldrich), material **2**, and pyrolytic graphite, all with a working area of 1 cm^2. The working electrodes were prepared by mixing 80 wt% active materials, 10 wt% carbon black and 10 % (1:1 CMC/SBR) binder in water. The homogeneous solution was drop-cast onto a graphite current collector. The heterogeneous electron transfer rate constant (k_{obs}^{0}) was calculated using a method developed by Nicholson, which relates the peak separation (ΔE_P) to a dimensionless kinetic parameter, ψ, and consequently to k_{obs}^{0} according to the following equation[57]: $\Psi = \frac{(D_O/D_R)^{\alpha/2}k^o}{(\pi D_O v F/RT)^{1/2}}$ where D_O and D_R are the diffusion coefficients of the oxidized and reduced species, respectively. The other variables are α, the transfer coefficient; k^o, the heterogeneous electron transfer rate constant; ν, the scan rate; F, the Faradays constant; R, the general gas constant; T, the temperature. The diffusion coefficients for the oxidized (O) and reduced (R) forms of the solution phase probe redox couple are equal, therefore, $(D_O/D_R)^{\alpha/2}$ ~1. A diffusion coefficient of $[Fe(CN)_6]^{3-/4-}$ is 7.26 x 10^{-6} cm^2/s in 1.0 M KCl electrolyte[58,59].

Assembly of supercapacitors

Both pouch cells and coin cells were assembled to test the capacitive performance of the different materials. Celgard 3501 separator was utilized to complete the assembly of the cells. Supercapacitor electrodes were prepared following the procedure described in the previous section (electrochemical measurement section). A pouch cell was assembled by sandwiching a Celgard separator with two identical pieces of the coated films. This stack is then inserted into an aluminum-laminated bag followed by the addition of some electrolytes. To assemble the coin cells, the electrode films were punched into discs of 14 mm in diameter whereas Celgard 3501 membranes were punched into 17 mm to avoid the shorting of the two electrodes. A stack of electrode 1, separator and electrode 2 was placed into the bottom cap followed by the addition of 500 uL of the electrolyte (1.0 M Na_2SO_4). A stainless steel spacer and a spring were placed on top of that to enable electrical connection with the positive and negative terminals of the pouch cell. Eventually, the top cap is added and the full stack is crimped using CR 2032 coin cell crimper (MTI Corp, United States). All the cells were assembled in the air.

The gravimetric capacitance ($\boldsymbol{C_g}$, mF/g) of each device was calculated from CV curves using the formula below:

$$C_g = \frac{1}{vm\,(V_f - V_i)} \int_{V_i}^{V_f} i(V)dV$$

,where $\boldsymbol{i}$ is the current response (mA), $\boldsymbol{V_f}$- $\boldsymbol{V_i}$ is the potential window (V), $\boldsymbol{v}$ is the scan rate (V/s), and $\boldsymbol{m}$ is the mass of the active materials on both electrodes.

Resistivity measurements

The resistivity measurements were carried out using probe station (Lakeshore Model PS-100 Tabletop Cryogenic Probe Station) under vacuum conditions. The meter is Agilent B2902A Precision Source/Measure Unit. By sweeping the voltage applied on two ends of our material, we obtained the current and voltage curves of 10 different devices. Then, the resistances were determined by calculating the ratio of maximum voltage and corresponding current. After normalizing the resistance with the geometries of our material, we achieved the resistivity and the statistics.

Visible light photocatalytic degradation

The visible light photocatalytic activity of the material **3** was investigated by monitoring the decomposition of the organic dyes Alizarin Red S (ARS), Methylene Blue (MB), and Rhodamine B (RhB) in an aqueous solution under 630 nm red LED light. For the degradation of ARS, 0.050g of material **3** was added to 15 ml solution with a concentration of 20 mg/L, and the suspension was stirred in the dark overnight to reach an equilibrated adsorption of the suspension to the catalyst. In the case of the RhB and the MB, 0.010 g of material **3** was added to 15 mL MB solution with a concentration of 10 and 20 ppm, respectively and the suspensions were stirred in the dark for 1 h before illumination. At given irradiation time intervals (2 h), aliquots of 2.5 ml were taken out, centrifuged, and subsequently filtered through a filter (EMD Millipore, pore size 0.22 μm) to remove any remaining material **3**. The filtrates were then analyzed by UV-Visible spectra with a spectrometer (Shimadzu UV-3101PC). The maximum absorption at 420, 554, and 660 nm was monitored for ARS, RhB and, MB degradation, respectively.

Detection of reactive oxygen species (ROS)

A solution was prepared in a beaker containing 12.5 ppm 1,3-diphenylisobenzofuran (DPBF, Sigma) in acetonitrile. After irradiating for 2 h under visible light (630 nm red LED) for stabilization, 10 mg of material **2** and **3** was added to 80 ml of DPBF solution, respectively. The system was opened to air and subsequently aerated to provide more oxygen. At given time intervals, aliquots were collected and their absorbance was recorded at 410 nm.

Data availability

All data generated or analysed during this study are included in this published article (and its supplementary information files).

References

1. Jaffe, R. L. *et al.* Energy critical elements: securing materials for emerging technologies. (Materials Research Society/American Physical Society, Washington D. C., 2011).
2. Reddy, M. V., Subba Rao, G. V., Chowdari, B. V. R. Metal oxides and oxysalts as anode materials for Li ion batteries. *Chem. Rev.* **113,** 5364-5457 (2013).
3. McFarland, E. W. & Metiu, H. Catalysis by doped oxides. *Chem. Rev.* **113,** 4391–4427 (2013)
4. Chen, X. & Mao, S. S. Titanium dioxide nanomaterials: Synthesis, properties, modifications, and applications. *Chem. Rev.* **107,** 2891−2959 (2007).
5. Asahi, R., Morikawa, T., Irie, H., Ohwaki, T. Nitrogen-doped titanium dioxide as visible-light-sensitive photocatalyst: designs, developments, and prospects. *Chem. Rev.* **114,** 9824−9852 (2014).
6. Kapilashrami, M., Zhang, Y., Liu, Y.-S., Hagfeldt, A., Guo, J. Probing the optical property and electronic structure of TiO_2 nanomaterials for renewable energy applications. *Chem. Rev.* **114,** 9662–9707 (2014).
7. Schneider, J. *et al.* Understanding TiO_2 photocatalysis: mechanism and materials. *Chem. Rev.* **114,** 9919–9986 (2014).
8. Fujishima, A. & Honda, K. Electrochemical photolysis of water at a semiconductor. *Nature* **238,** 37−38 (1972).
9. Ma, Y. *et al.* Titanium dioxide-based nanomaterials for photocatalytic fuel generations. *Chem. Rev.* **114,** 9987–10043 (2014).
10. Bai, Y., Mora-Seró, I., De Angelis, F., Bisquert, J., Wang, P. Titanium dioxide nanomaterials for photovoltaic applications. *Chem. Rev.* **114,** 10095–10130 (2014).
11. Khan, S. U. M., Al-Shahry, M., Ingler Jr., W. B. Efficient photochemical water splitting by a chemically modified n-TiO_2. *Science* **297,** 2243–2245 (2002).

12. Chen, X., Liu, L., Yu, P. Y., Mao, S. S. Increasing solar absorption for photocatalysis with black hydrogenated titanium dioxide nanocrystals. *Science* **331,** 746−750 (2011).

13. Chen, X., Liu, L., Huang, F. Black titanium dioxide (TiO_2) nanomaterials. *Chem. Soc. Rev.* **44,** 1861–1885 (2015).

14. Salzmann, I. & Heimel, G. Toward a comprehensive understanding of molecular doping organic semiconductors. *J. Electron. Spectrosc. Relat. Phenom.* **204,** 208–222 (2015).

15. Pitochelli, A. R. & Hawthorne, M. F. The isolation of the icosahedral $B_{12}H_{12}^{-2}$ ion. *J. Am. Chem. Soc*. **82,** 3228−3229 (1960).

16. Spokoyny, A. M. New ligand platforms featuring boron-rich clusters as organomimetic substituents. *Pure Appl. Chem.* **85,** 903−919 (2013).

17. Sivaev, I. B., Bregadze, V. I., Sjöberg, S. Chemistry of closo-dodecaborate anion $[B_{12}H_{12}]^{2-}$: a review. *Collect. Czech. Chem. Commun.* **67,** 679–727 (2002).

18. Hawthorne, M. F. & Pushechnikov, A. Polyhedral borane derivatives: unique and versatile structural motifs. *Pure Appl. Chem.* **84,** 2279–2288 (2012).

19. Dash, B. P., Satapathy, R., Maguire, J. A., Hosmane, N. S. Polyhedral boron clusters in materials science. *New J. Chem.* **35,** 1955–1972 (2011).

20. Hansen, B. R. S., Paskevicius, M., Li, H-.W., Akiba, E., Jensen, T. R. Metal boranes: progress and applications. *Coord. Chem. Rev.* **323,** 60–70 (2016).

21. Cheng, F., Jäkle, F. Boron-containing polymers as versatile building blocks for functional nanostructured materials. *Polym. Chem.* **2,** 2122–2132 (2011).

22. Núñez, R., Romero, I., Teixidor, F., Viñas, C. Icosahedral boron clusters: a perfect tool for the enhancement of polymer features. *Chem. Soc. Rev.* **45,** 5147–5173 (2016).

23. Alexandrova, A. N., Boldyrev, A. I., Zhai, H.-J., Wang, L.-S.. All-boron aromatic clusters as potential new inorganic and building blocks in chemistry. *Coord. Chem. Rev.* **250,** 2811–2866 (2006).

24. Muetterties, E. L. Boron hydride chemistry. (Academic Press, New York, 1975).

25. Farha, O. K. *et al*. Synthesis of stable dodecaalkoxy derivatives of hypercloso–$B_{12}H_{12}$. *J. Am. Chem. Soc*. **127,** 18243−18251 (2005).

26. Wixtrom, A. I. *et al.* Rapid synthesis of redox-active dodecaborane $B_{12}(OR)_{12}$ clusters under ambient conditions. *Inorg. Chem. Front*. **3,** 711−717 (2016).

27. Messina, M. S. *et al.* Visible-light induced olefin activation using 3D aromatic boron-rich cluster photooxidants. *J. Am. Chem. Soc.* **138,** 6952–6955 (2016).

28. Qian, E. A. *et al.* Atomically precise organomimetic cluster nanoparticles assembled via perfluoroaryl-thiol S_NAr chemistry. *Nature Chem.* **9,** 333–340 (2017).

29. Pan, L. *et al.* Hierarchical nanostructured conducting polymer hydrogel with high electrochemical activity. *Proc. Natl. Acad. Sci. U.S.A.* **109,** 9287–9292 (2012).

30. To, J. W. F. *et al.* Ultrahigh surface area three-dimensional porous graphitic carbon from conjugated polymeric molecular framework. *ACS Cent. Sci.* **1,** 68–76 (2015).

31. Mirabelli, M. G. L. & Sneddon, L. G. Synthesis of boron carbide via poly(vinylpentaborane) precursors. *J. Am. Chem. Soc.* **110,** 3305–3307 (1988).

32. Su, K. & Sneddon, L. G. A polymer precursor route to metal borides, *Chem. Mater.* **5,** 1659–1668 (1993).

33. Feng, N. *et al.* Boron environments in B-doped and (B,N)-codoped TiO_2 photocatalysts: a combined solid-state NMR and theoretical calculation study, *J. Phys. Chem. C* **115,** 2709–1719 (2011).

34. Barrow, N. S. *et al.* Towards homonuclear *J*-solid-state NMR correlation experiments for half-integer quadrupolar nuclei: experimental and simulated ^{11}B MAS spin-echo dephasing and calculated $^2J_{BB}$ coupling constants for lithium diborate. *Phys. Chem. Chem. Phys.* **13,** 5778–5789 (2011).

35. Billing, S. J. L. & Kanatzidis, M. G. Beyond crystallography: the study of disorder, nanocrystallinity and crystallographically challenged materials with pair distribution functions. *Chem. Commun.* 749–760 (2004)

36. Lee, M. W., Farha, O. K., Hawthorne, M. F., Hansch, C. H. Alkoxy derivatives of dodecaborate: discrete nanomolecular ions with tunable pseudometallic properties. *Angew. Chem. Int. Ed.* **46,** 3018–3022 (2007).

37. Van, N. *et al.* Oxidative perhydroxylation of [closo-$B_{12}H_{12}$]$^{2-}$ to the stable inorganic cluster redox system [$B_{12}(OH)_{12}$]$^{2-/.-}$: experiment and theory. *Chem. Eur. J.* **16,** 11242–11245 (2010).

38. Li, Y. *et al.* An oxygen reduction electrocatalyst based on carbon nanotube-graphene complexes. *Nature nanotechnology* **7**, 394–400 (2012).

39. Guo, Y. –G., Hu, Y. –S., Sigle, W., Maier, J. Superior electrode performance of nanostructured mesoporous TiO_2 (anatase) through efficient hierarchical mixed conducting networks. *Adv. Mater.* **19,** 2087–2091 (2007).

40. Jiang, C., Hosono, E., Zhou, H. Nanomaterials for lithium ion batteries. *Nano Today* **1,** 28–33 (2006).

41. Gomes, A., Fernandes, E., Lima, J. L. F. C. Fluorescence probes used for detection of reactive oxygen species. *J. Biochem. Biophys. Methods* **65,** 45–80 (2005).

42. Yin, Q. *et al.* A fast soluble carbon-free molecular water oxidation catalyst based on abundant metals. *Science* **328,** 342–345 (2010).

43. Yan, H. et al. Hybrid metal-organic chalcogenide nanowires with electrically conductive inorganic core through diamondoid-directed assembly. *Nat. Mater.* **16,** 349–355 (2017).

44. Bag, S., Trikalitis, P. N., Chupas, P. J., Armatas, G. S., Kanatzidis, M. G. Porous semiconducting gels and aerogels from chalcogenide clusters. *Science* **317,** 490–493 (2007).

45. Song, J. *et al.* A multiunit catalyst with synergistic stability and reactivity: a polyoxometalate-metal organic framework for aerobic decontamination. *J. Am. Chem. Soc.* **133,** 16839–16846 (2011).

46. Yaghi, O. M., Li, G., Li, H. Selective binding and removal of guests in a microporous metal-organic framework. *Nature* **378,** 703–706 (1995).

47. Bachman, J. E., Smith, Z. P., Li, T., Xu, T., Long, J. R. Enhanced ethylene separation and plasticization resistance in polymer membranes incorporating metal-organic framework nanocrystals. *Nature Mater.* **15,** 845–849 (2016).

48. Wang, C., Xie, Z., deKrafft, K. E., Lin, W. Doping Metal-Organic Frameworks for water oxidation, carbon dioxide reduction and organic photocatalysis. *J. Am. Chem. Soc. 133*, 13445–13454 (2011).

49. Goellner, J. F., Gates, B. C., Vayssilov, G. N., Rösch, N. Structure and bonding of a site-isolated transition metal complex: rhodium dicarbonyl in highly dealuminated zeolite Y. *J. Am. Chem. Soc.* **122,** 8056–8066 (2000).

50. Wixtrom, A. I. *et al.* Rapid synthesis of redox-active dodecaborane $B_{12}(OR)_{12}$ clusters under ambient conditions. *Inorg. Chem. Front*. **3,** 711−717 (2016).

51. Pryor Jr. A. *et al.* GENFIRE: A generalized Fourier iterative reconstruction algorithm for high-resolution 3D imaging. arXiv:1706.04309 (2017).

52. Yang, Y. *et al*. Deciphering chemical order/disorder and material properties at the single-atom level. *Nature* **542,** 75–79 (2017).

53. Fung, B. M., Khitrin, A. K., Ermolav, K. An improved broadband decoupling sequence for liquid crystals and solids. *J. Magn. Reson*. **142,** 97–101 (2000).

54. Yesinowski, J. P. Finding the true-spin-lattice relaxation time for half-integral nuclei with non-zero quadrupolar couplings. *J. Mag. Reson.* **252,** 135–144 (2015).

55. Johnston, D. C. Stretched exponential relaxation arising from a continuous sum of exponential decays, *Phys. Rev. B*. **74,** 184430 (2006).

56. Brouwer, D. H., Kristiansen, P. E., Fyfe, C. A., Levitt, M. H. Symmetry-based ^{29}Si dipolar recoupling magic angle spinning NMR spectroscopy: a new method for investigating three-dimensional structures of zeolite frameworks. *J. Am. Chem. Soc.* **127,** 542–543 (2005).

57. Nicholson, R. S. Theory and application of cyclic voltammetry for measurement of electrode reaction kinetics. *Anal. Chem*. ***37*****,** 1351–1355 (1965).

58. Moldenhauer, J., Meier, M., Paul, D. W. Rapid and direct determination of diffusion coefficients using microelectrode arrays. *J. Electrochem. Soc*. **163**, H672–H678 (2016).

59. Konopka, S. J. & Bruce M. Diffusion coefficients of ferri-and ferrocyanide ions in aqueous media, using twin-electrode thin-layer electrochemistry. *Anal. Chem.* **42**, 1741–1746 (1970).

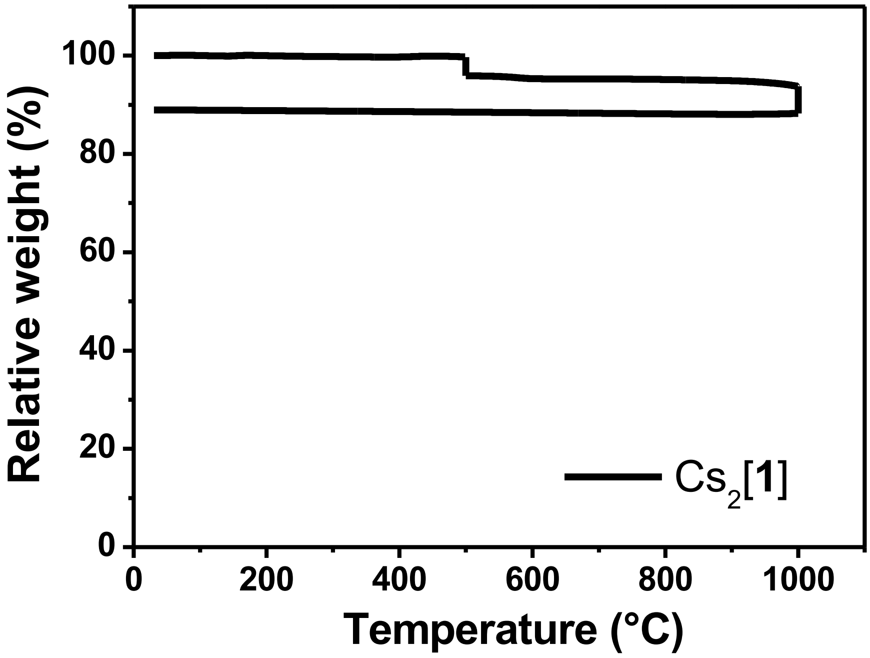

Fig. S1.
TGA analysis of Cs_2[**1**].

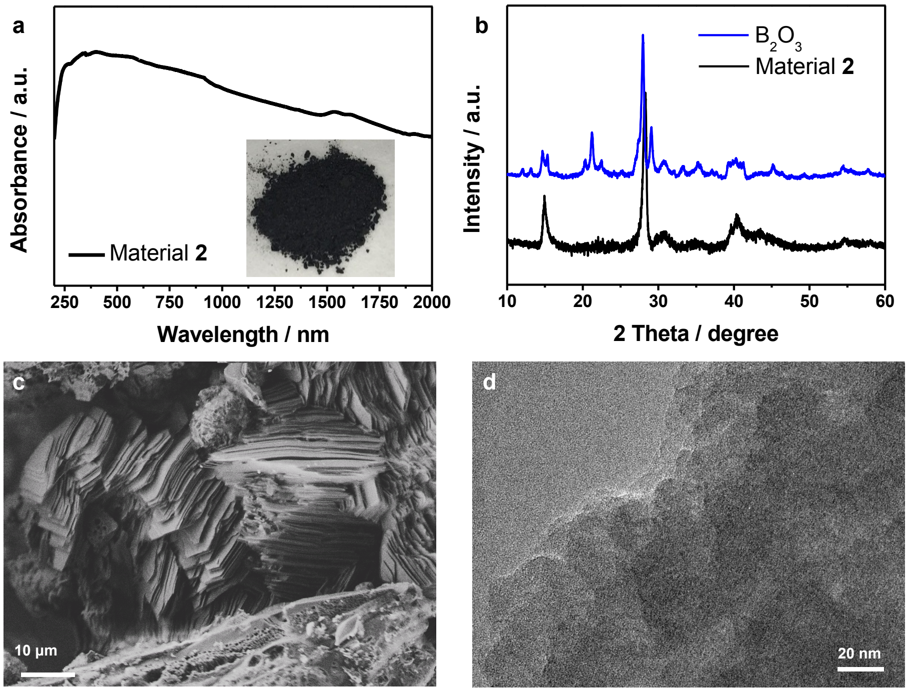

Fig. S2.

Characterization of material **2**. (**a**) Diffuse reflectance UV-Vis spectroscopy of **2**, showing absorption out to the near-IR range; (**b**) PXRD pattern of **2**, with B_2O_3 control; (**c**) SEM image of **2**; (**d**) TEM image of **2,** being consistent with the PXRD data in suggesting no long range order present.

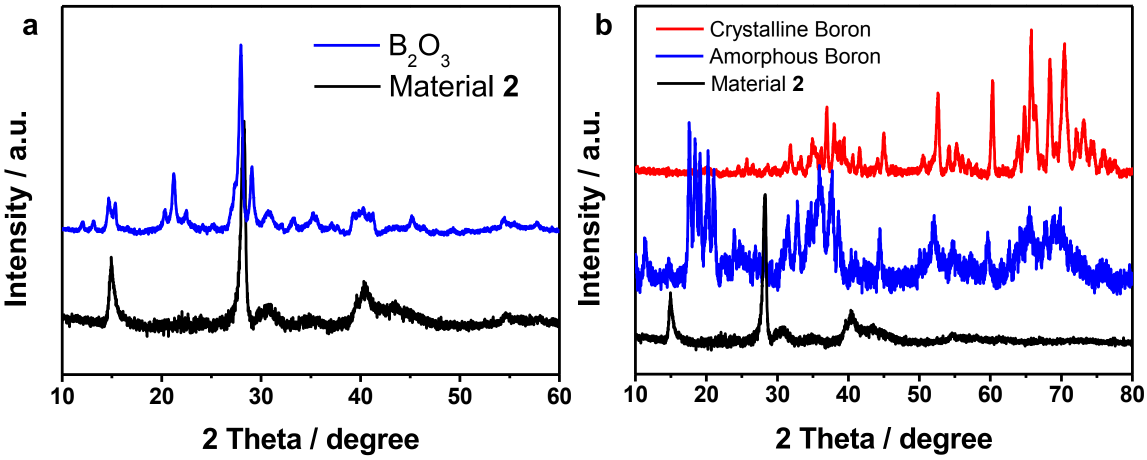

Fig. S3.

PXRD of material **2** with B_2O_3, crystalline and amorphous elemental boron controls. (**a**) B_2O_3 and **2**; (**b**) crystalline and amorphous elemental boron and **2**.

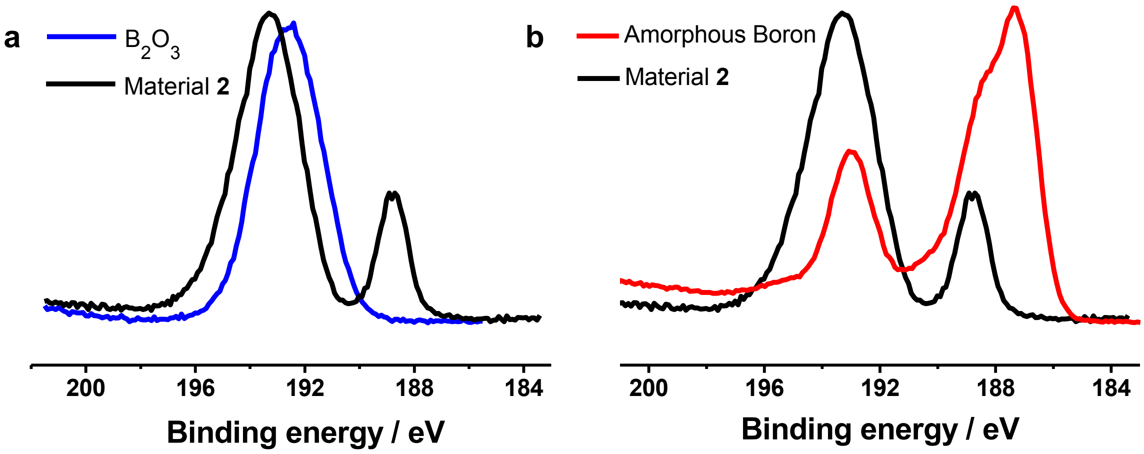

Fig. S4.

XPS of material **2** showing the boron 1*s* region, with B_2O_3 and amorphous elemental boron included as controls. (**a**) boron 1*s* region of B_2O_3 and material **2.** Two peaks are observed in the boron 1*s* region for **2** corresponding to intact clusters (188.8 eV) and a form of boron oxide at higher energy (193.3 eV), and excludes the presence of elemental boron.; (**b**) boron 1*s* region amorphous elemental boron and **2**.

% Found	**C**	**H**	**N**
Trial 1	3.99	4.97	0.73
Trial 2	4.06	5.08	0.73

Table S1.

Combustion analysis of material **2**. It confirms the presence of ~ 4 % carbon in the material, assigned as graphitic carbon based on the XPS binding energy. The appearance of graphitic carbon suggests a likely templating effect imposed by the clusters, reminiscent of the cross-linked "molecular frameworks" recently reported by Bao and co-workers[1,2], albeit with significantly lower carbon content in the case of **2**.

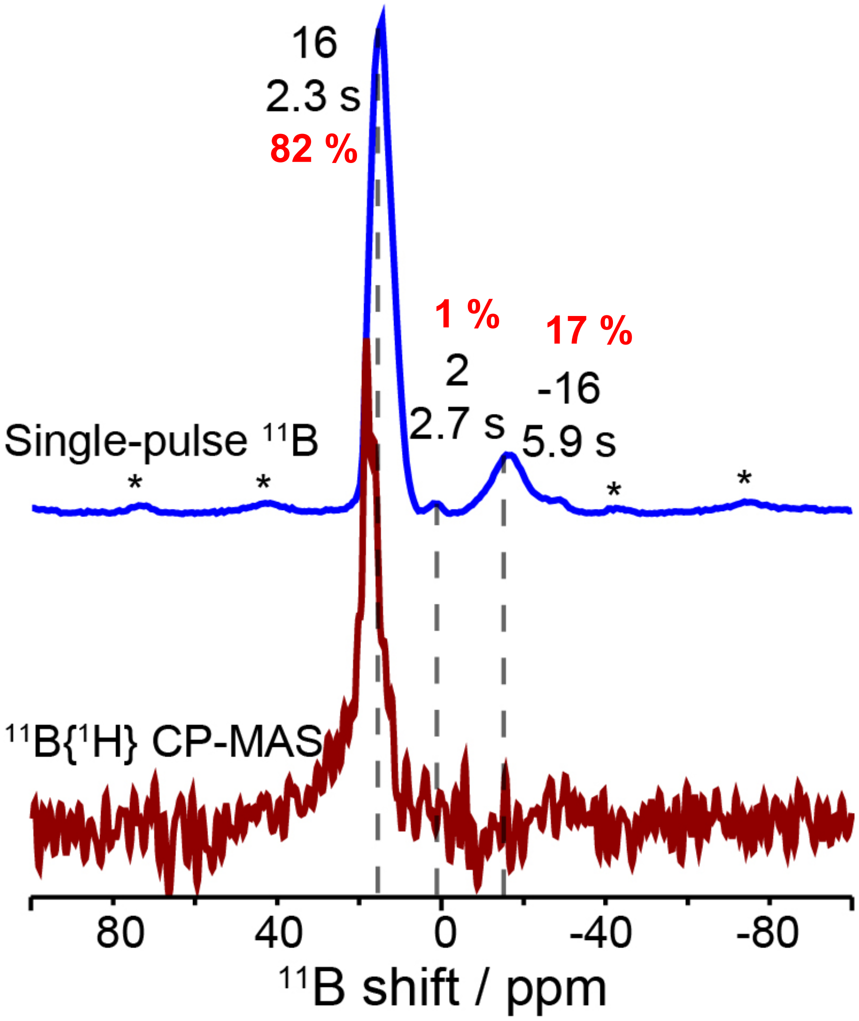

Fig. S5.

Solid-state 1D single-pulse ^{11}B MAS NMR (top) and ^{11}B{^{1}H} CP-MAS (bottom) spectra of material **2**, acquired at 18.8 T and 298 K. A single ^{11}B signals at -16 and 2 ppm are detected from the molecular B_{12}-based clusters. ~80 % of the boron content is in the oxidized form.

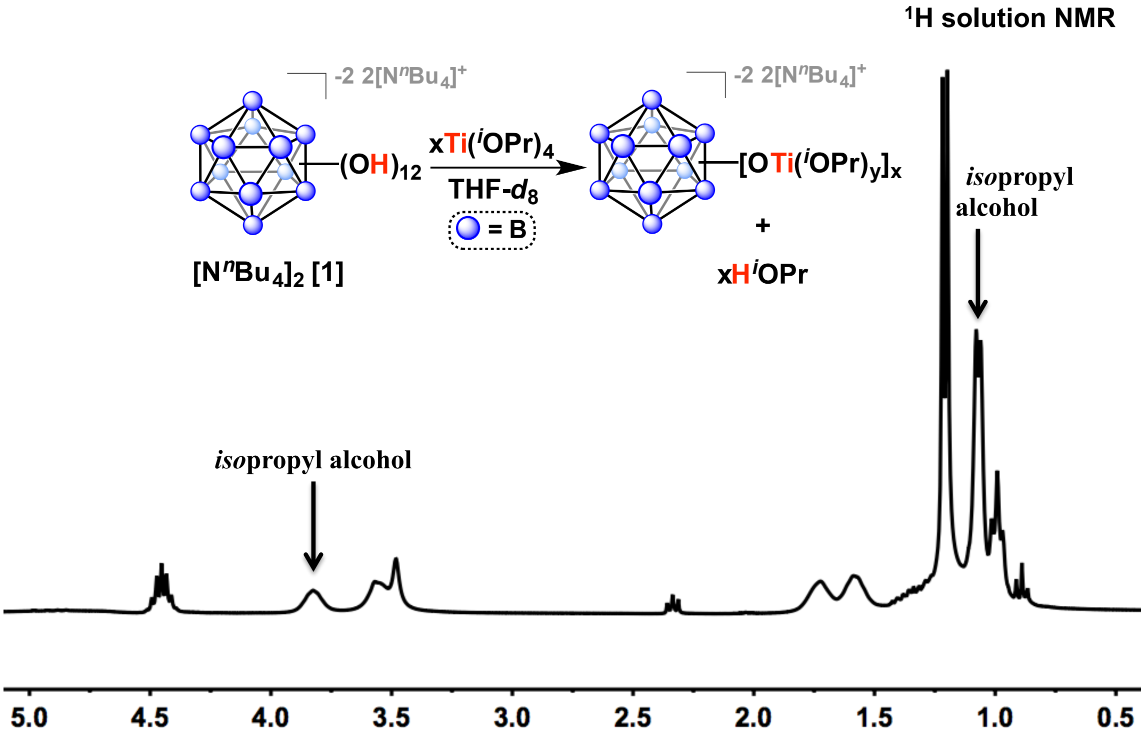

Fig. S6.

^{1}H solution NMR of the test reaction of $Ti(O^iPr)_4$ with $[N^nBu_4]_2$[**1**] in THF-d_8. A solution of $Ti(O^iPr)_4$ (31 mg, 0.03 mL, 0.11 mmol) in THF-d_8 (0.3 mL) was added to a suspension of $[N^nBu_4]_2$[**1**] (15 mg, 0.018 mmol) in THF-d_8 (0.3 mL). The resultant orange mixture was allowed to stir for 2 h at room temperature. The sample was then transferred to an NMR tube with a J. Young Teflon valve for the ^{1}H solution NMR experiment. Peaks associated with *iso*propyl alcohol (marked with arrows) can be observed, indicating formation of B-O-Ti bonds.

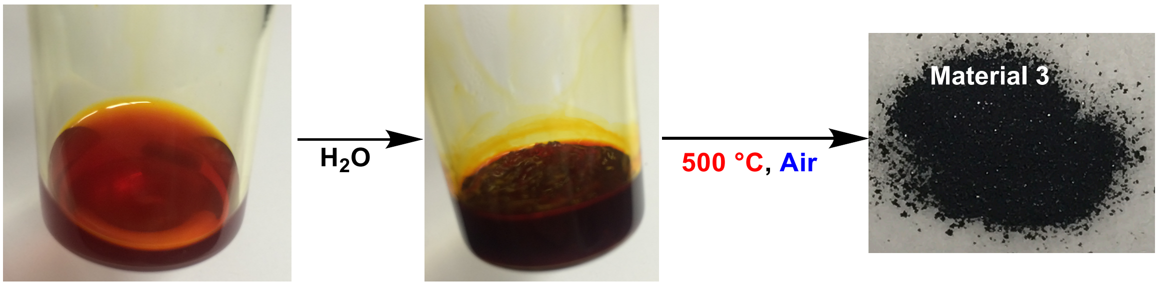

Fig. S7.

A reaction of $[N^nBu_4]_2$[**1**] with $Ti(O^iPr)_4$ in THF. It produces a clear red-orange solution, which is subsequently hydrolyzed to form a red-orange gel. After calcining at 120 °C, the now dark orange solid is annealed at 500 °C in air to produce material **3** as a shiny black solid.

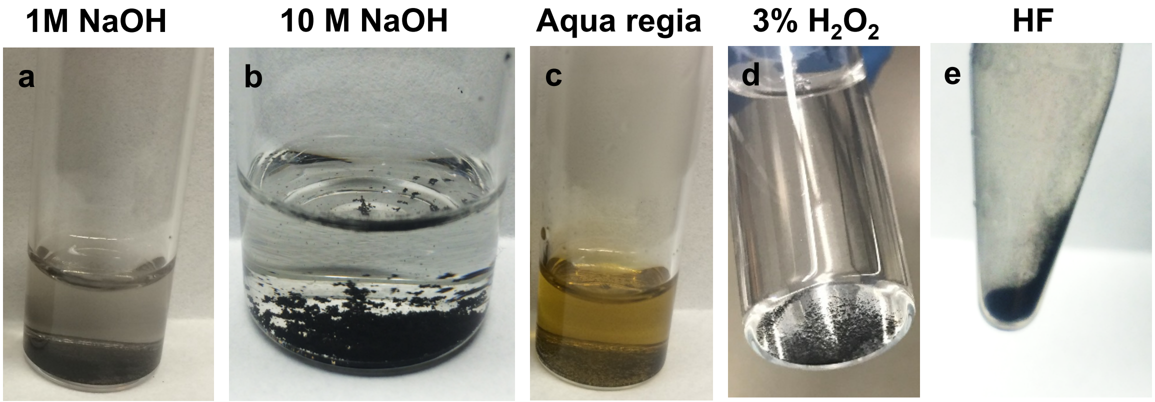

Fig. S8.

Chemical stability test of material **3** in (a) 1M NaOH; (b) 10 M NaOH; (c) Aqua regia; (d) 3 % H_2O_2; (e) HF. **3** resisted prolonged exposure to a variety of strong acids, bases, and 3 % H_2O_2 consistent with its hypothesized highly cross-linked composition.

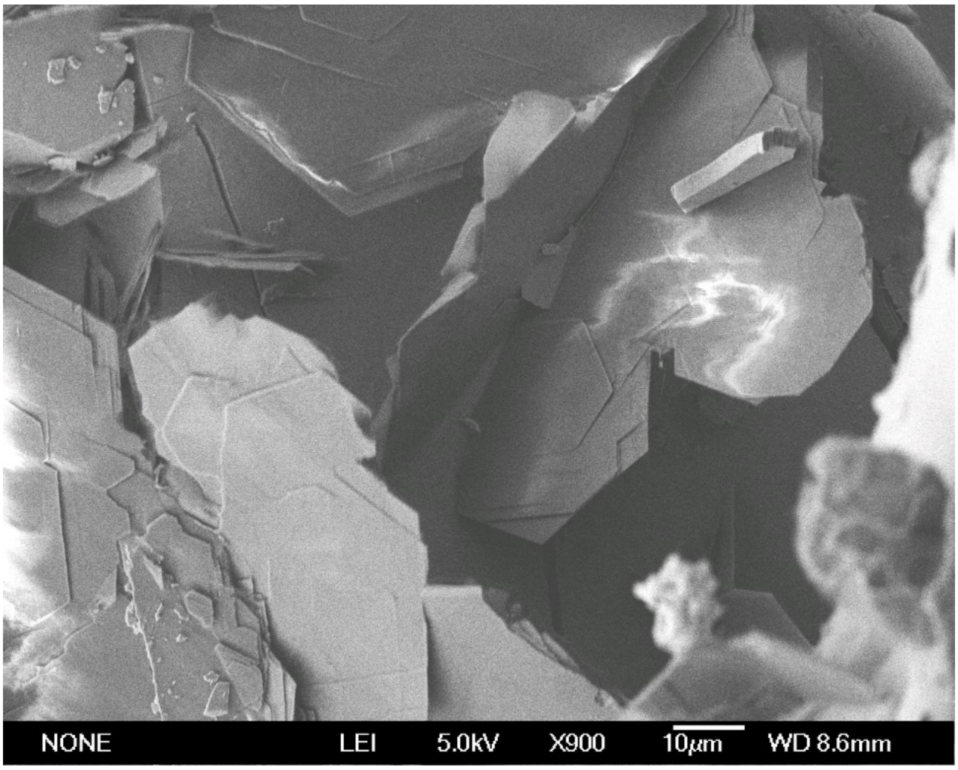

Fig. S9.

SEM image of material **3**.

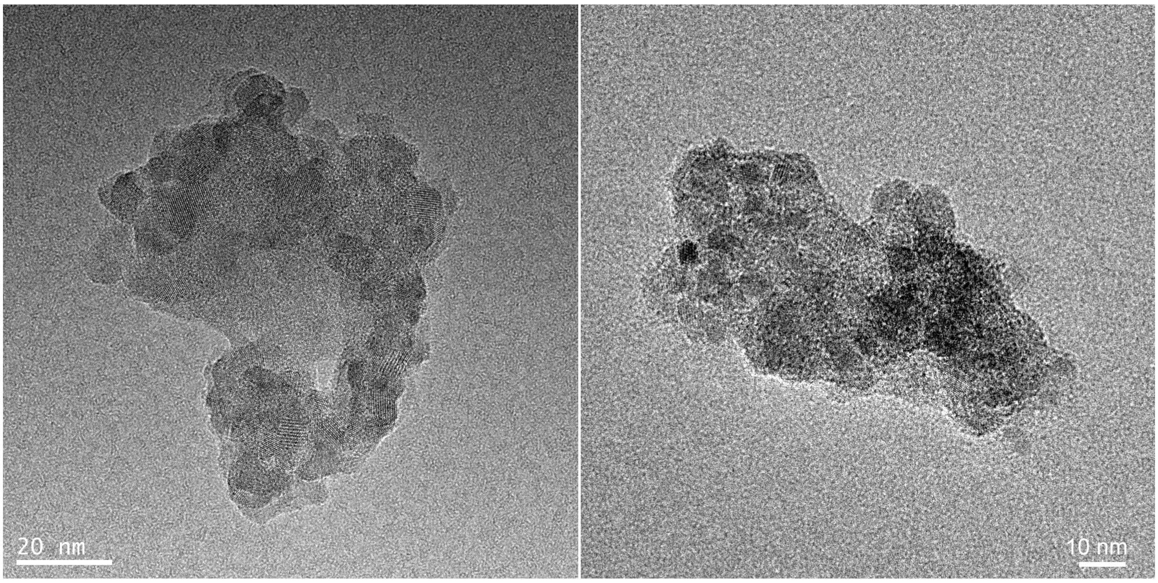

Fig. S10.

High-resolution TEM images of **3** after ball-milled into ~100 nm. Even smaller pieces of **3** still contain TiO_2 nanocrystals embedded in amorphous B_{12}-based clusters.

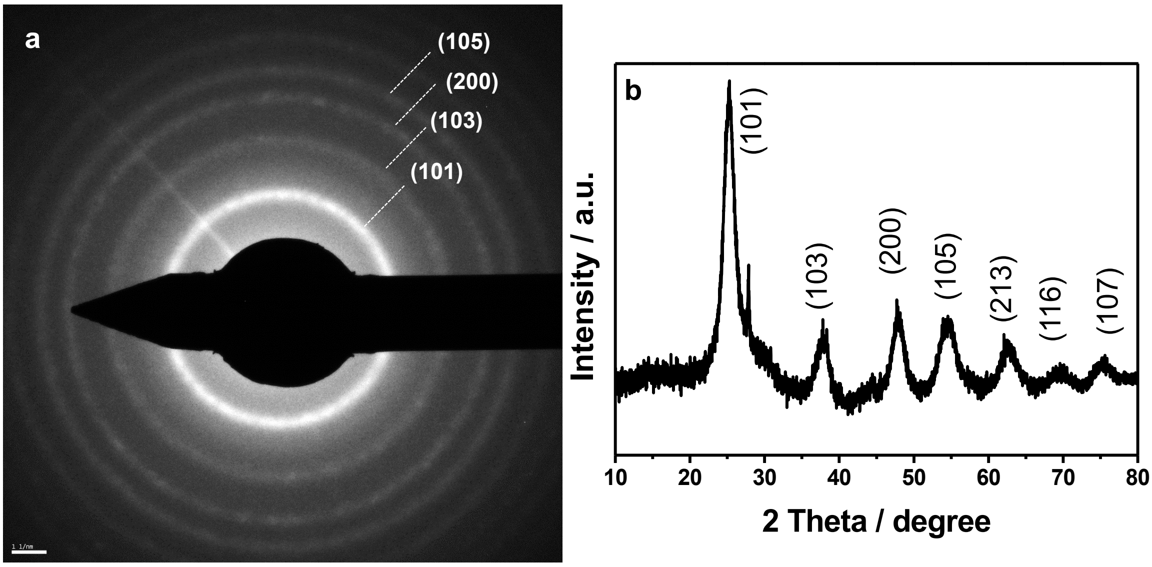

Fig. S11.

(**a**) Selected area electron diffraction (SAED) pattern of material **3**, confirming polycrystalline nature of the material. The individual diffraction rings can be indexed to anatase phase of TiO_2; (**b**) PXRD pattern for **3**, consistent with SAED assignment.

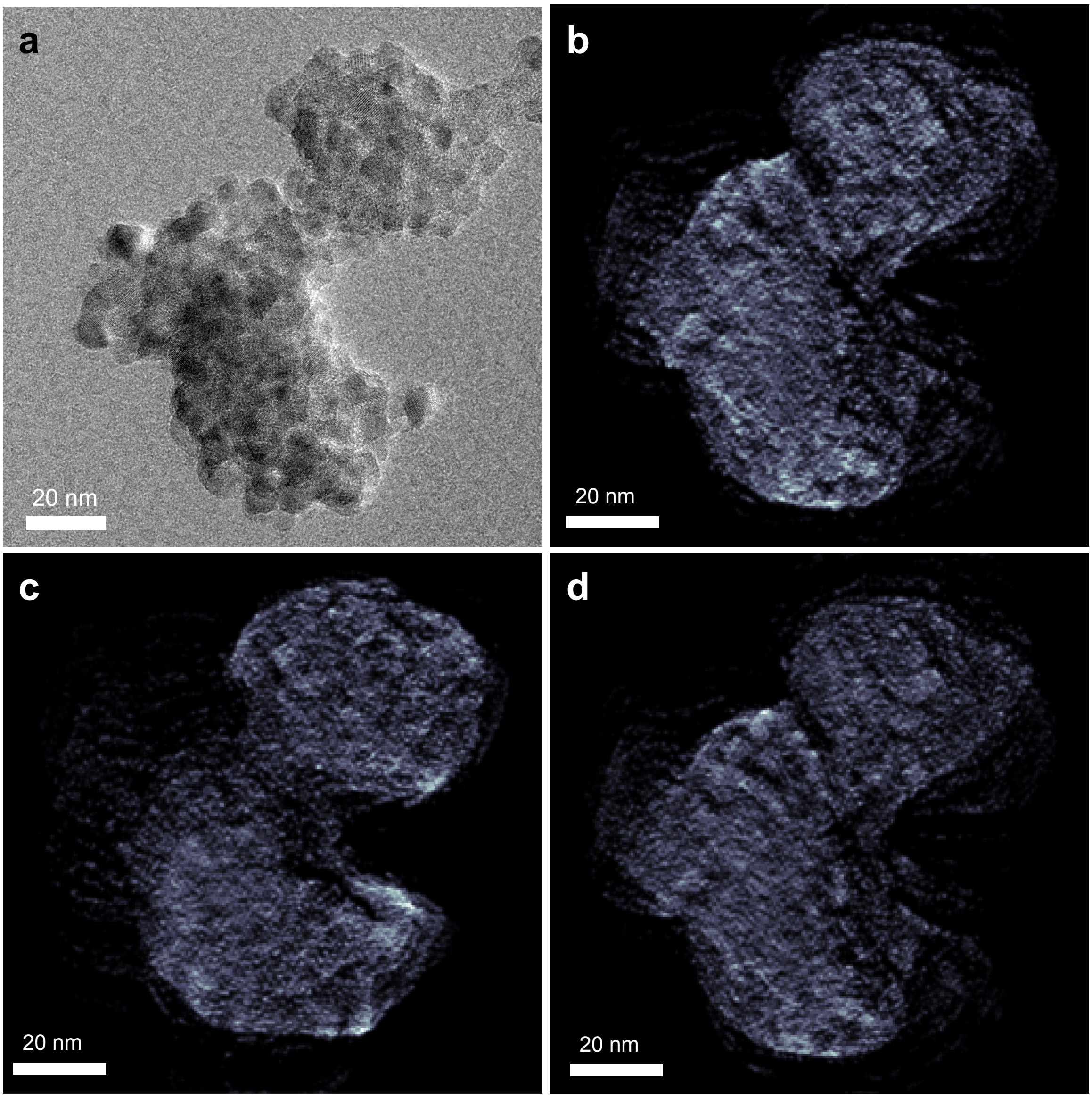

Fig. S12.

(**a**) High-resolution TEM image of **3**. (**b-d**) The middle slice images of the 3D reconstructed density of **3** shown in (**a**) as viewed from different angles.

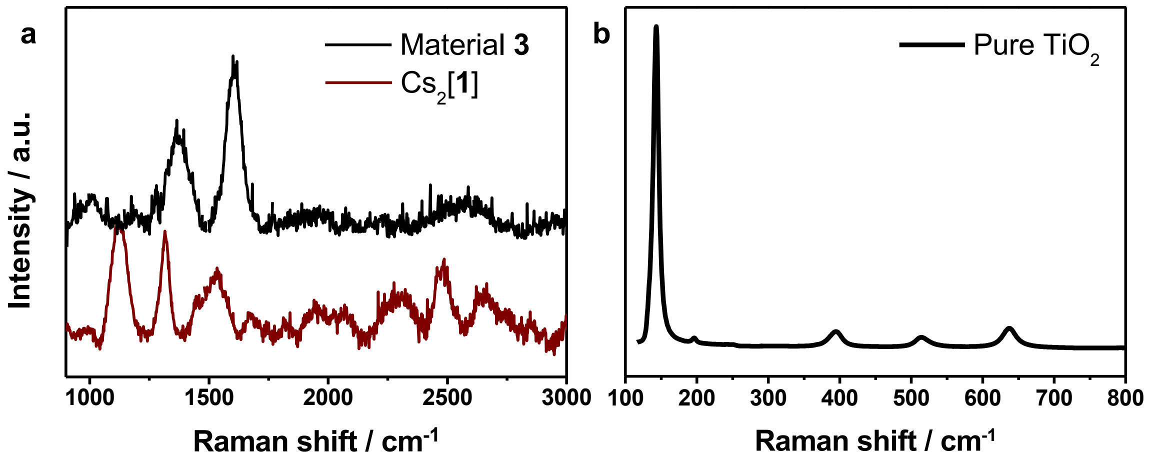

Fig. S13.

Raman spectra of (**a**) Cs_2[**1**] and material **3**. No vibrational modes were observed below 1000 cm^{-1}, which is where modes associated with TiO_2 would be seen; (**b**) Raman of a sample of commercial TiO_2 for reference.

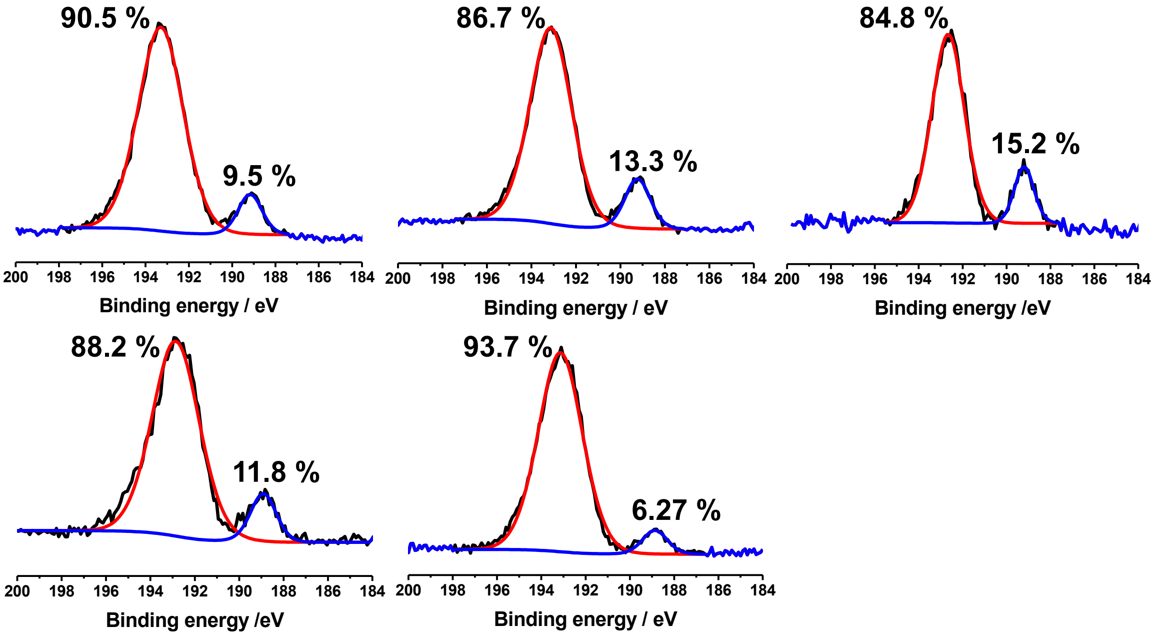

Fig. S14.

XPS obtained from five different material **3** samples, showing the boron 1*s* region. On average, 10 % of the boron content is intact clusters and 90 % of it is in oxidized form at the surface.

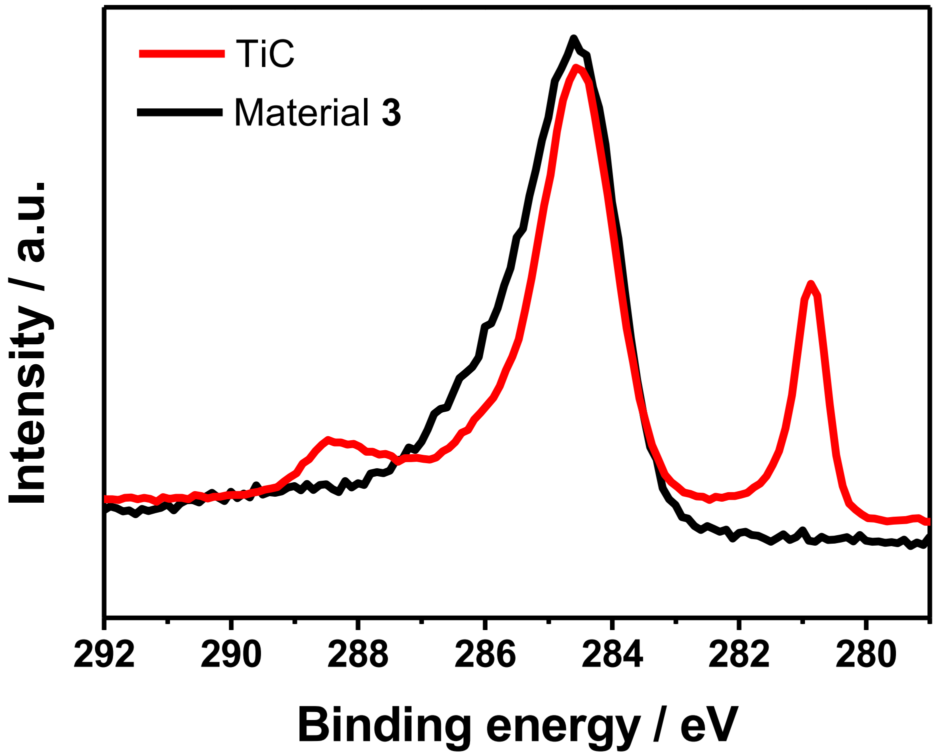

Fig. S15.

XPS for material **3**, looking at the carbon 1*s* region. While graphitic carbon can be observed, a titanium carbide (TiC) control confirms no TiC in **3**.

% Found	C	H	N
6 h reaction	8.72	2.03	0.98
20 h reaction	9.42	0.43	1.19

Table S2.

Combustion analysis of material **3** depending on the reaction time, showing the carbon content in **3** is independent of the reaction time.

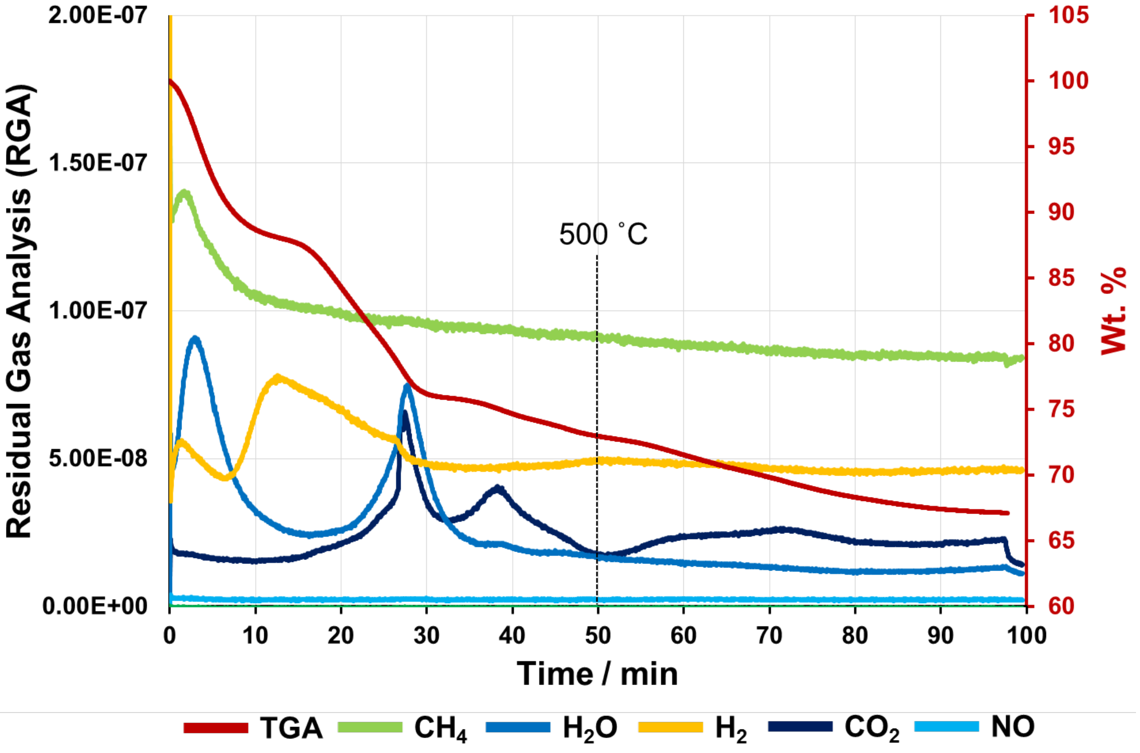

Fig. S16.

TGA-mass spectroscopy (TGA-MS) of pre-annealed material **3**. (A heating rate of 10 °C min^{-1} was used, therefore the scale can be read as: 10 mins= 100 °C) Several different mass loss events are observed between room temperature and 450 °C, where water and then CO_2 are released in distinct phases. Between 450 °C and 550 °C however, production of CO_2 stops, and then begins again at >550 °C, with only concomitant minor mass loss.

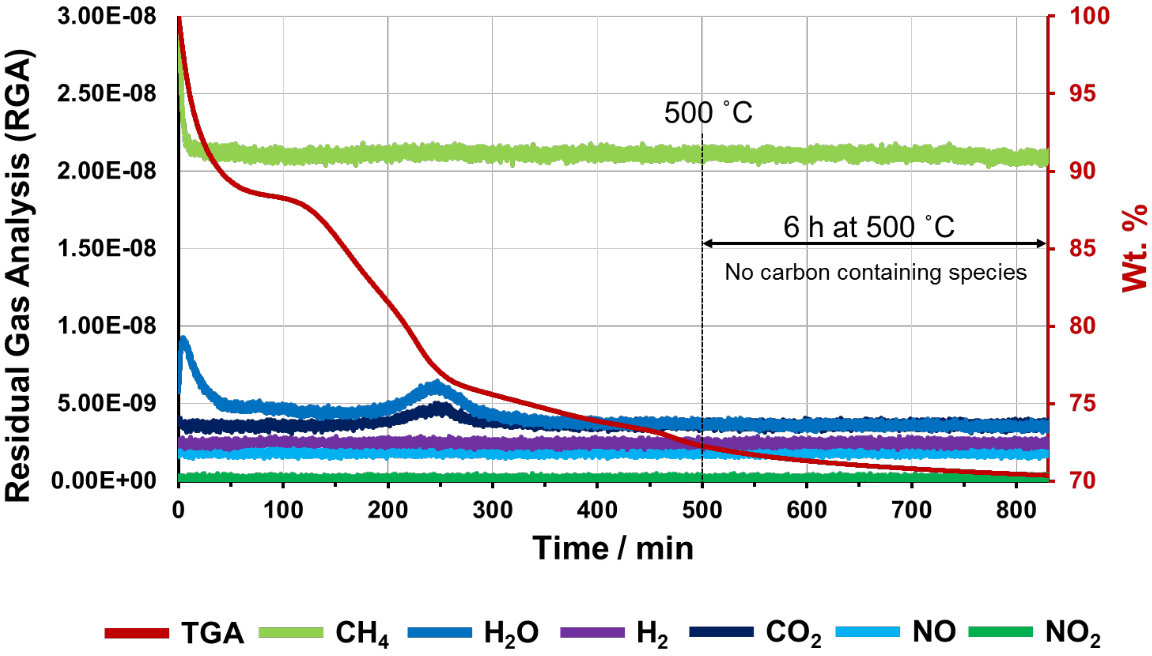

Fig. S17.

TGA-mass spectroscopy (TGA-MS) of pre-annealed material **3**, using the exact synthetic conditions: heating from room temperature to 500 °C at a rate of 1°C/min and holding at 500 °C for six hours. No carbon containing species are released during the annealing process, indicating remaining carbons are entrapped in **3**.

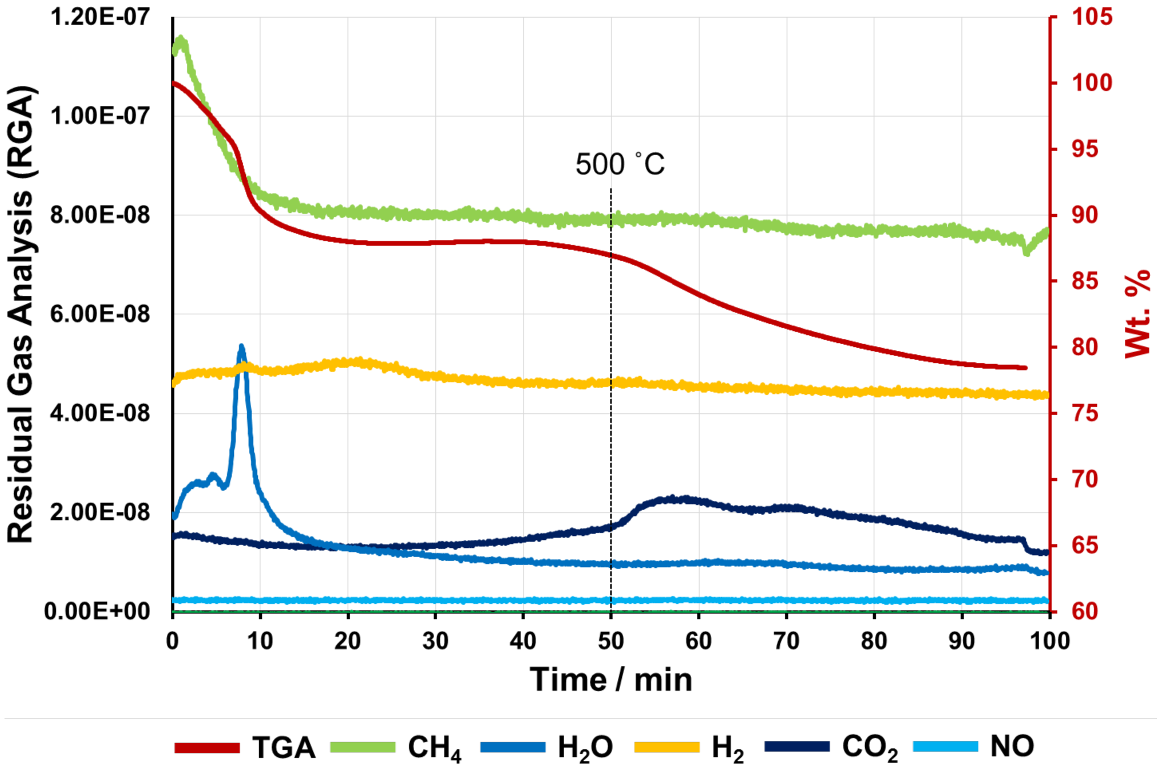

Fig. S18.

TGA-mass spectroscopy (TGA-MS) of material **3**, showing the different mass loss events during the annealing process to form **3**. (A heating rate of 10 °C min^{-1} was used, therefore the scale can be read as: 10 mins = 100 °C)

	Elemental Compositions in Atomic %			
	C	**B**	**O**	**Ti**
1	44.7	10.5	37.3	7.5
2	42.3	13.8	37.6	6.3
3	32.3	10.9	45.9	10.9
4	32.7	10.9	44.9	11.5
Ave.	**38.0**	**11.5**	**41.4**	**9.1**

Table S3.

Elemental compositions in material **3** by TEM/EDX in atomic %. The high percentage of carbon is due to the carbon-based TEM grid.

Sample	Pre-edge energy / keV	Edge energy / keV	$N_{Ti\text{-}O}$	R / Å	$\Delta\sigma^2$ (x 10^3)	E_o / eV	Comments
TiO_2	4.9689, 4.9718, 4.9743	4.9785	6	1.96	0	-0.4	Ti(IV) Ref
Ti_2O_3	-	4.9678	-	-	-	-	Ti(III) Ref
TiO	-	4.9668	-	-	-	-	Ti(II) Ref
TiC	-	4.9668	-	-	-	-	Ti(II)
TiB_2	-	4.9677	-	-	-	-	Ti(III)
Ti foil	-	4.9660	-	-	-	-	Calibration
Material **3**	4.9690, 4.9707, 4.9741	4.9790	4.2	1.95	3.0	-0.3	Ti(IV)

Table S4.

Table showing the summary of the results from XANES and EXAFS for material **3** and several reference materials. The XANES of pre-edge peaks and edge energy of **3** are consistent with Ti(IV) oxide.

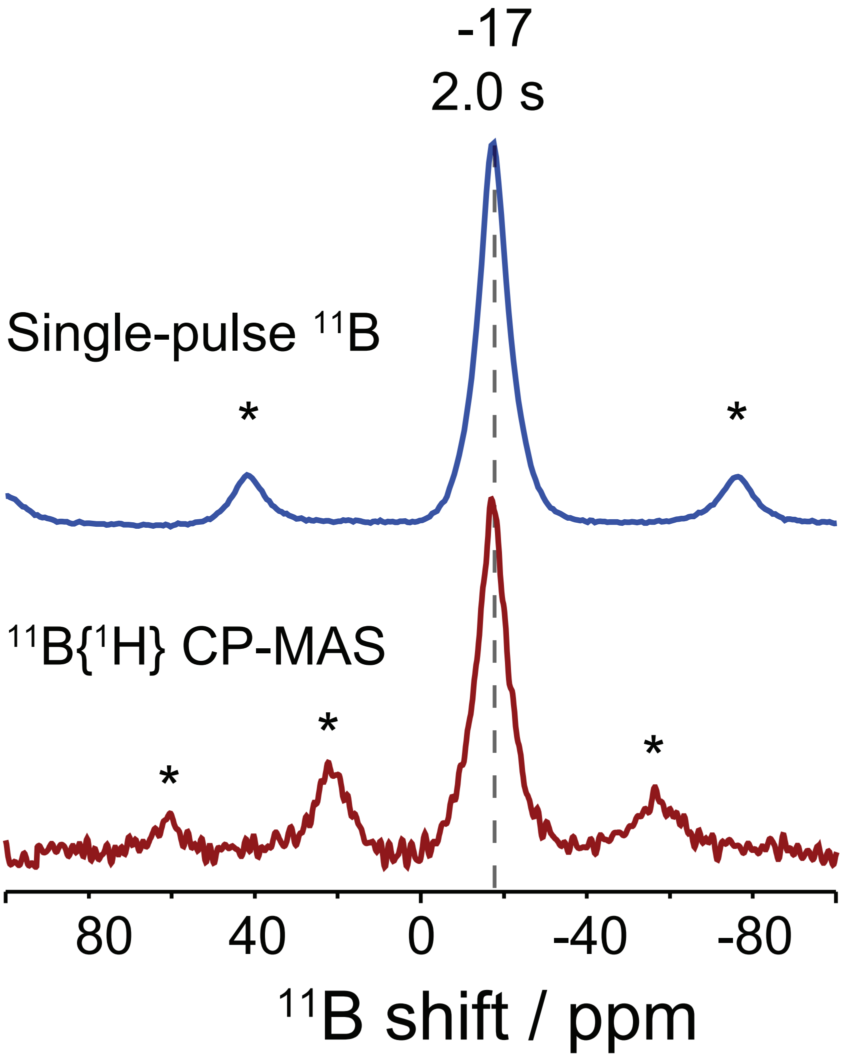

Fig. S19.

Solid-state 1D single-pulse ^{11}B MAS NMR (top) and ^{11}B{^{1}H} CP-MAS (bottom) spectra of a reference material containing intact B_{12} clusters, Cs_2[**1**], acquired at 18.8 T and 298 K. A single ^{11}B signal (9 ppm FWHM) at -17 ppm is detected from the molecular B_{12} clusters. The ^{11}B spin-lattice relaxation behavior of Cs_2[**1**] showed no signs of paramagnetic interactions and the ^{11}B T_1 relaxation times was measured to be 2.0 s.

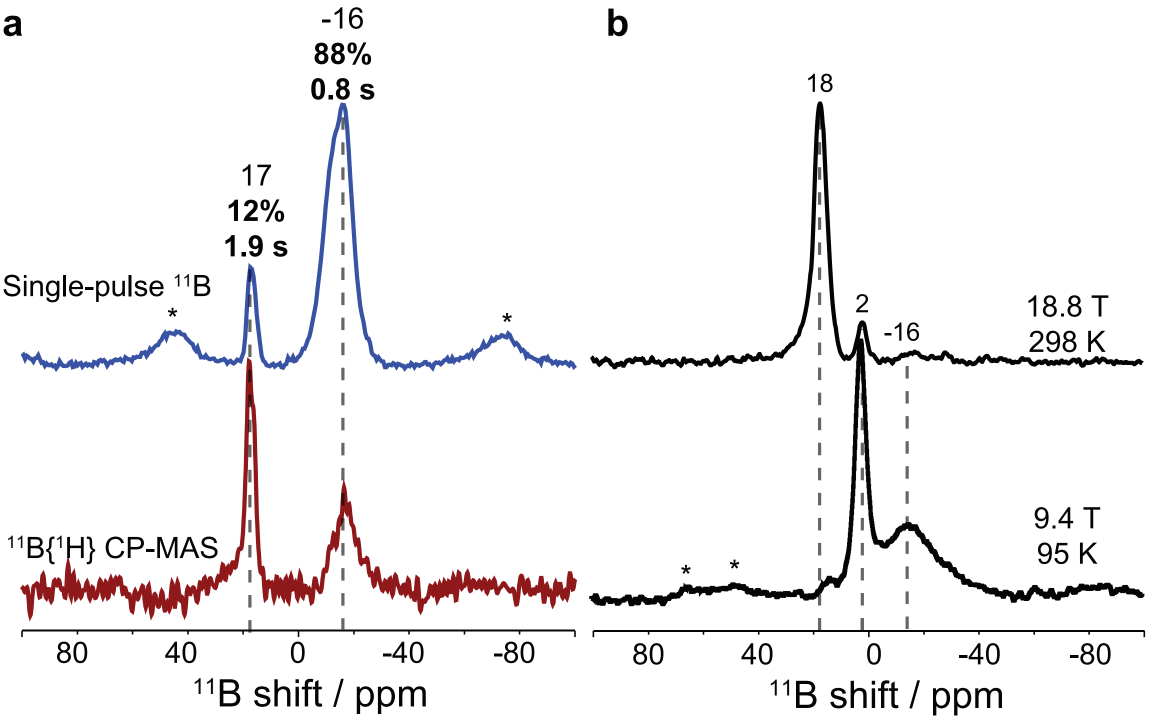

Fig. S20.

(**a**) Solid-state 1D single-pulse ^{11}B MAS NMR (top) and ^{11}B{^{1}H} CP-MAS (bottom) spectra of pre-annealed material **3**, showing that the majority of the sample is still composed of intact boron clusters; (**b**) ^{11}B{^{1}H} CP-MAS spectra of material **3** obtained at 18.8 T and 298 K (top) and 9.4 T and 95 K (bottom). At the lower temperature, paramagnetic relaxation effects are slowed, enabling better CP-MAS enhancement of the signals at 2 ppm and -16 ppm. However, the ^{11}B signal at 18 ppm is greatly broadened at the lower magnetic field strengths due to the field-dependent quadrupolar interactions of boron oxide[3] and reappearance of the peak at -16 ppm suggests that the associated boron atoms are in a highly symmetrical environment, as found for boron atoms in a cluster. The molecular B_{12} are then likely cross-linked and terminated by B-O-B and B-O-Ti bonds, consistent with their incorporation into the metal oxide matrix. Asterisks indicate spinning sidebands.

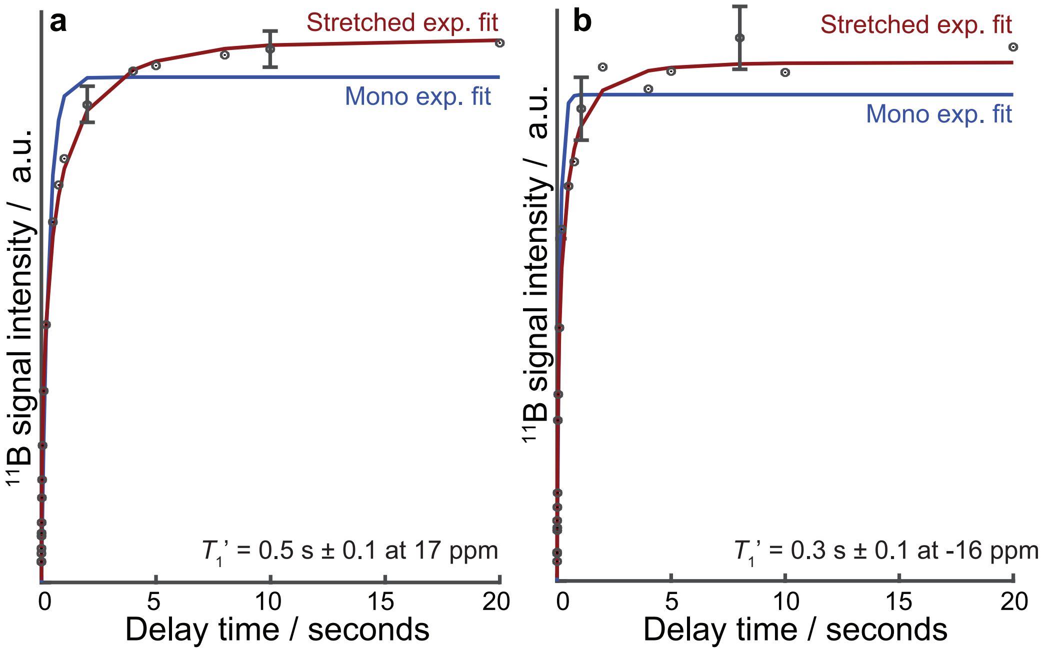

Fig. S21.

^{11}B relaxation analysis of material **3**. Measured ^{11}B saturation recovery signal intensities (black points) compared with stretched (red) and mono- (blue) exponential fitting functions for the ^{11}B signals at (**a**) 17 ppm and (**b**) -16 ppm. The measured ^{11}B signal intensities show good agreement with the stretched exponential function as expected for paramagnetic relaxation. The different ^{11}B species in material **3** are proximate to paramagnetic centers, as evidenced by ^{11}B spin-lattice (T_1) relaxation measurements, which are strongly influenced by the interactions of nuclear spins and unpaired electrons. Analysis of the ^{11}B T_1 relaxation behaviors shows that the different ^{11}B species in material **3** each exhibit a distribution of T_1 relaxation times. These distributions can be described by a stretched exponential function with a characteristic relaxation time T_1' and a stretched exponent of 0.5, which is typical of nuclear T_1 relaxation that arises from coupling to paramagnetic electron spins[4,5]. The measured ^{11}B T_1' relaxation times of material **3** are shown in Fig. 4a the respective ^{11}B signals. The species associated with the ^{11}B signal at -16 ppm exhibited the shortest T_1' (0.3 s), suggesting that they are closest to the paramagnetic centers in material **3**, which, on the basis of the EPR results, are likely localized on the molecular boron clusters.

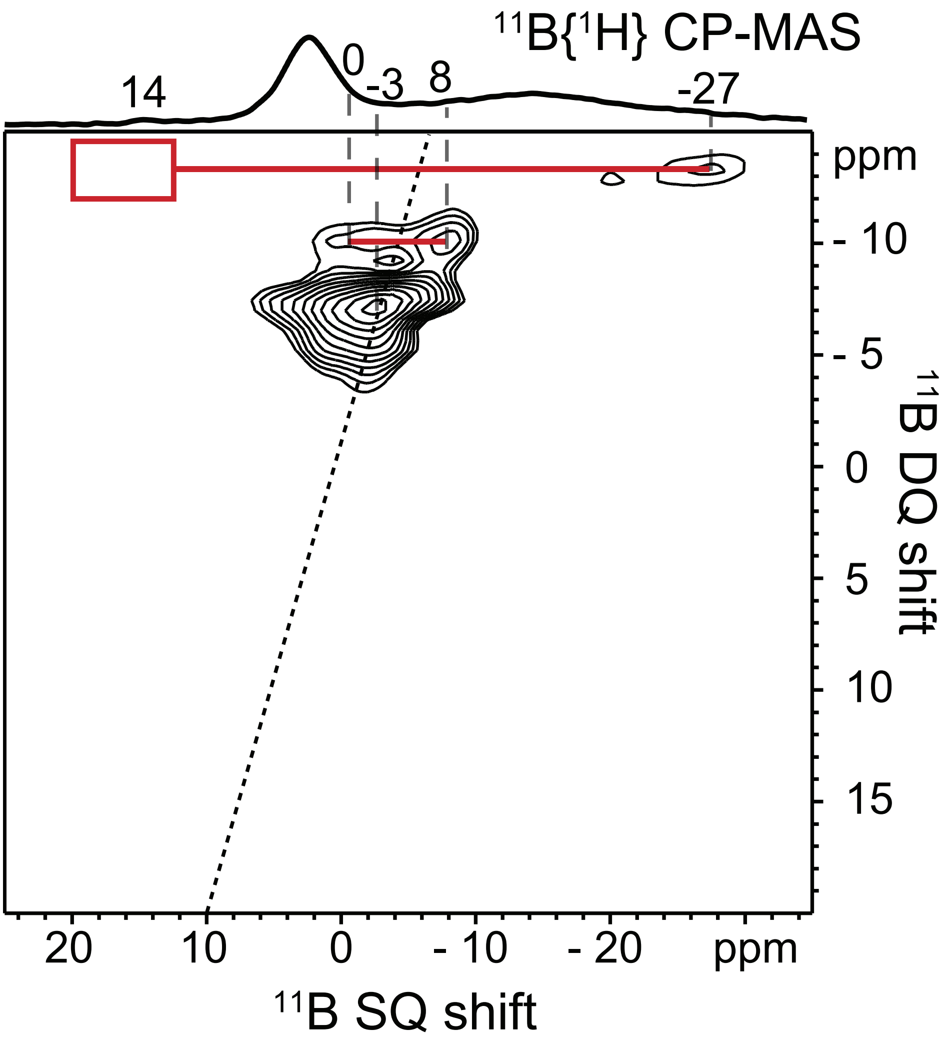

Fig. S22.

Two-dimensional dipolar-mediated (through-space) ^{11}B{^{11}B} correlation spectrum of material **3**, acquired at 9.4 T, 4.6 kHz MAS, and under low temperature conditions of 95 K to slow the nuclear spin relaxation kinetics and allow for more efficient dipolar recoupling. A 1D ^{11}B{^{1}H} CP-MAS spectrum acquired under the same conditions is shown above for comparison with the 2D spectrum. ^{11}B signals correlated across the diagonal arise from ^{11}B-^{11}B spin pairs which are dipole-dipole coupled through space (< 1 nm). The 2D spectrum shows signals at ^{11}B SQ shift positions of 0, -3, and -8 ppm, all of which arise from ^{11}B species in B_{12} clusters that are in close mutual proximities. Additionally, a signal at SQ: -27 ppm indicates that the B_{12} clusters are in close molecularly proximity (< 1 nm) with ^{11}B species in the boron oxide matrix (red line). The expected corresponding pair signal intensity around 14 ppm is not observed (red box), likely due to quadrupolar broadening of the ^{11}B signals from boron oxide at the lower magnetic field strengths (9.4 T) used to acquire the 2D dipolar-mediated NMR spectrum (see Fig. S20). Taken together, the 2D ^{11}B{^{11}B} NMR results establish the interconnectivities of intact B_{12} clusters, as well as the nanoscale proximities of B_{12} clusters with the oxide matrix.

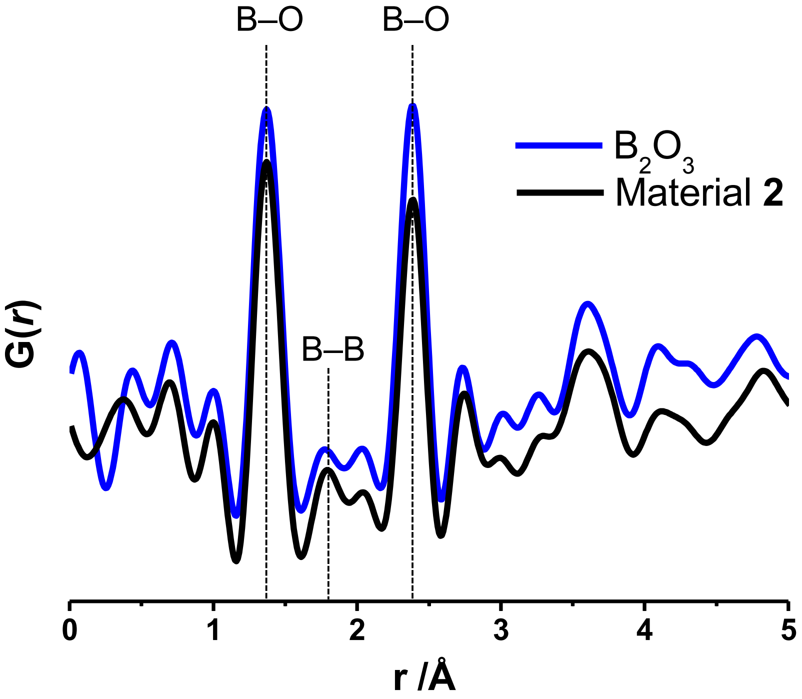

Fig. S23.

Pair distribution function (PDF) analysis of material **2** and B_2O_3 control. Although reduced in intensity, the peak corresponding to B-B bound atoms (at ~ 1.87 Å) can be observed for **2**.

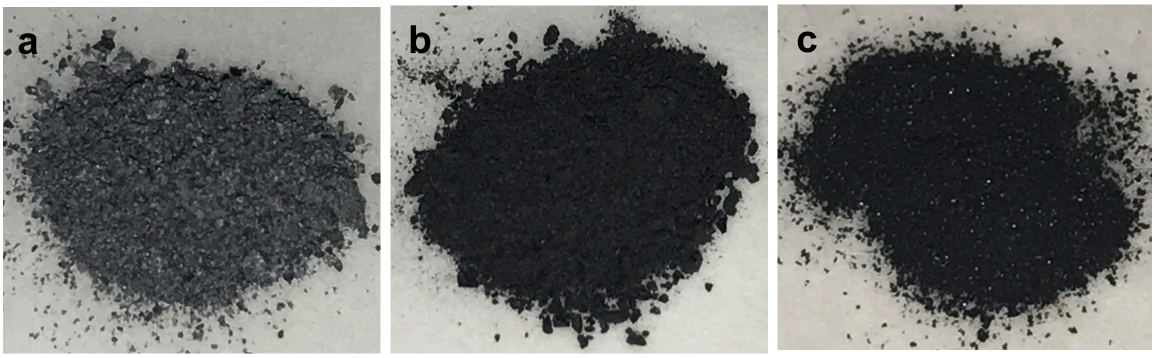

Fig. S24.

A control reaction was performed where 10 % graphite (by mass) was added to $Ti(O^iPr)_4$, hydrolyzed and annealed under the same conditions for materials **2** and **3** to form a composite graphitic TiO_2 material (image **a**). The combustion analysis confirmed the composite graphitic TiO_2 contained ~5 % carbon. The optical images show that this material, despite its similar carbon content, was a grey color rather than the intense black of materials **2** (image **b**) and **3** (image **c**) suggesting that the carbon content alone in the material is insufficient to produce the observed color.

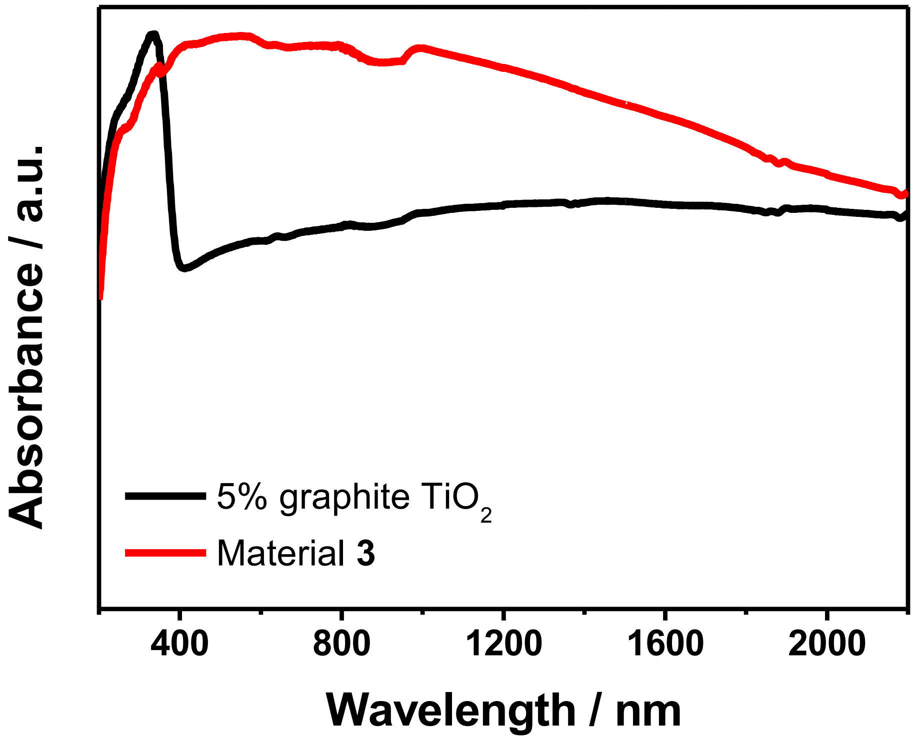

Fig. S25.

Diffuse reflectance UV-Vis spectroscopy of a composite graphitic TiO_2 (Fig. S24a) and material **3,** showing different light absorption properties. This experiment clearly suggests that the carbon content alone is insufficient to produce the strong light absorption properties.

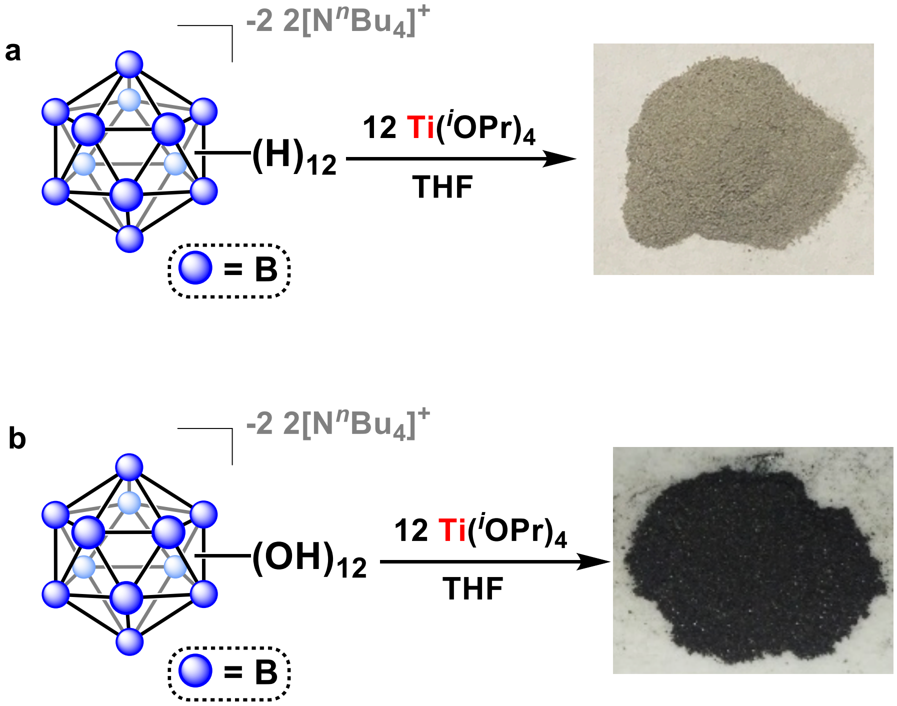

Fig. S26.

(**a**) A control reaction was performed where $[N^nBu_4]_2[B_{12}H_{12}]$ was added to $Ti(O^iPr)_4$, hydrolyzed and annealed under the same conditions for materials **3** to form a non cross-linked TiO_2 material. (**b**) A synthetic route to produce material **3**. These results further corroborate that cross-linking B_{12}-based clusters is indeed important for the observed black color.

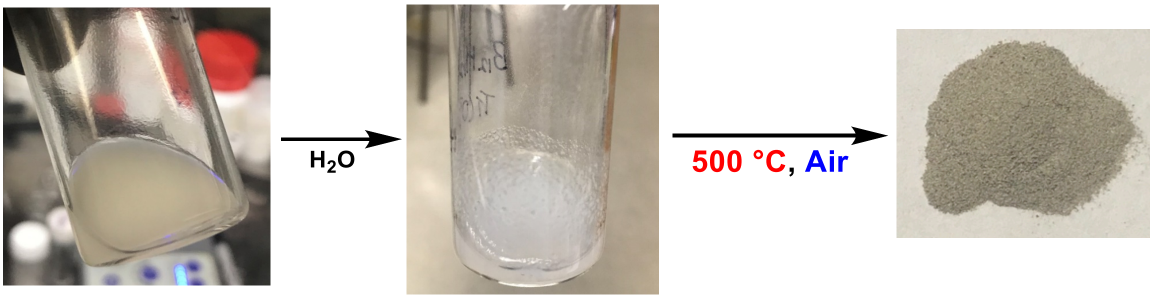

Fig. S27.

A reaction of $[N^nBu_4]_2[B_{12}H_{12}]$ with $Ti(O^iPr)_4$ in THF. It produces a cloudy white solution, which is subsequently hydrolyzed to form a white slurry. After calcining at 120 °C, the solid is annealed at 500 °C in air to produce a non cross-linked TiO_2 material.

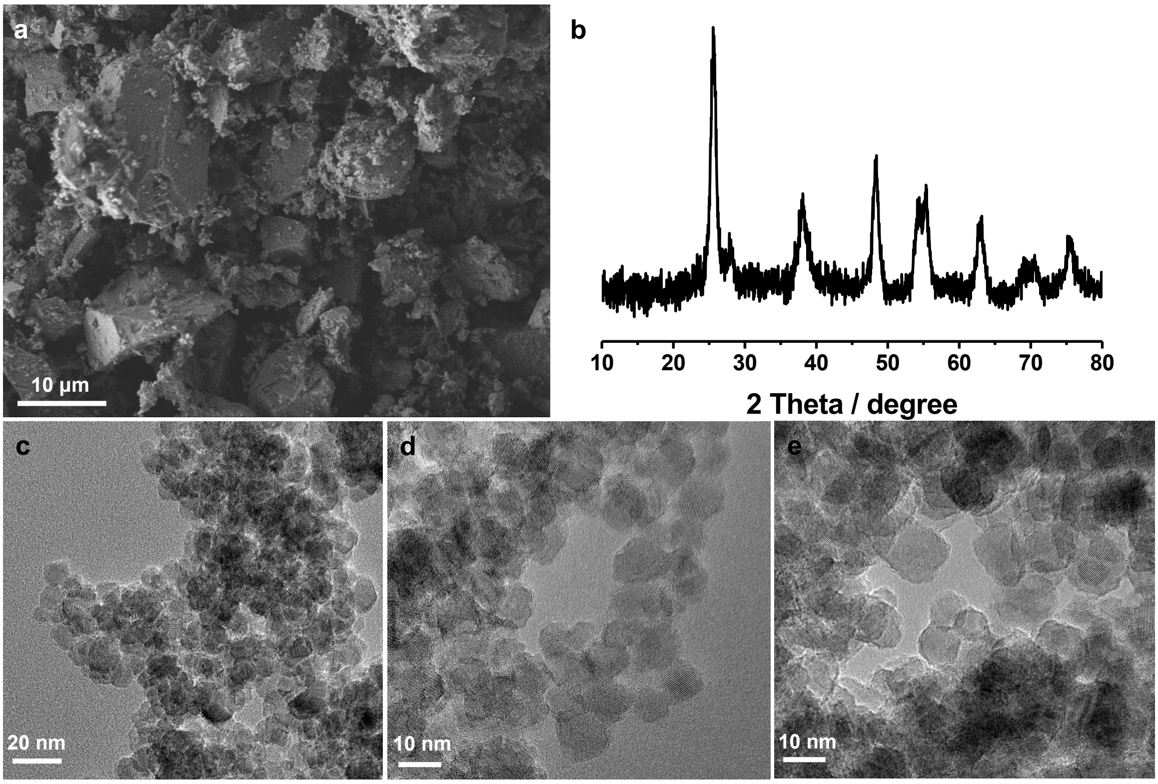

Fig. S28.

(**a**) SEM image; (**b**) PXRD pattern; (**c-e**) TEM images of a non cross-linked TiO_2 (see Fig S27). Based on the structural characterizations, we confirmed the resulting compound did not have a cross-linked morphology.

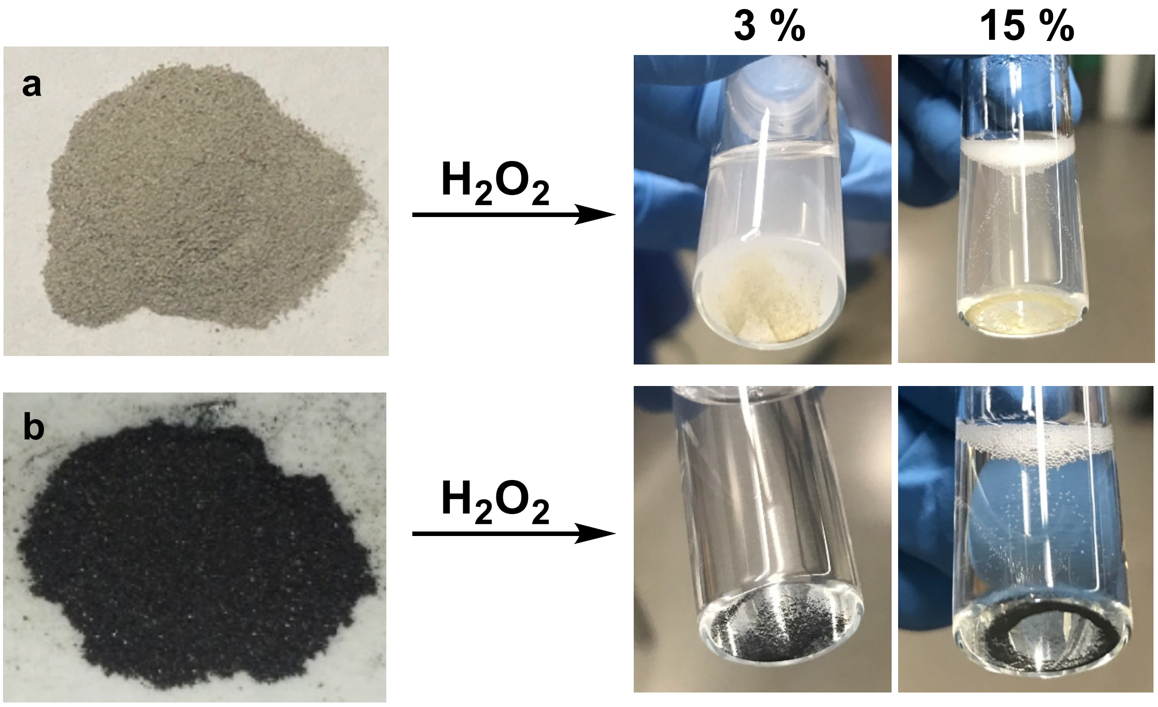

Fig. S29.

Chemical stability test of (**a**) a non cross-linked TiO_2 and (**b**) material **3** in 3 % and 15 % H_2O_2. While **3** resisted prolonged exposure to both 3 % and 15 % H_2O_2, a non cross-linked TiO_2 lost its color upon the exposure to H_2O_2. Given the light color and weak chemical stability of the non cross-linked TiO_2, cross-linking B_{12}-based clusters to TiO_2 is indeed important for the observed intense color and robustness.

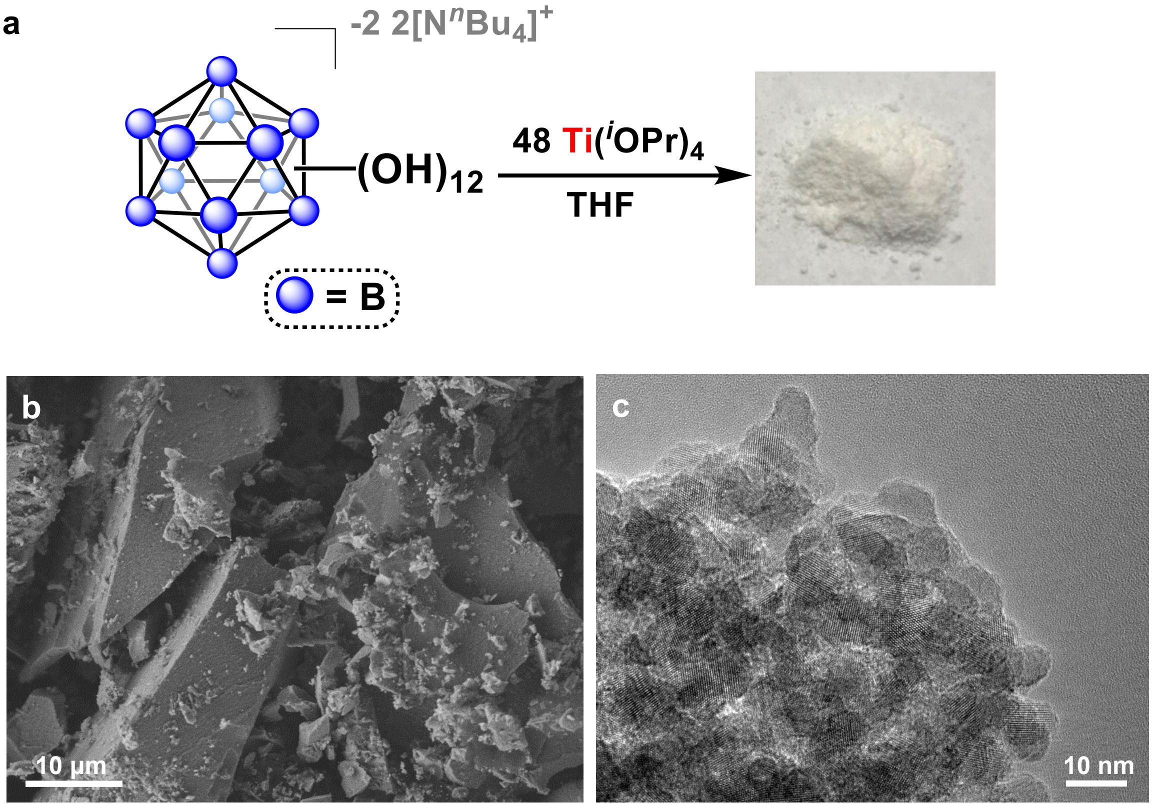

Fig. S30.

(a) A control reaction was performed where [N^{n}Bu$_4$]$_2$[**1**] was added to 48 equivalent of Ti(O^{i}Pr)$_4$, which is four times more titanium precursors than material **3**. It was then hydrolyzed and annealed under the same conditions for materials **3** and the resulting compound was a white powder as the excess TiO$_2$ diluted the amount of the cross-linkers. (**b**) SEM image; (**c**) TEM image of the resulting compound, showing the cross-linked morphology to some extent.

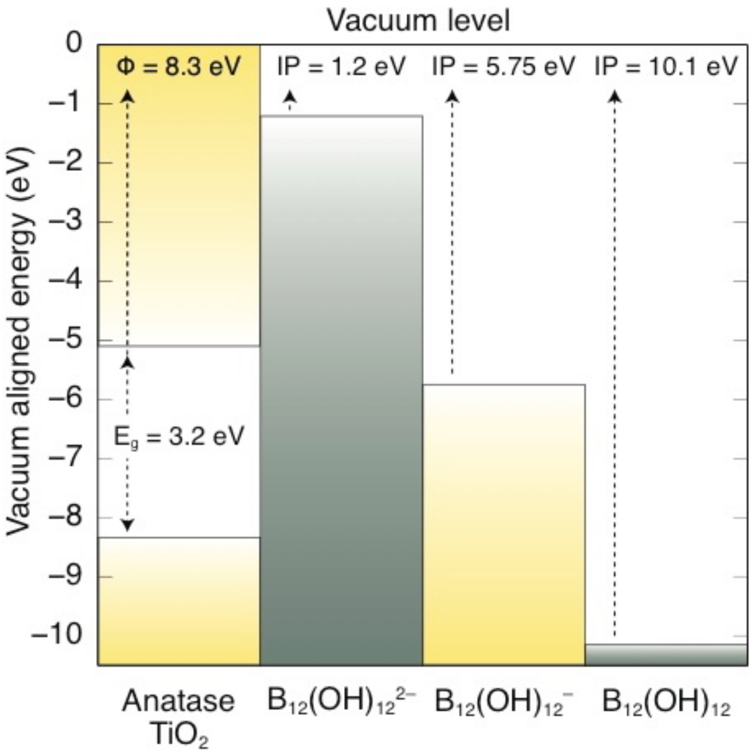

Fig. S31.

Electron energy alignments of anatase TiO_2, and B_{12}-based clusters in different oxidation states. Anatase TiO_2 has a band gap of 3.2 eV and a work function of 8.3 eV (*Nature Mater.* **2013**, *12*, 798). The $[B_{12}(OH)_{12}]^{2-}$ species has an extremely low ionization potential (IP = 1.2 eV), indicating that the valence electrons are loosely bound, or highly reducing. Upon single electron oxidation, $[B_{12}(OH)_{12}]^{-}$ features a HOMO located midgap to TiO_2, resulting in an extremely narrow charge transfer excitation (0.65 eV) which would give rise to a black material and absorption in the near IR to some extent. The charge neutral compound, $B_{12}(OH)_{12}$ is stable, with tightly bound valence electrons as evidenced by the ionization potential= 10.1 eV. In this case, the zero charge clusters would be expected to deplete TiO_2 of electron density from the oxygen valence of TiO_2, making an electron deficient O-Ti site. Based on the similar light absorption properties observed in material **2** and **3**, a variety of charge transfer transitions would likely give rise to the broad absorbance: intervalence charge transfers between clusters in different valence states, and charge transfers between the clusters and the boron/titanium oxides, as well as some absorbance from trapped carbon.

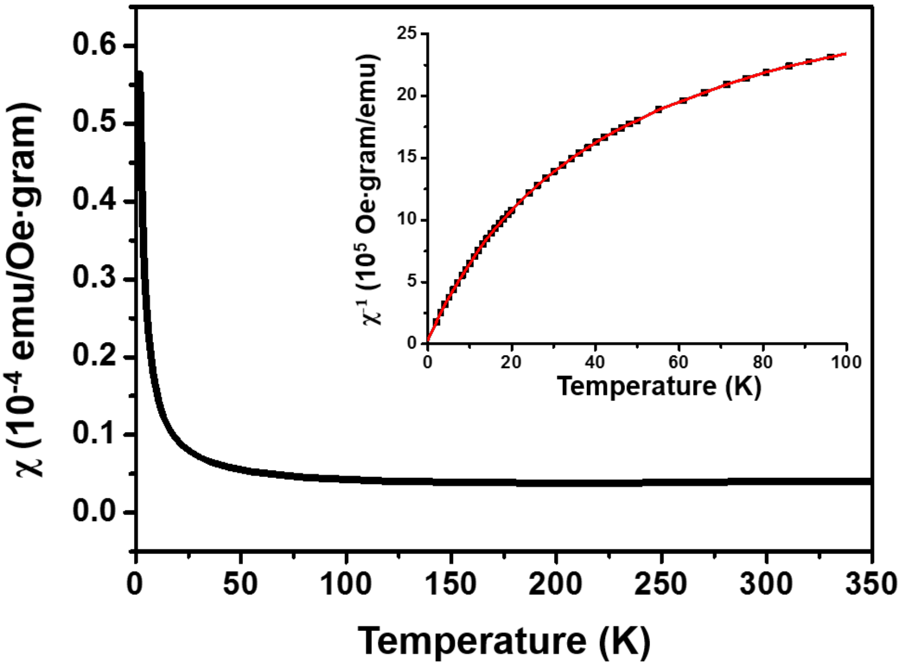

Fig. S32.

Plot of the SQUID magnetometric data obtained for material **3**, along with a plot of inverse of the magnetic susceptibility against temperature (inset).

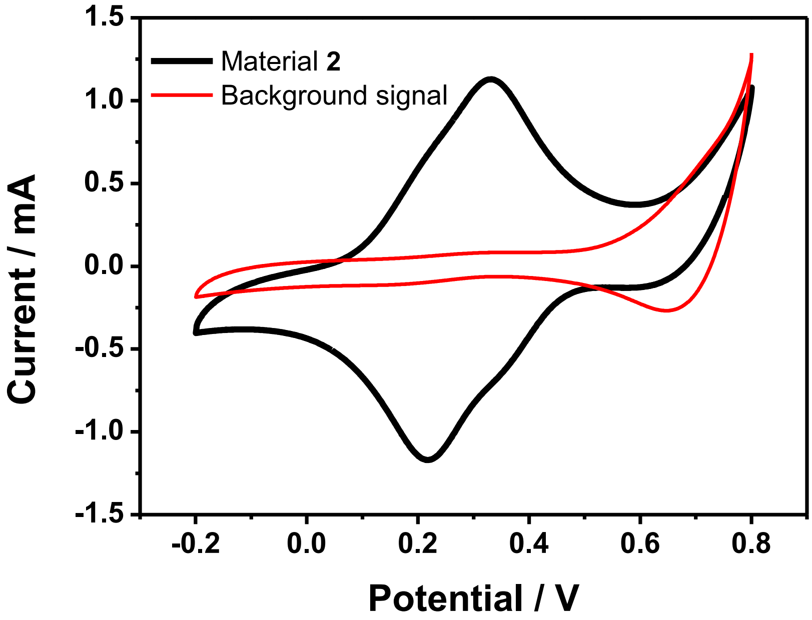

Fig. S33.

CV curves of material **2** for the ferri/ferrocyanide redox couple (black) and the supporting electrolyte only (red). Material **2** is electrochemically active by itself, but the peak-to-peak separation (116 mV) is larger than material **3** (89 mV). The oxidation wave at 0.8 V is consistent with the previously observed redox feature of unfunctionalized $[B_{12}(OH)_{12}]^{2-}$ cluster undergoing single electron oxidation to a radical species $[B_{12}(OH)_{12}]^{1-}$ 6.

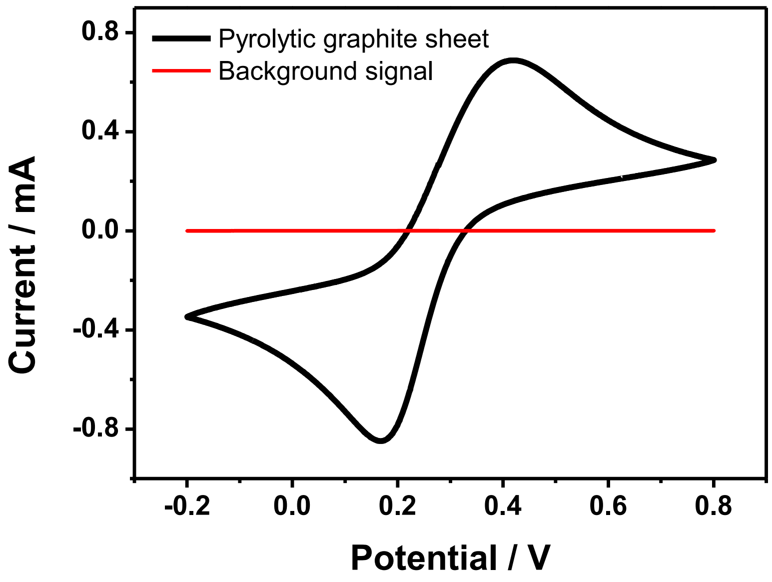

Fig. S34.

CV curves of pyrolytic graphite sheet electrodes for the ferri/ferrocyanide redox couple (black) and the supporting electrolyte only (red). The peak-to-peak separation of the pyrolytic graphite sheet (253 mV) is much larger than material **3** (89 mV).

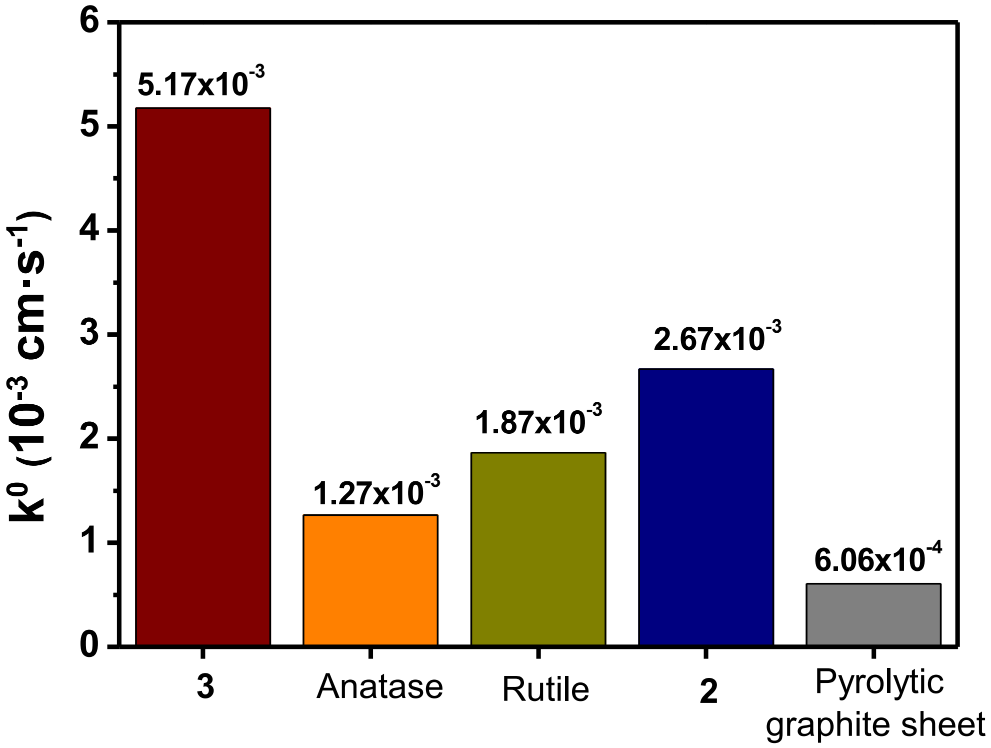

Fig. S35.

Bar chart showing the electron transfer rate constants for material **3**, anatase, rutile TiO_2, material **2**, and pyrolytic graphite sheet. Commercially available TiO_2 consists of spherical nanoparticles with ~100 nm in diameter (see Fig. S36b). In this case, charge transfer is limited to the surface of the material only. On the other hand, material **3** contains nanocrystalline TiO_2 (<10 nm) cross-linked with B_{12}-based clusters, while the bulk material itself remains micron-sized. This features a unique structure, creating internal mesopores that can act as electrolyte solution reservoirs. This explains the faster electron transfer kinetics at the material **3** electrodes. Charge transfer occurs at the electrode/electrolyte interface, meaning that a material with higher surface area will possess more active sites where the charge transfer may occur. Material **3** has high specific surface area, leaving behind 3 nm mesopores that provide more room for charge transfer to occur (see Fig. S37). Additionally, defect sites on the structure such as step edges shown in Figure S29a are responsible for the favorable electrochemical activity[7,8]. The improved electrical conductivity of material **3** than commercial TiO_2 (see Fig. S43d) and material **2** (see Fig. S41) also results in the faster charge transfer kinetics [9].

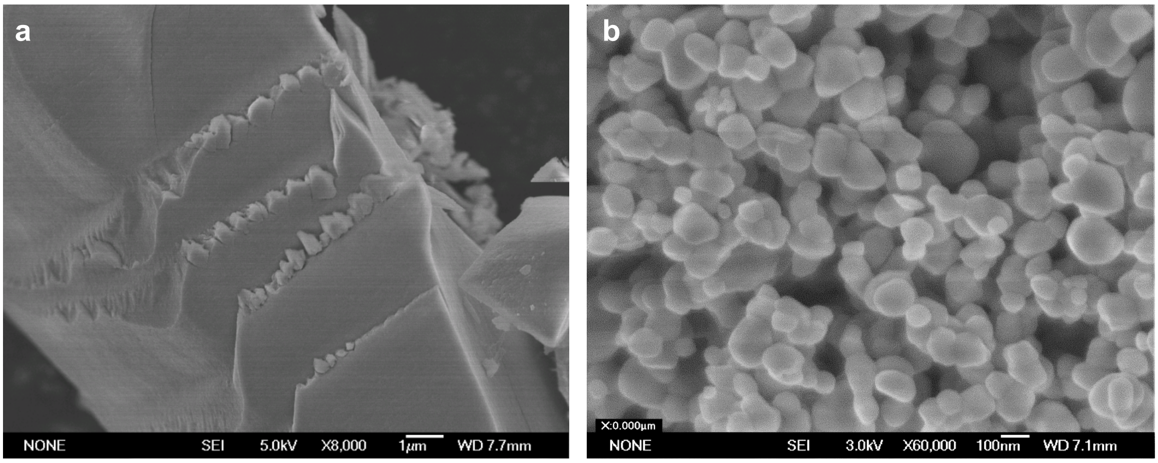

Fig. S36.

SEM images of (**a**) material **3**; (**b**) anatase TiO_2.

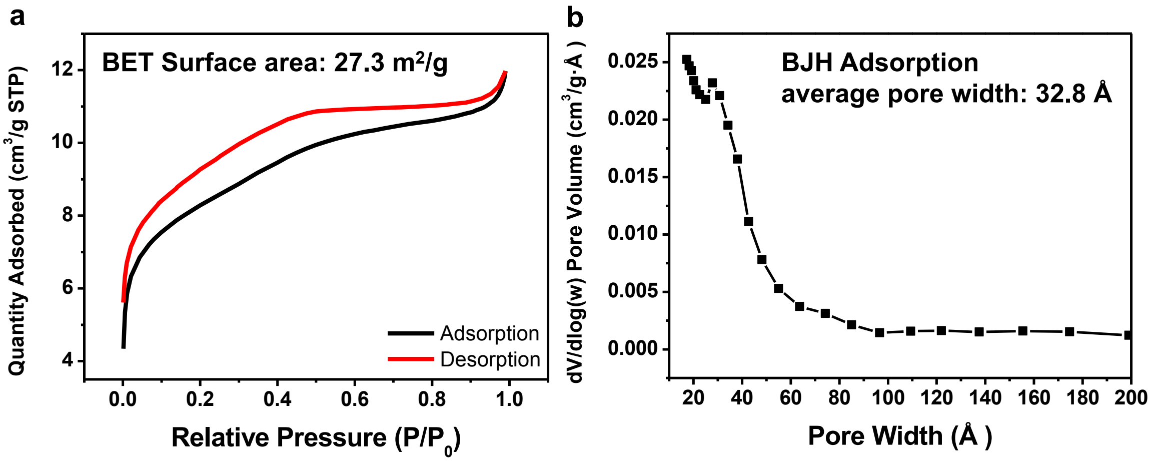

Fig. S37.

(**a**) Low pressure N_2 adsorption isotherms of material **3**. The Brunauer-Emmett-Teller (BET) surface area is 27.3 m^2/g; (**b**) Calculated pore size distribution of material **3** using the Barret-Joyner-Halenda (BJH) equation.

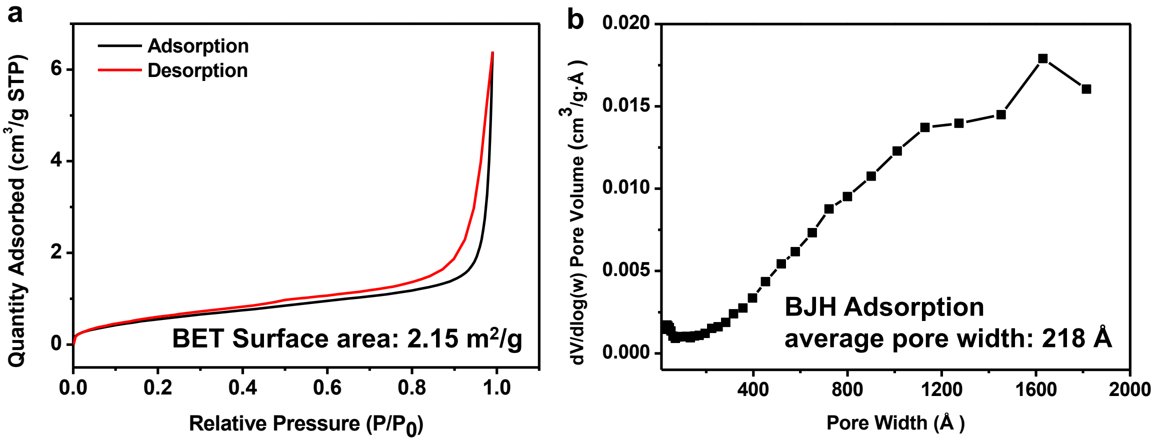

Fig. S38.

(**a**) Low pressure N_2 adsorption isotherms of material **2**. The Brunauer-Emmett-Teller (BET) surface area is 2.15 m^2/g; (**b**) Calculated pore size distribution of material **2** using the Barret-Joyner-Halenda (BJH) equation.

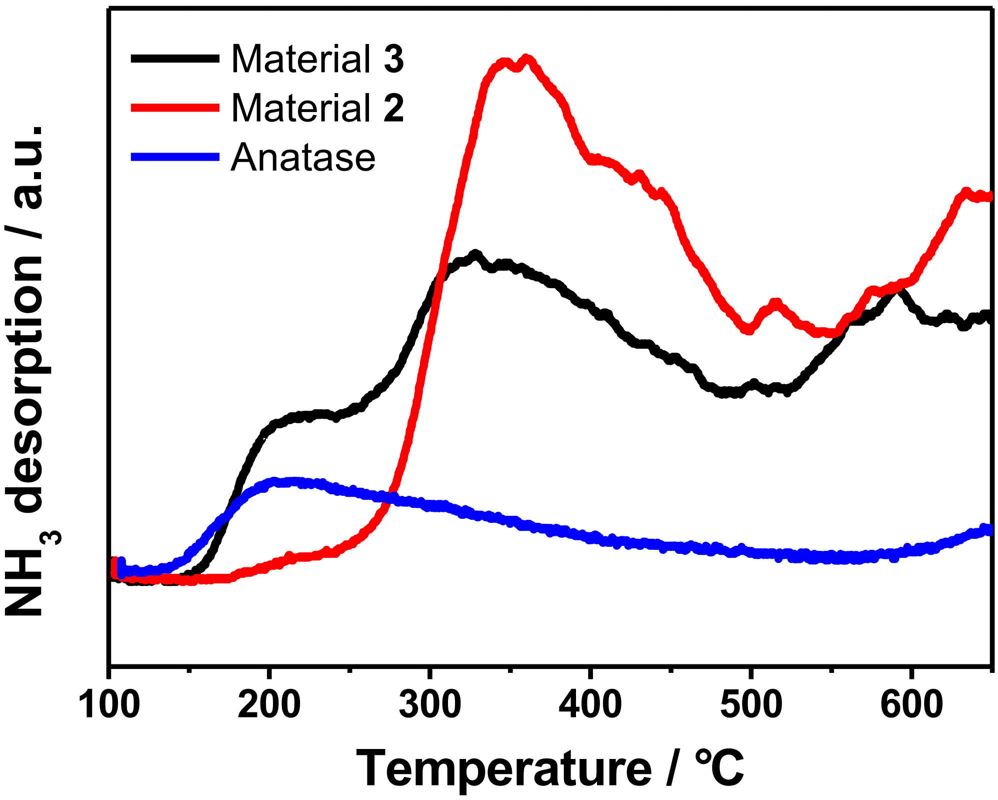

Fig. S39.

Temperature-programmed desorption (TPD) of ammonia from the surface of material **2**, **3** and anatase. The desorption peak at lower temperature regime (< 300℃) is assigned to weak acidic sites, and the peak at higher temperatures (>300℃) is attributed to the strong acidic sites. On the basis of desorption temperatures of ammonia, material **2** predominantly possesses strong acidic sites, while **3** possesses both weak and strong acidic sites. It has been previously reported that desorption of ammonia from TiO_2 surface occurs at 222 ℃ when the ammonia was absorbed at 100 ℃ [10]. These results are consistent with the desorption data at the lower temperature region in **3** and anatase. Overall, **3** exhibits hybrid surface properties, which arise from both material **2** and TiO_2.

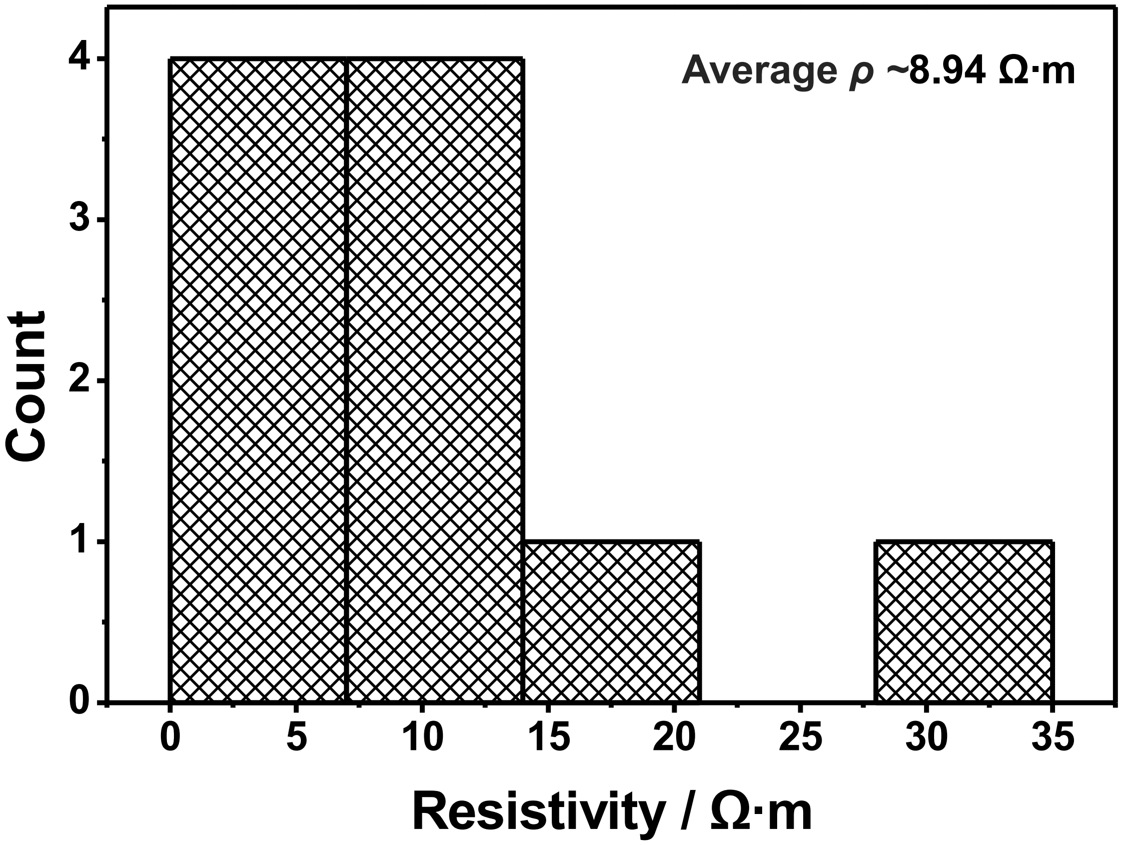

$R_S = R/(L/W) = R/(3.0) = 5.94\text{x}10^{7}\ \Omega/3.0 = \mathbf{2.0x10^{7}\ \Omega}$

$\rho = R_S \cdot t = 2.0 \text{ x } 10^{7} \text{ x } 398.6 \text{ nm} = \mathbf{8.0\ \Omega \cdot m}$

σ (Conductivity)= 1/ρ= $\mathbf{0.13\ \Omega^{-1} \cdot m^{-1}}$

Fig. S40.

Plot of the statistics of ten different devices fabricated from **3** as a function of resistivity (ρ).

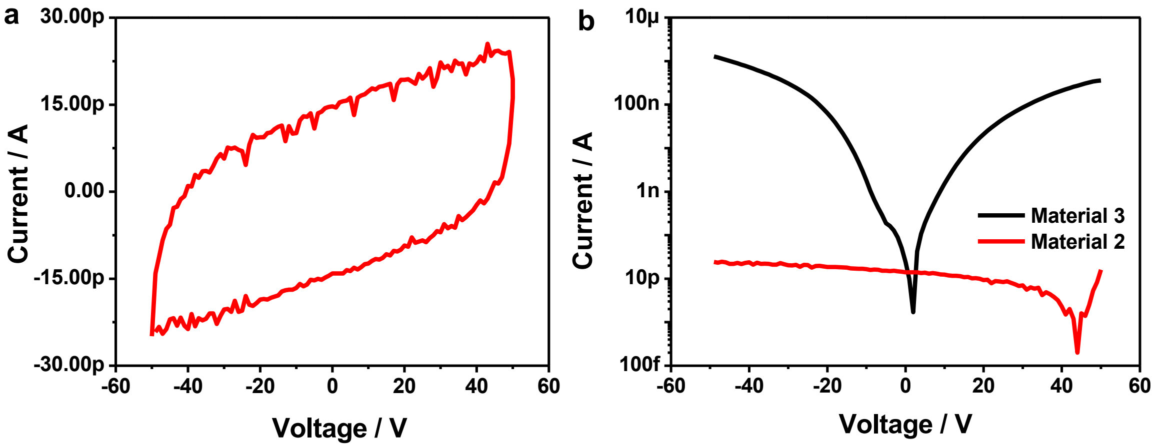

Fig. S41.

(**a**) Linear-scale plot of the I-V curve of material **2**. The measured current is close to the lower limit of the system, indicating a low electrical conductivity of **2**; (**b**) Log-scale I-V curves of Material **2** and **3**, showing the current response is much higher in **3**. The calculated conductivity of **2** and **3** is 1.1 x 10^{-5} Ω^{-1}•m^{-1} and 4.2 x 10^{-2} Ω^{-1}•m^{-1}, respectively. This indicates the hybrid molecular boron oxide material (material **2**) is not very conductive, however, when metal oxides are incorporated, its conductivity is much improved (material **3**). The possible explanation for the conductivity of material **3** can be a result of the creation of charge transfer between the hybrid molecular boron oxide material and metal oxides[11]. In addition, increasing carrier concentration by cross-linking B_{12}-based clusters to TiO_2 can be another reason for the improved conductivity[12].

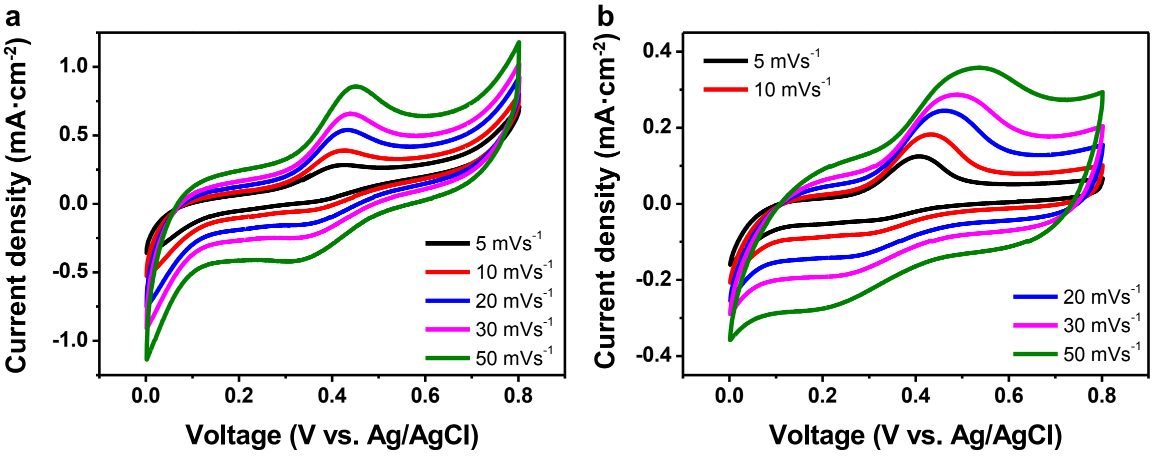

Fig. S42.

Cyclic voltammograms (CV) of (**a**) material **3** and (**b**) Commercial TiO_2 at different scan rates.

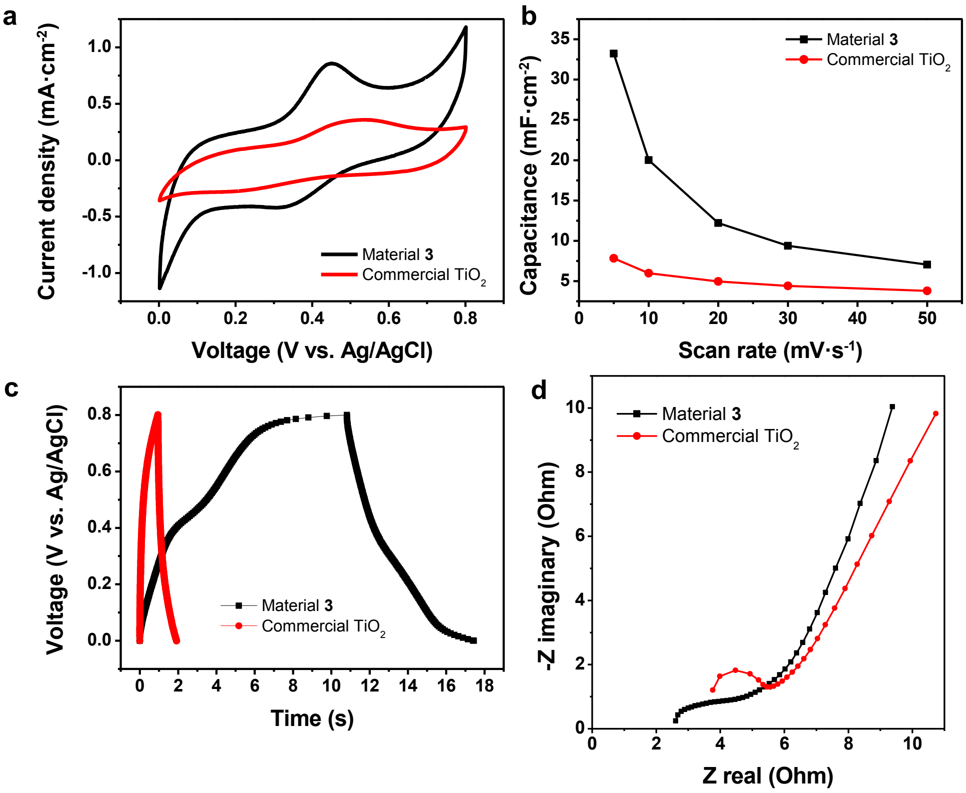

Fig. S43.

Three-electrode electrochemical cell measurements of material **3** and commercial TiO_2. (**a**) CV curves at a scan rate of 50 mV/s; (**b**) Areal capacitance as a function of scan rates; (**c**) Galvanostatic charge/discharge curves; (**d**) Nyquist plots. Compared to commercial TiO_2, material **3** has larger integrated area along with the higher current response, and its calculated areal capacitance of electrodes as a function of scan rate is much larger than commercial TiO_2 (Fig. S43a and b). Moreover, galvanostatic charge/discharge curve of **3** is significantly prolonged over the pristine TiO_2 (Fig. S43c). Electrochemical impedance spectroscopy (EIS) is further studied to evaluate the capacitive characteristics of electrode materials. In the Nyquist plots, the intercept at the real axis in the higher frequency region represents the equivalent series resistance (ESR), which arises from the electric resistance of the electrode material and the interface resistance. Material **3** reveals a lower ESR than that of the commercial TiO_2, implying an improved electrical conductivity in **3** (Fig. S43d). In addition, the straight line of **3** in the lower frequency area is steeper than that of TiO_2, representing a lower diffusion resistance and an ideal polarizable capacitance. Overall, the results show the electrochemical performance of **3** is substantially improved than TiO_2 as an electrode for supercapacitors. The areal capacitance of the materials (C_A) was calculated using the formula

$$C_A = \frac{1}{vA\,(V_f - V_i)} \int_{V_i}^{V_f} i(V)dV$$

, where $\boldsymbol{i}$ is the current response (mA), $\boldsymbol{V_f - V_i}$ is the potential window (V), $\boldsymbol{v}$ is the scan rate (V/s), and A is the footprint area of the electrode in three-electrode measurements.

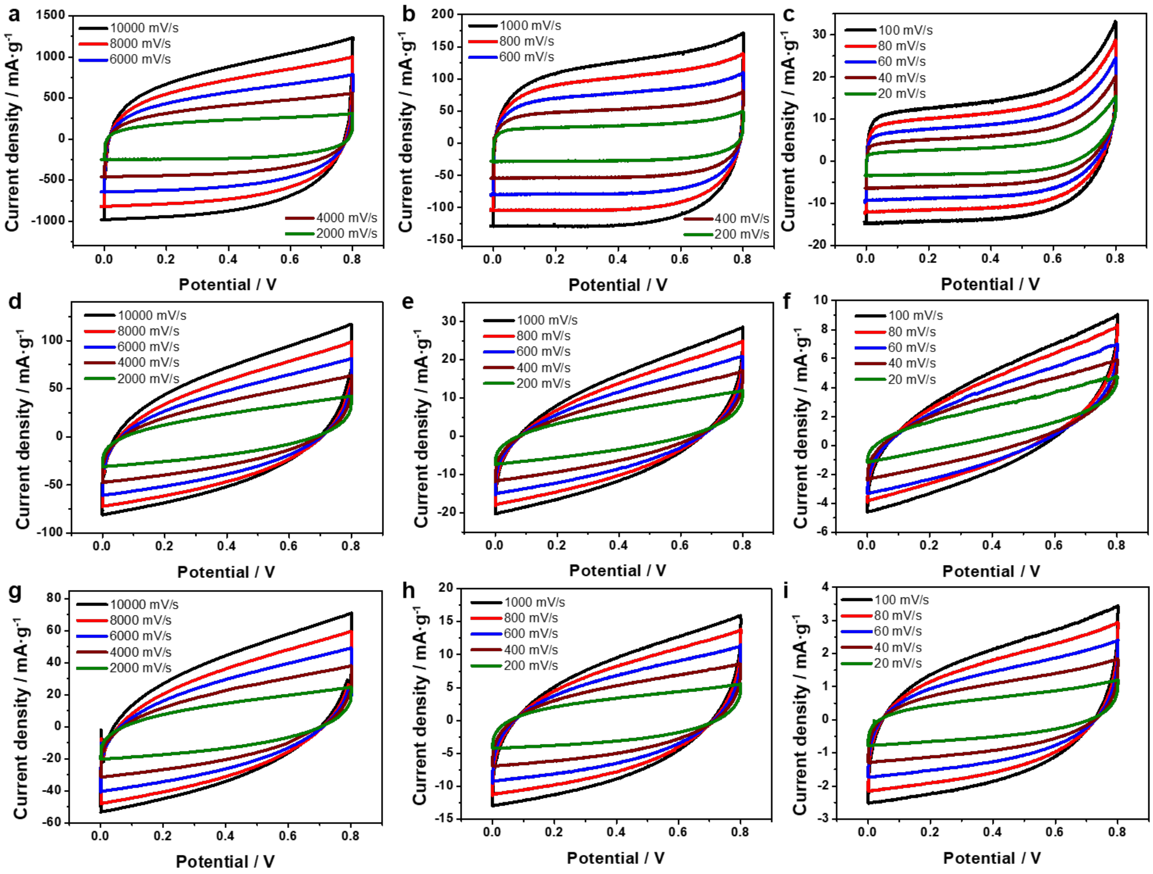

Fig. S44.

Cyclic voltammograms (CV) of (**a-c**) material **3**, (**d-f**) anatase, and (**g-i**) rutile TiO_2 at scan rates from 20 mV/s to 10,000 mV/s. **3** exhibits much enhanced performances at each scan rate, featuring much larger integrated area along with the higher current responses than both forms of TiO_2. Importantly, material **3** shows more rectangular CV profiles even when tested at an ultrafast scan rate of 10,000 mV/s, indicating its excellent rate capability.

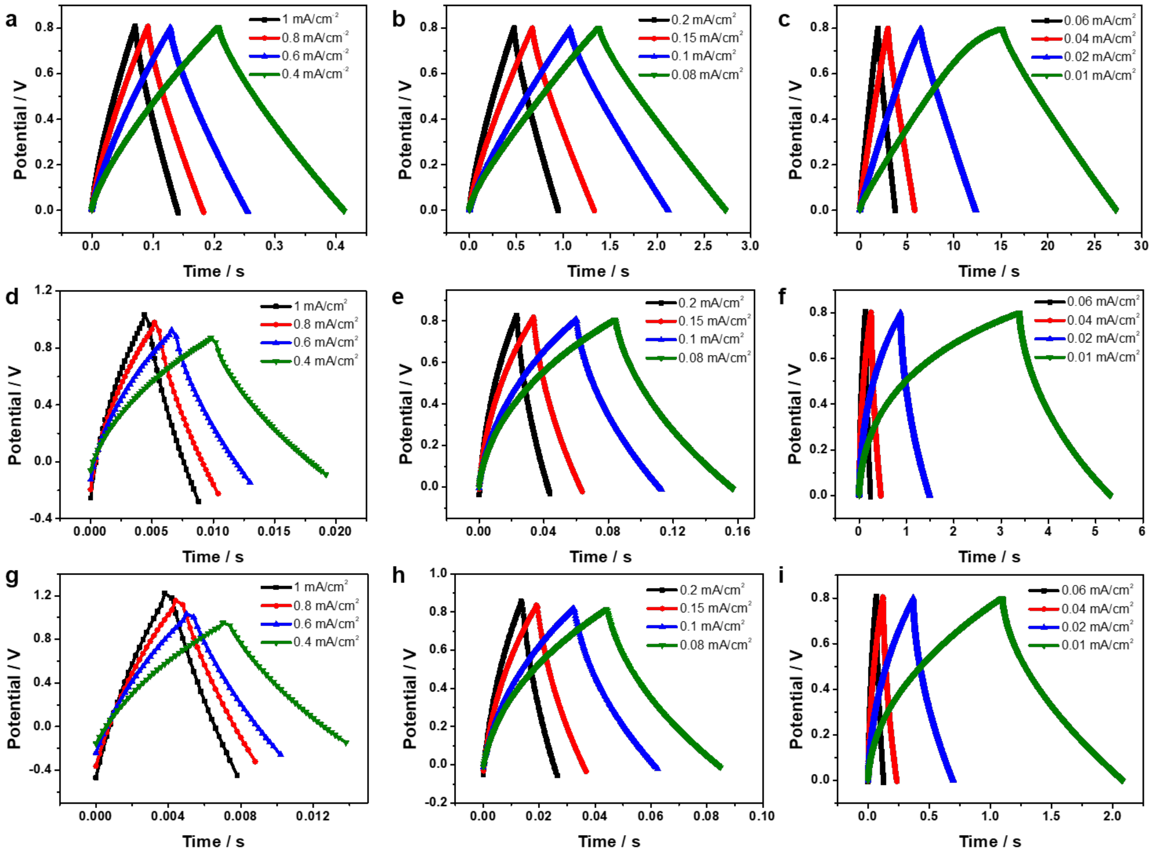

Fig. S45.

Galvanostatic cycling charge/discharge profiles of (**a-c**) material **3**, (**d-f**) anatase, and (**g-i**) rutile TiO_2 at different current densities. At each current density, the charge/discharge curves of **3** are dramatically prolonged over both forms of TiO_2.

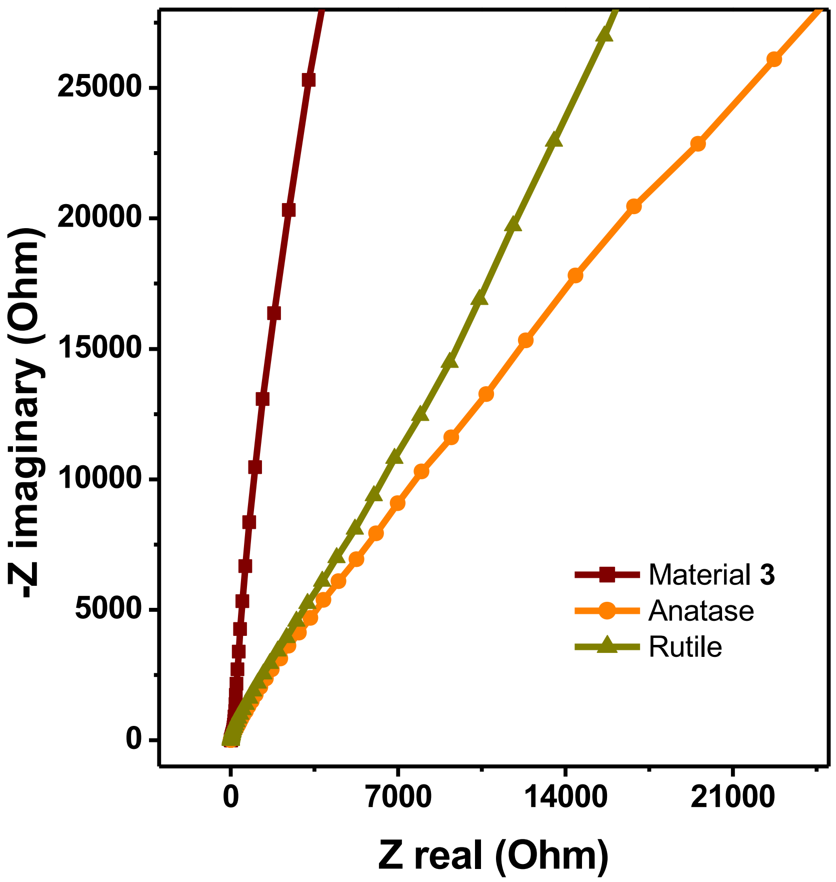

Fig. S46.

Nyquist plots of material **3**, anatase, and rutile TiO_2, showing the straight line of **3** in the lower frequency area is much steeper than that of both forms of TiO_2. It represents a lower diffusion resistance and an ideal polarizable capacitance in **3**.

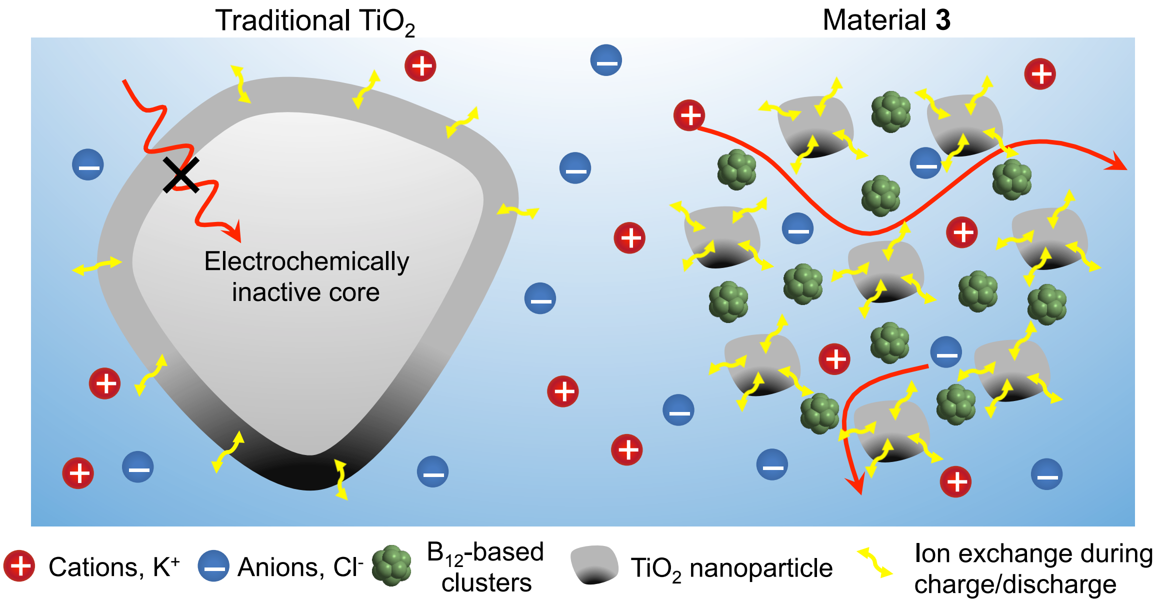

Fig. S47.

A schematic illustration of electrochemical processes in TiO_2 vs. material **3**. Material **3** enables the full utilization of TiO_2 surfaces whereas in the traditional TiO_2 only the external surfaces are available for charge storage.

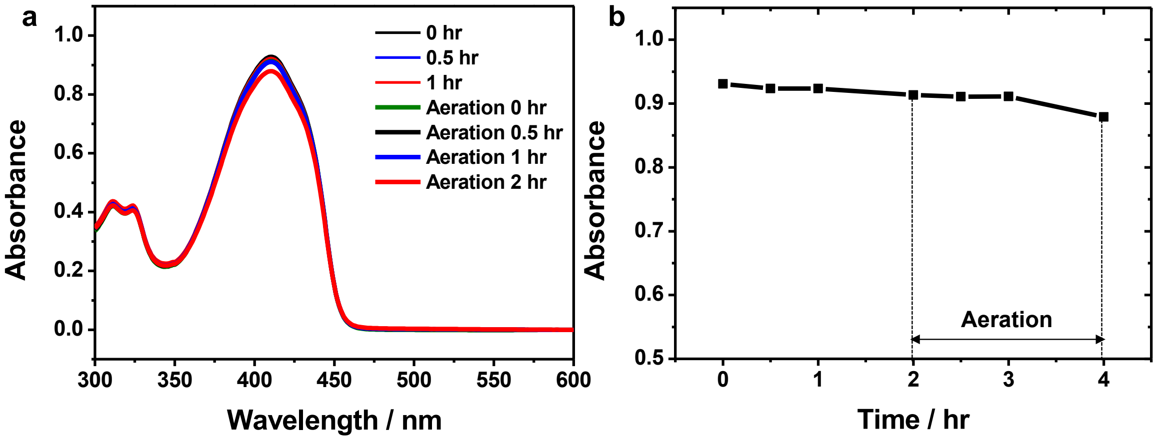

Fig. S48.

(**a**) Control UV-Vis spectrum depicting the progression of the consumption of DPBF in the presence of **2** and irradiation with red (~630 nm) LED lights. DPBF is a sensitive probe for ROS, and a decrease in its absorbance at 410 nm is indicative of the production of ROS. Even after aeration of the reaction mixture, decomposition of DPBF was barely observed, indicating the absence of photocatalytic activity of **2**; **(b)** a chart showing the rate of consumption of DPBF.

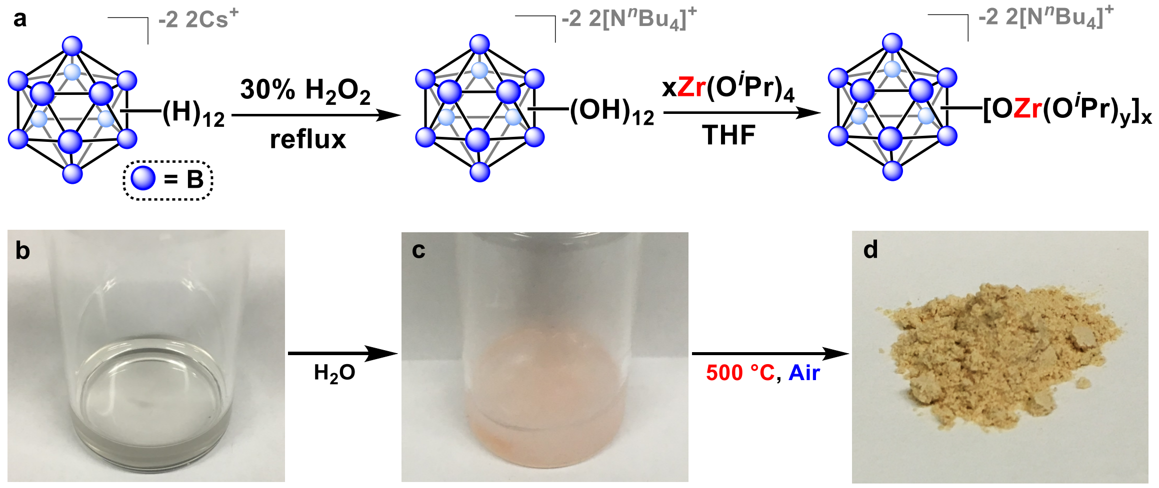

Fig. S49.

(**a**) Synthetic route towards the synthesis of material **4** utilizing the robust polyhedral boron cluster $[N^nBu_4]_2$[**1**] as a key precursor. A reaction of $[N^nBu_4]_2$[**1**] with $Zr(O^iPr)_4{\bullet}^iPrOH$ in THF produces a clear solution (**b**), which is subsequently hydrolyzed to form a pink gel (**c**). After calcining at 120 °C, the now brown solid is annealed at 500 °C in air to produce material **4** as a light brown solid (**d**).

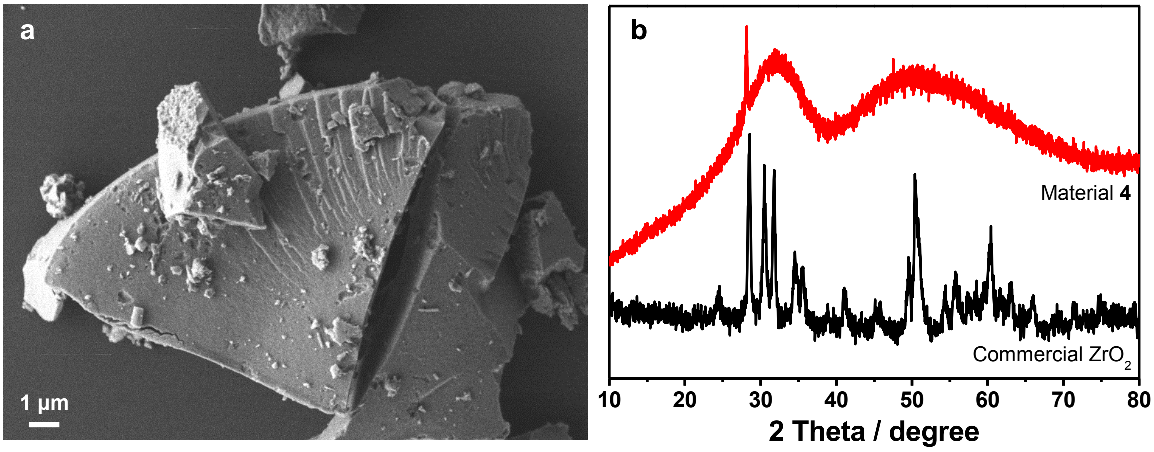

Fig. S50.

(**a**) SEM image of material **4**; (**b**) PXRD pattern of material **4**, with ZrO_2 control.

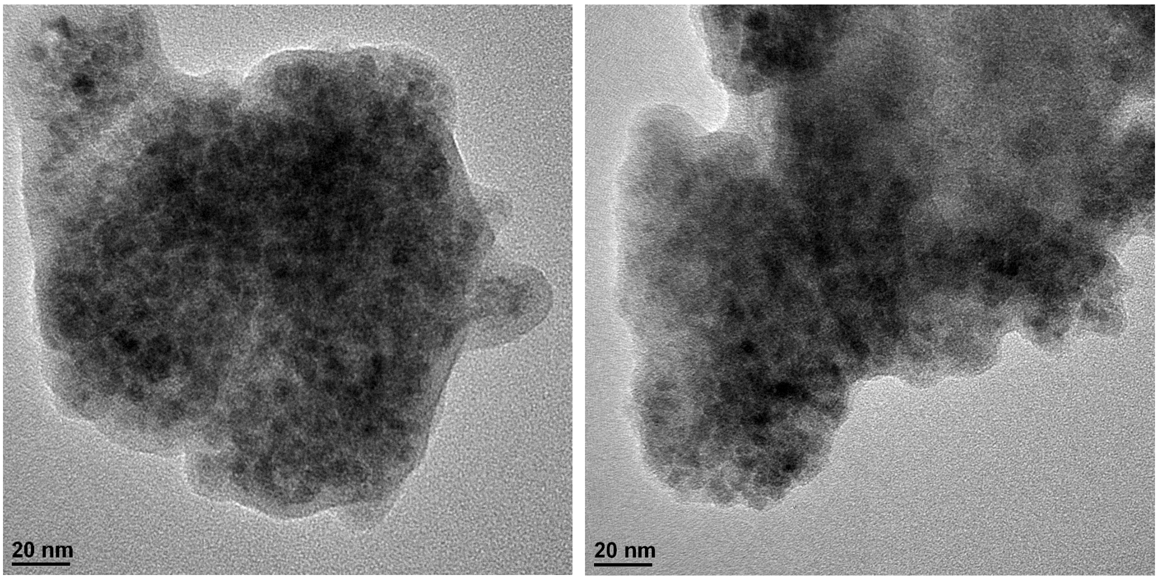

Fig. S51.

High-resolution TEM images of material **4**, showing the similar cross-linked morphology as the previous case of material **3**.

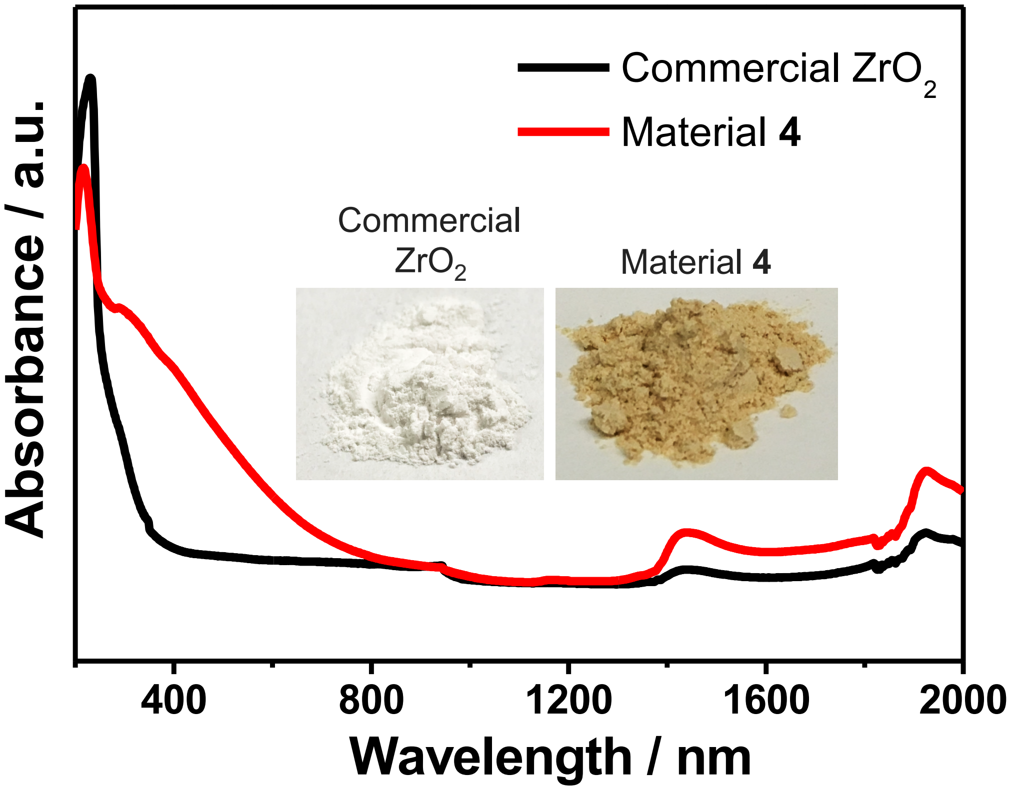

Fig. S52.

Diffuse-reflectance UV-Vis data for material **4**, plotted with data for ZrO_2 to highlight the difference in light absorption properties of the materials.

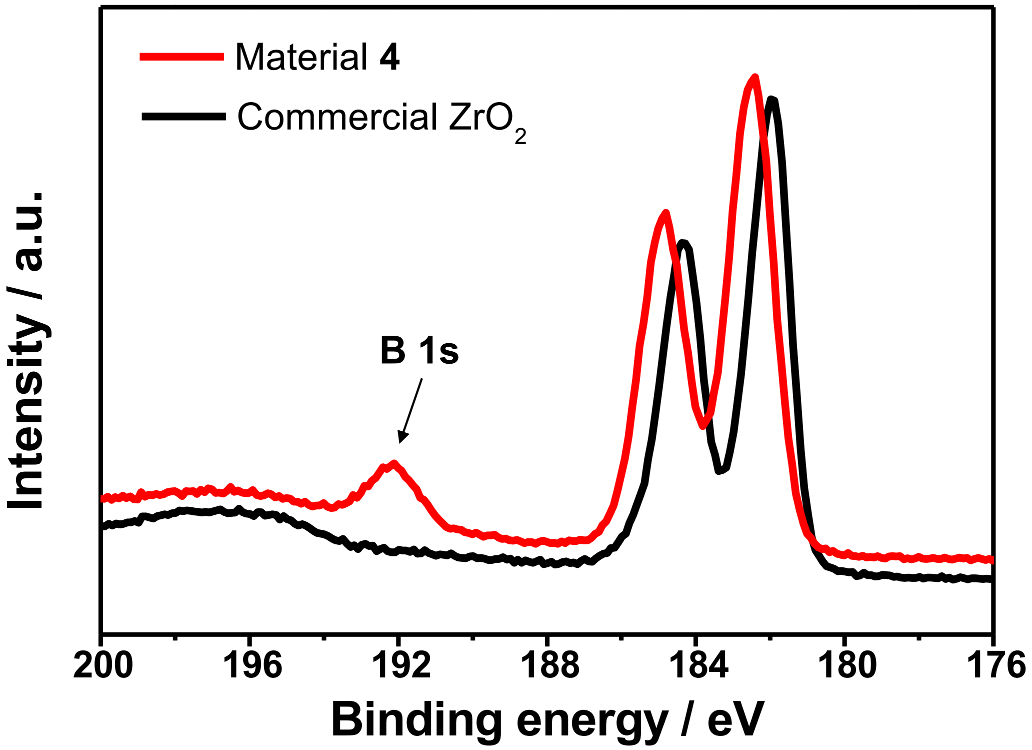

Fig. S53.

The zirconium 3*d* region of material **4** shows well-resolved spin-orbit components at 182.4 eV and 184.8 eV, indicating Zr^{4+}. The boron 1*s* region is overlapping with Zr *3d* region, but material **4** clearly shows a boron 1*s* peak at 192.1 eV.

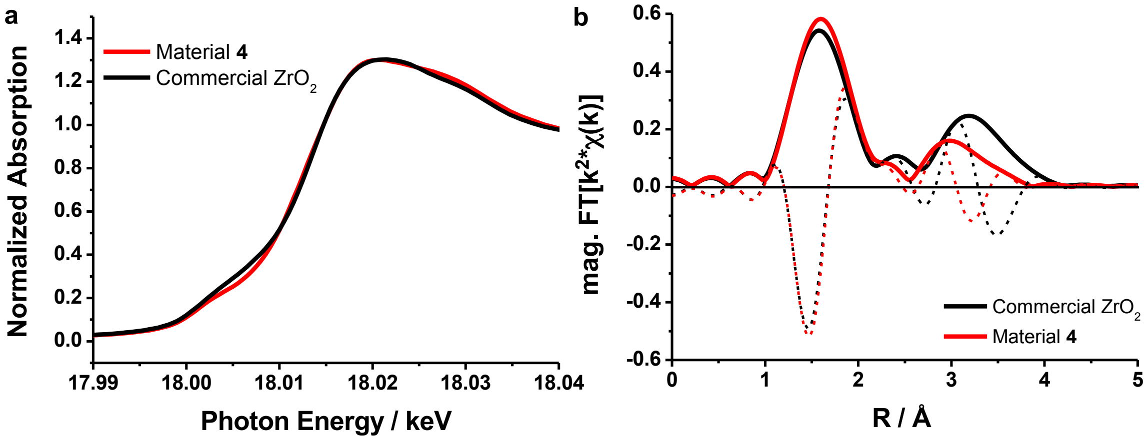

Fig. S54.

a, XANES measurements on material **4** were compared to that measured for ZrO_2. The Zr K edge structure for material **4** matches that found for zirconia, confirming the presence of zirconium exclusively in the 4+ oxidation state. **b**, The k-squared weighted EXAFS function of material **4** and ZrO_2. From this data, an average Zr O bond distance of 2.14 Å for ZrO_2 in material **4** can be extracted.

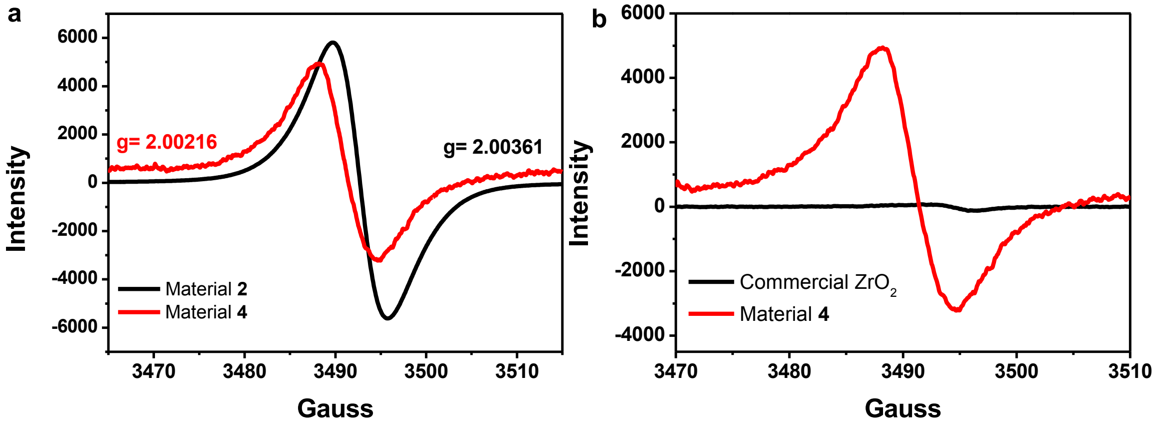

Fig. S55.

(**a**) Electroparamagnetic resonance (EPR) spectroscopy at room temperature of materials **2** and **4**. Each material produces a peak, with corresponding *g*-values of 2.00361 and, 2.00216 very close to that found for single molecular boron cluster radicals. The origin of the paramagnetism is related to **2** and the paramagnetism is perturbed when ZrO_2 is introduced to **2**. (b) EPR spectroscopy of material **4** plotted with data for ZrO_2. While commercial ZrO_2 showed the absence of paramagnetism, material **4** clearly produced a signal arise from cross-linked B_{12}-based clusters.

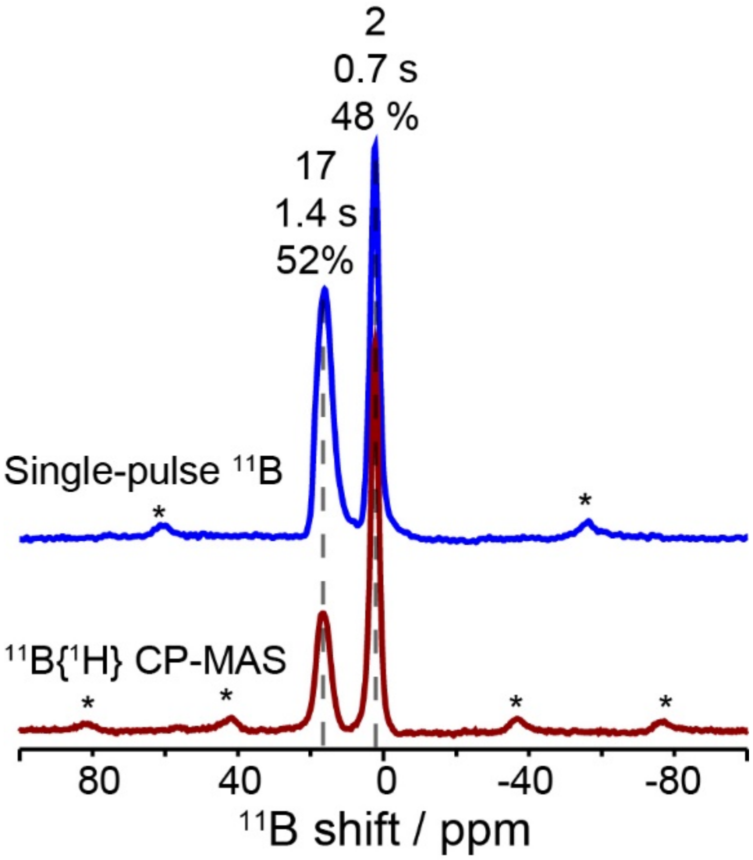

Fig. S56.

Solid-state 1D single-pulse ^{11}B MAS NMR (top) and ^{11}B{^{1}H} CP-MAS (bottom) spectra of material **4** acquired at 18.8 T and 298 K, showing two resolved ^{11}B signals at 2, and 17 ppm, assigned to surface boron clusters, and boron oxide/borates, respectively, and the corresponding percentages are 48 and 52 %, respectively.

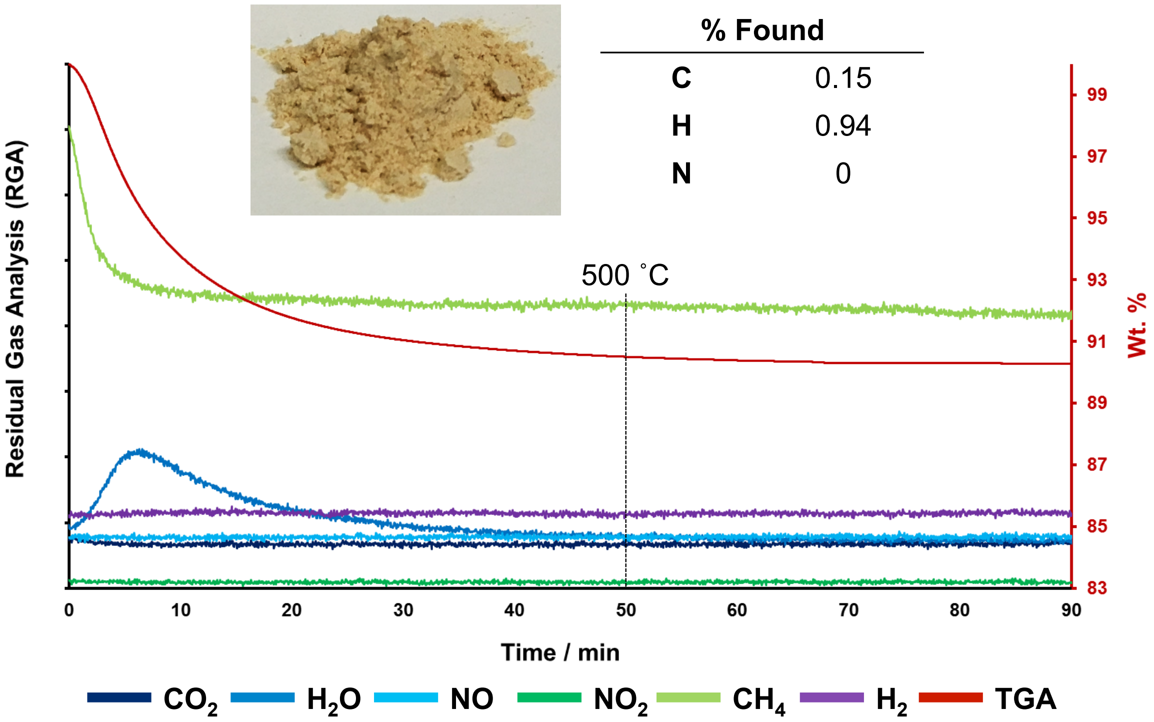

% Found	
C	0.15
H	0.94
N	0

Fig. S57.

TGA-mass spectroscopy (TGA-MS) of material **4**, showing the different mass loss events during the annealing process to form **4**. (A heating rate of 10 °C min^{-1} was used, therefore the scale can be read as: 10 mins= 100 °C). The elemental analysis shows material **4** contains ~0.15 % of carbon (inset table).

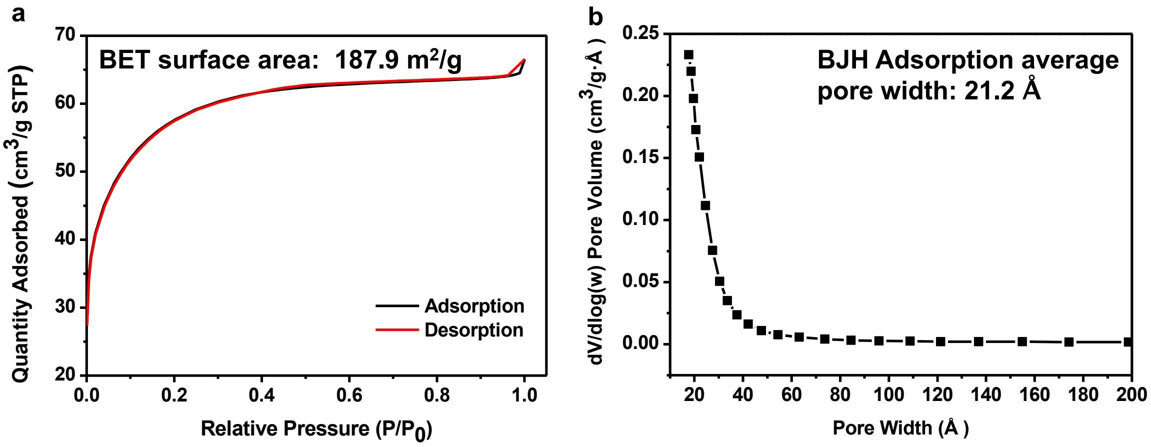

Fig. S58.

(**a**) Low pressure N_2 adsorption isotherms of material **4**. The Brunauer-Emmett-Teller (BET) surface area is 187.9 m^2/g; (**b**) Calculated pore size distribution of material **4** using the Barret-Joyner-Halenda (BJH) equation.

References

1. Pan, L. *et al*. Hierarchical nanostructured conducting polymer hydrogel with high electrochemical activity. *Proc. Natl. Acad. Sci. U.S.A.* **109,** 9287–9292 (2012).

2. To, J. W. F. *et al*. Ultrahigh surface area three-dimensional porous graphitic carbon from conjugated polymeric molecular framework. *ACS Cent. Sci.* **1,** 68–76 (2015).

3. Feng, N. *et al.* Boron environments in B-doped and (B,N)-codoped TiO_2 photocatalysts: a combined solid-state NMR and theoretical calculation study. *J. Phys. Chem. C* **115**, 2709–1719 (2011).

4. Rorschach, H. E. Nuclear relaxation in solids by diffusion to paramagnetic impurities, *Physica* **30,** 38–48 (1964).

5. Lowe, I. J. & Tse, D. Nuclear spin-lattice relaxation via paramagnetic centers. *Phys. Rev.* **166,** 2, 279–291 (1968).

6. Van, N. *et al.* Oxidative perhydroxylation of [*closo*-$B_{12}H_{12}$]$^{2-}$ to the stable inorganic cluster redox system [$B_{12}(OH)_{12}$]$^{2-/-}$: Experiment and theory. *Chem. Eur. J.* **16,** 11242–11245 (2010).

7. Zhong, J. -H. *et al*. Quantitative correlation between defect density and heterogeneous electron transfer rate of single layer graphene. *J. Am. Chem. Soc.* **136,** 16609–16617 (2014).

8. Boopathi, S., Narayanan, T. N., Kumar, S. S. Improved heterogeneous electron transfer kinetics of fluorinated graphene derivatives. *Nanoscale* **6,** 10140–10146 (2014).

9. Mao, X., Guo, F., Yan, E. H., Rutledge, G. C., Hatton, T. A. Remarkably high heterogeneous electron transfer activity of carbon-nanotube-supported reduced graphene oxide. *Chem. Mater.* **28,** 7422–7432 (2016).

10. Odriozola, J. A., Heinemann, H., Somorjai, G. A., Garcia de la Banda, J. F., Pereira, P.

AES and TDS Study of the adsorption of NH_3 and NO On V_2O_5 and TiO_2 Surfaces: Mechanistic implications. *J. Catal.* **119,** 71 (1989).

11. Saxman, A. M., Liepins, R., Aldissi, M. Polyacetylene: Its Synthesis, Doping, and Structure. *Pro. Polym. Sci.* **11,** 57–89 (1985).

12. Tian, H., Xin, F., Tan, X., Han, W. High lithium electroactivity of boron-doped hierarchical rutile submicrosphere TiO_2. *J. Mater. Chem. A* **2,** 10599 (2014).

CHAPTER 3

CROSS-LINKED TUNGSTEN OXIDES FOR ENERGY STORAGE APPLICATIONS

Abstract

As a continuation of using a $[B_{12}(OH)_{12}]^{2-}$ cluster as molecular cross-linker, we report a synthesis of a hybrid tungsten oxide material. The exhaustive structural characterization of the cross-linked tungsten oxide with the molecular boron cluster is elaborated in this chapter. The potential utilization of this hybrid material for pseudocapacitor is also discussed. Although our preliminary results show a promising energy storage capability, further study is necessary to fully understand the electrochemical properties of the hybrid tungsten oxide material.

Introduction

Supercapacitors have attracted tremendous interest in the field of rechargeable batteries due to their high power density, excellent low temperature performance and essentially unlimited charge/discharge cycles.[1] Based on energy storage mechanisms, supercapacitors can be divided into two categories: electrochemical double-layer capacitors (EDLC) and pseudocapacitors. In EDLCs, they store charge via ion adsorption at the interface between the electrode and electrolyte, forming electric double layers. This non-Faradaic process enables supercapacitors to be fully recharged rapidly.[2] Recently, pseudocapacitors have emerged as a new class of materials for supercapacitors with superior electrochemical performance. Pseudocapacitors store charge via reversible redox Faradaic reactions, which leads to store a larger amount of capacitance than EDLC. Conductive polymers and metal oxides have been extensively studied as an active material for pseudocapaticors.[3,4]

Our group previously reported a cross-linked TiO_2 material with dodecaborate clusters, $[B_{12}(OH)_{12}]^{2-}$ (referred to herein as **I**) which exhibited enhanced electrochemical behavior compared to the pristine TiO_2.[5] Specifically, the cross-linked boron-rich clusters confer conductive nature to TiO_2 network and nano-sized TiO_2 particles interconnected with the boron-rich clusters provide a larger electrode-electrolyte contact area with reduced ionic diffusion resistance and charge transfer resistance. However, the inherently poor electrochemical property and low electrical conductivity of TiO_2 limit its application for supercapacitor electrodes. Therefore, we envisioned that **I** can be incorporated into other metal oxides with superior electrochemical properties such as tungsten oxide[6] in order to improve the performance of the hybrid metal oxide material as a supercapacitor.

Results and Discussion

We conducted a reaction between **I** and WCl_6 using a bench-top microwave reactor to create a cross-linked tungsten oxide with a B_{12}-based cluster. Reaction of **I** with 1 equivalent of WCl_6 (B:W=12:1) in acetonitrile formed a red-orange gel which was subsequently rinsed with ethanol three times and dried at 120 °C for 2 h (Fig. 3.1).

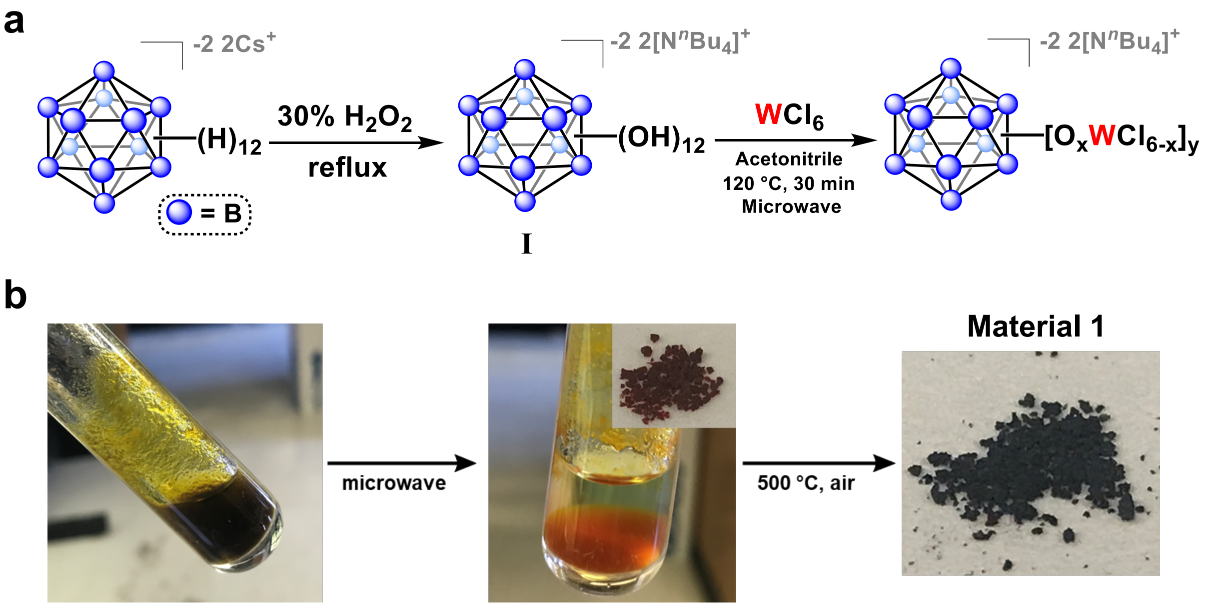

Figure 3.1. (a) Synthetic route to produce a cross-linked tungsten oxide material with dodecaborate clusters. (b) A mixture of **I** and WCl_6 in CH_3CN before (left) and after (middle) the microwave reaction, and material **1** after annealing at 500 °C (right).

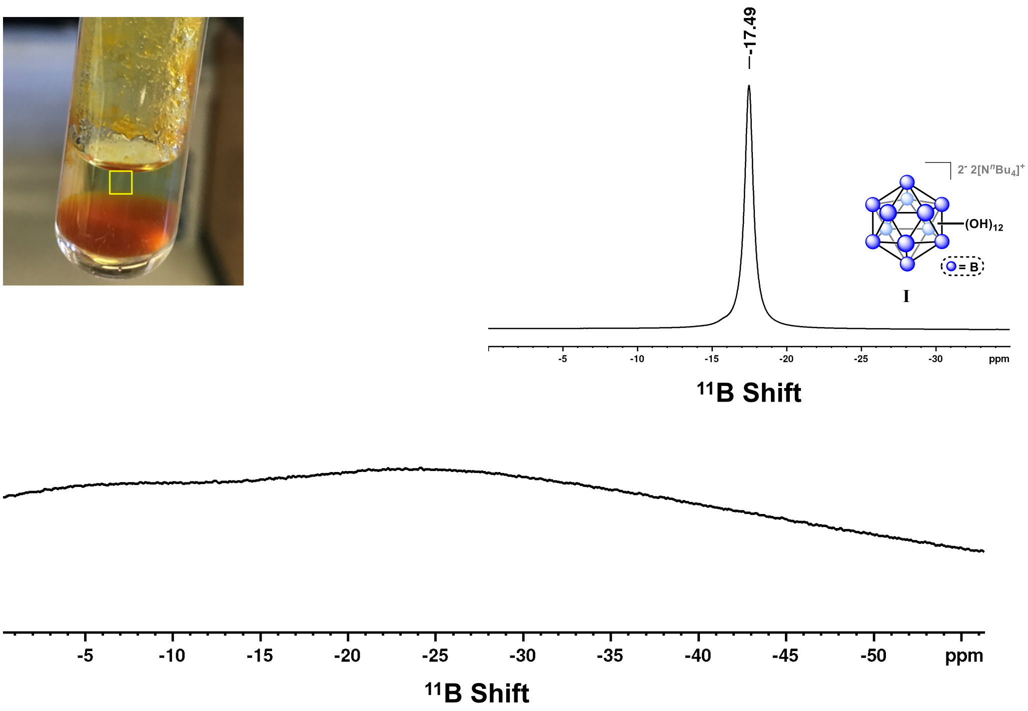

Figure 3.2 ^{11}B solution NMR of the supernatant liquid after the reaction between **I** and WCl_6. (Inset) ^{11}B NMR of **I** in CD_3CN.

The supernatant liquid was subject to ^{11}B solution nuclear magnetic resonance (NMR) spectroscopy to identify the presence of unreacted B_{12}-based clusters. The ^{11}B solution NMR shows no boron containing species in the supernatant liquid, confirming all the boron-rich clusters were consumed in the reaction (Fig. 3.2). The dried sample was then subjected to annealing at 500 °C for 3 h and was recovered as a black solid (referred to herein as material **1**) (Fig. 3.1b). The structure of the cross-linked tungsten oxide material was characterized by powder X-ray diffraction (PXRD), scanning electron microscopy (SEM), transmission electron microscopy (TEM), X-ray photoelectron spectroscopy (XPS), and solid-state NMR (SSNMR) spectroscopy. The PXRD data shows material **1** possesses crystalline monoclinic phase based on comparison to the reference monocline WO_3.[7] The broad peaks in PXRD can be attributed to the small crystal size of WO_3 (< 10 nm) in material **1**. The surface morphology and elemental analysis of material **1** were obtained using SEM and energy dispersive X-ray spectroscopy

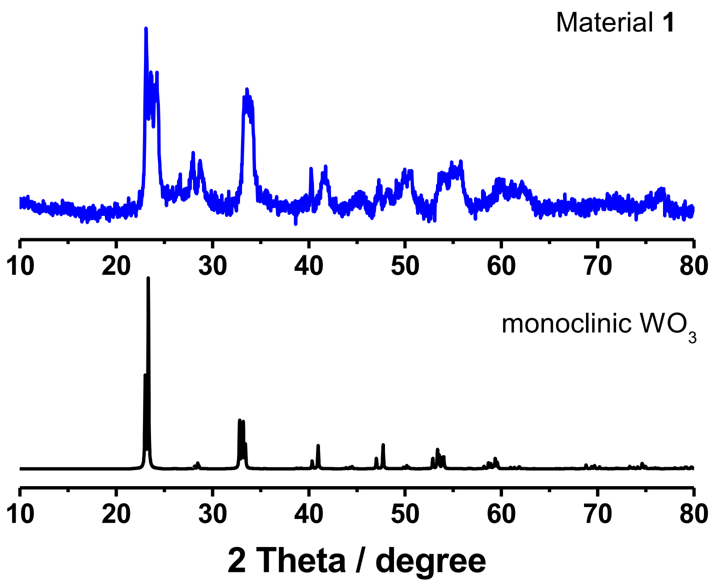

Figure 3.3. PXRD of material **1** (top) and monoclinic WO_3 (bottom).[7]

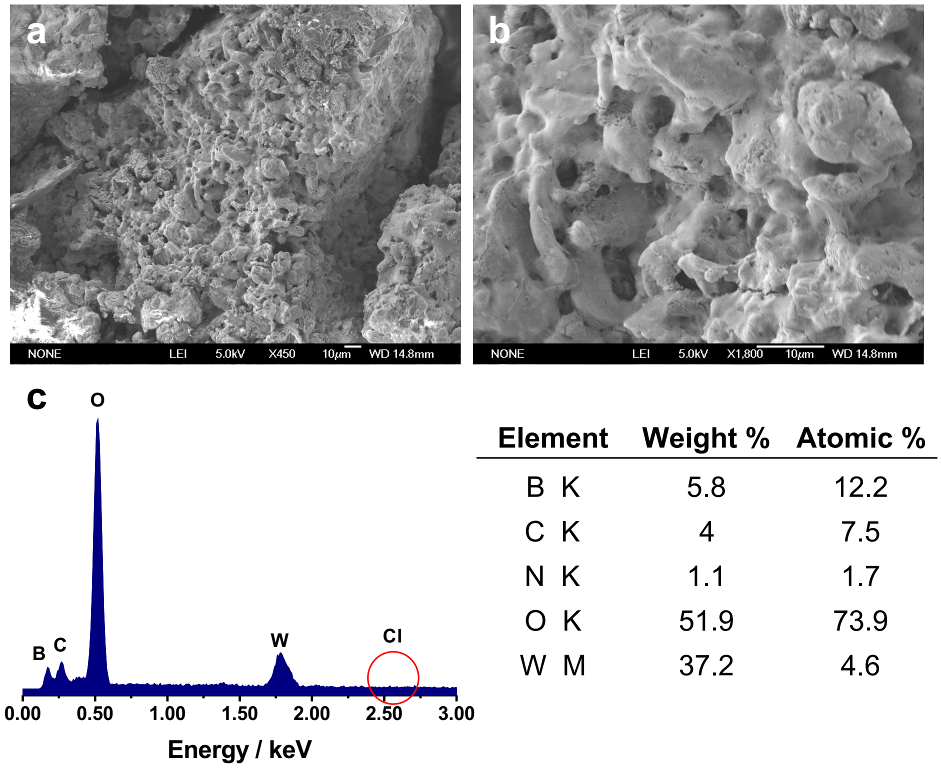

Element	Weight %	Atomic %
B K	5.8	12.2
C K	4	7.5
N K	1.1	1.7
O K	51.9	73.9
W M	37.2	4.6

Figure 3.4. (a,b) SEM images and (c) EDS results (left) and atomic composition (right) of material **1**.

(EDS). The SEM images of **1** suggest the likely formation of porous structure upon cross-linking boron-rich clusters to the tungsten oxide network (Fig. 3.4a,b). Moreover, the elemental analysis shows that the material **1** consists of B, O, W and C with 12.2, 73.9, 4.6 and 7.5 at %, respectively (Fig. 3.4c).

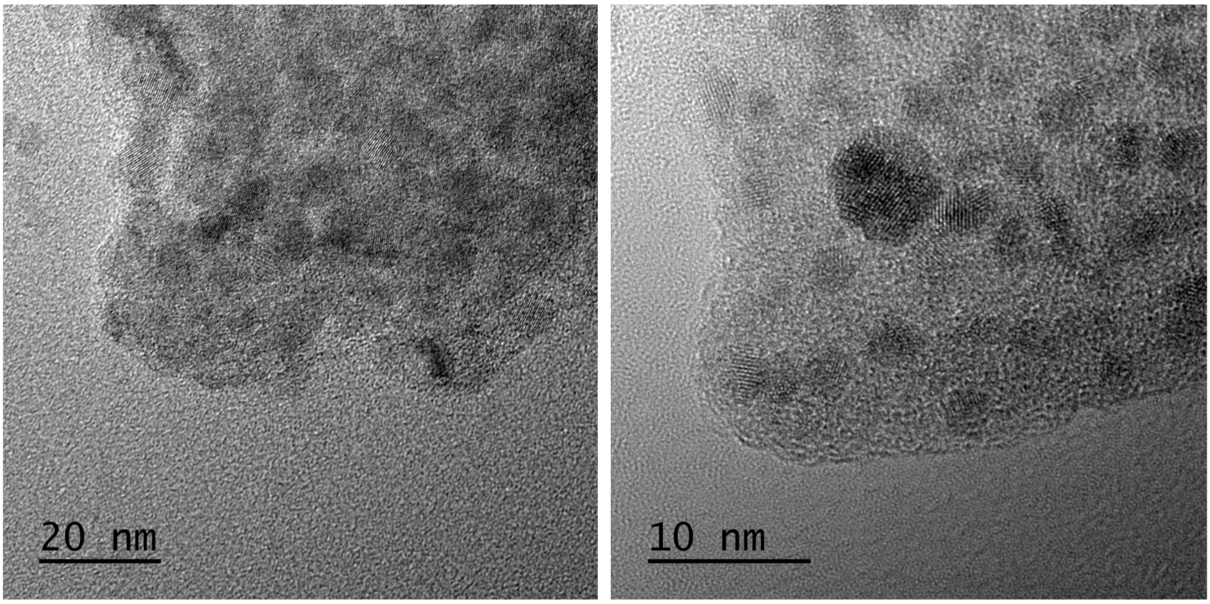

Figure 3.5. TEM images of material **1**.

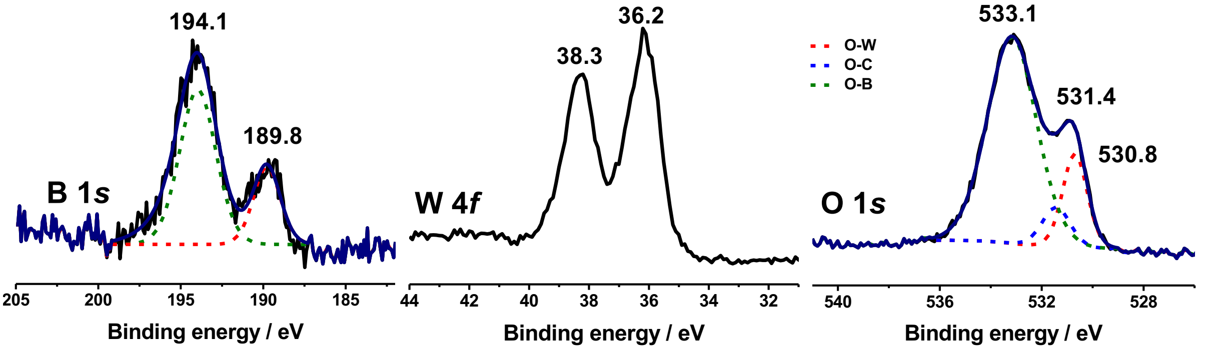

Figure 3.6. XPS of material **1**.

The carbon present in material **1** is likely trapped into the molecular framework during the annealing process. Noticeably, no chlorine from the starting material was detected, demonstrating B–O–W linkage is possibly formed through the reaction between **I** and WCl_6.

High-resolution TEM (HRTEM) images of material **1** highlight the cross-linked morphology where nanocrystalline WO_3 particles are embedded in the cross-linked network of intact boron clusters and boron oxide. XPS measurements were performed to reveal the surface environment of material **1**. The boron 1s region exhibits two components at 189.8 and 194.1 eV, corresponding to the intact dodecaborate clusters and boron oxide/borates, respectively. The W 4f XPS spectra consist of two peaks of $4f_{7/2}$ and $4f_{5/2}$ at 36.2 and 38.3 eV, respectively. The binding energy of W 4f indicates the presence of W(VI) in the sample. The O 1s region shows multiple components at 530.8, 531.4, and 533.1 eV, which can be assigned to O–W, O–C, and O–B, respectively. Moreover, the atomic compositions obtained from XPS measurements demonstrate that boron (21 %) and oxygen (51%) are dominant while there is only 5 % of tungsten at the surface. This result is consistent with the TEM image of material **1** which describes that tungsten oxide nanoparticles are embedded in the molecular boron oxide.

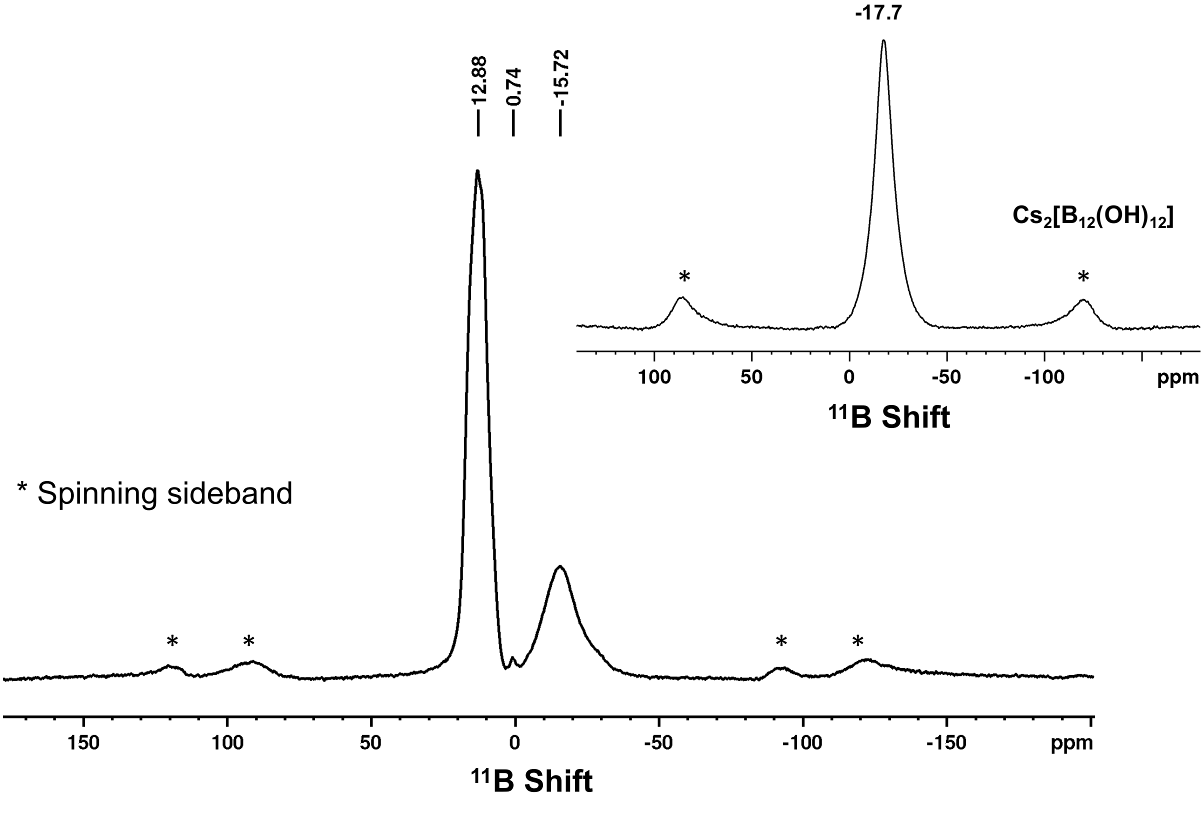

Figure 3.7. ^{11}B MAS SSNMR of material **1** and a reference $Cs_2[B_{12}(OH)_{12}]$ (inset).

The presence of intact B_{12}-based clusters in material **1** can be directly detected using solid-state ^{11}B NMR. The 1D single-pulse ^{11}B magic angle spinning (MAS) SSNMR of material **1** shows three distinct features. The peak at -15.7 ppm can be assigned to the sub-surface dodecaborate clusters directly connected to the tungsten oxide network. Two additional signals at 0.7 and 12.9 ppm are attributed to the partially intact B_{12}-based clusters at the surface and to boron oxide or borates, respectively.[5] The combined structural characterizations of material **1** validate the hybrid molecular boron oxide material composed of nano-crystalline WO_3 particles in the monocline phase cross-linked with $[B_{12}(OH)_{12}]^{2-}$ clusters.

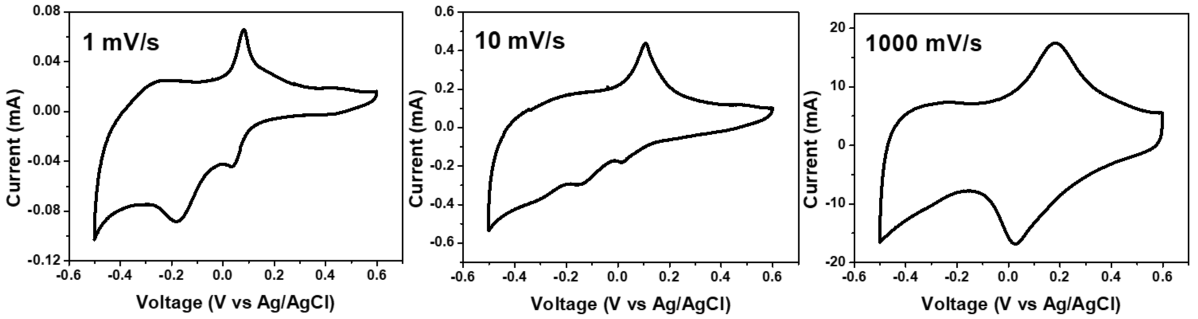

Figure 3.8. Cyclic voltammograms (CV) of material **1** at different scan rates in 2.0 M H_2SO_4.

Given the potential redox activity of material **1**, we investigated the electrochemical properties of this material using a 3-electrode electrochemical cell. The cyclic voltammetry (CV) of material **1** shows clear two pairs of reduction/oxidation peaks in 2.0 M H_2SO_4 at a scan rate of 1 mV/s. These peaks can be attributed to the following reactions[8]:

$$\mathbf{WO_{3-x} + ne^- + nH^+ \rightleftharpoons H_nWO_{3-x}}$$

$$\mathbf{H_nWO_{3-x} + (n-1)e^- + (n-1)H^+ \rightleftharpoons HWO_{3-x}}$$

Interestingly, as the scan rate increases to 1000 mV/s, two reduction peaks are combined and the material exhibits reversible oxidation and reduction feature. In order to understand the detailed electrochemical reactions of material **1**, we synthesized a series of control materials such as pure monoclinic WO_3 and hybrid tungsten oxide materials with different ratios of B to

W (B:W= 2:1, 1:1, and 1:2). Further investigation of the electrochemical reation will be performed to on these controls.

Conclusions & Future work

We have reported a successful synthesis of cross-linked tungsten oxides using a dodecaborate cluster building block as a molecular cross-linker. The comprehensive structural characterization of material **1** supports the formation of a cross-linked hybrid metal oxide consisted of intact molecular boron oxides with tungsten oxide nanoparticles embedded. The three-electrode electrochemical cell measurements suggest that material **1** is redox active and can potentially be used as an active material for pseudocapacitor. However, further investigation is required to fully understand the electrochemical properties of material **1**. We expect the inherent robustness of **I** would enhance its cycling stability and rate capacity compared to the pristine WO_3, maintaining the capacitance after multiple cycles and at high scan rates.

Methods

Materials: Deuterated solvents were purchased from Cambridge Isotope Laboratories and used as received. The following chemicals were purchased from commercial vendors: tungsten hexachloride (Acrosorganics).

Cesium and $[N^nBu_4]^+$ salts of $[B_{12}(OH)_{12}]^{2-}$ were synthesized by previously reported methods.[9]

Synthesis of Material 1: The preparation of the microwave reaction was carried out in an inert atmosphere dry-box. In a 10 ml glass microwave vial, WCl_6 (24 mg, 0.0611 mmol) in acetonitrile (1 ml) was added to a stirring suspension of $[N^nBu_4]_2[B_{12}(OH)_{12}]$ (50 mg, 0.0611 mmol) in acetonitrile (0.5 ml). The reaction vial was sealed with a PTFE/silicone cap and then brought outside of the dry-box. The mixture was heated at 120 °C with stirring in the microwave for 30 min. The red-orange gel reaction mixture was washed with ethanol three times and dried at 80 °C for 2 h. The dried powder was annealed by heating from room temperature to 500 °C at a rate of 10 °C/min and holding at 500 °C for 3 h. Then, the furnace was cooled to room temperature at a rate of 1 °C/min.

Characterization Methods and Instrumentation: Powder X-ray diffraction (PXRD) was performed on a Panalytical X'Pert Pro X-ray Powder Diffractometer with Cu-Kα radiation. Diffraction spectra were collected from a 2θ angle of 10 to 80 degree with a step size of 0.04 degree at a rate of 1 degree/min. High-resolution transmission electron microscopy (HRTEM) was performed using a FEI Titan S/TEM operated at 300 kV. X-ray photoelectron spectroscopy (XPS) was undertaken using an AXIS Ultra DLD instrument (Kratos Analytical Inc., Chestnut Ridge, NY, USA). All XPS spectra were obtained using a monochromatic Al Kα X-ray source (12 mA for both survey and high-resolution scans, 15 kV) with a 300 x 700 nm oval spot size. The pressure of analyzer chamber was maintained below 1×10^{-8} Torr during the measurement. Spectra were collected with 160 eV pass energy for survey spectra and 20 eV for high-resolution spectra of C 1*s*, O 1*s*, B 1*s*, and W 4*f*. All XPS peaks were charge referenced to the adventitious carbon 1*s* signal at 284.6 eV. Scanning electron microscopy (SEM) was undertaken using a field-emission SEM (JEOL JSM 6700F). ^{11}B solution NMR spectra were recorded in acetonitrile on AV 400 spectrometers in ambient conditions. ^{11}B solid-state magic angle spinning (MAS) nuclear magnetic resonance (NMR) spectra were acquired on a 600 MHz (14.1 T) Bruker AVANCE III HD spectrometer using a 3.2 mm HXY MAS probe. The MAS frequency used was 20 kHz for ^{11}B. The ^{11}B background signal from the MAS probe was suppressed using the EASY sequence.[10] The ^{11}B chemical shift was indirectly referenced to $BF_3O(CH_2CH_3)_2$ in $CDCl_3$ by using $Cs_2[B_{12}(OH)_{12}]$ (δ=-17.4 ppm).[5] The RF field for the ^{11}B central transition selective pulse was 66 kHz.

Electrochemical measurements: The working electrode was prepared by mixing 80 wt% of material **1** in N-methyl pyrrolidone (NMP) with 10 wt% of polyvinylidene fluoride (PVDF) and 10 wt% of carbon black, working as a binder and conductive additive, respectively. The mixture was drop-casted on graphite paper and dried at 80 °C for a few hours. For the measurements, a three-electrode configuration was used with a platinum foil as a counter electrode and Ag/AgCl as a reference electrode in 2.0 M H_2SO_4.

References

1. Wang, G., Zhang, L., Zhang, J. “A Review of Electrode Materials for Electrochemical Supercapacitors.” *Chem. Soc. Rev.* **41**, 797−828 (2012)
2. El-Kady, M. F., Shao, Y., Kaner, R. B. "Graphene for Batteries, Supercapacitors and Beyond." *Nature Rev. Mater.* **1**, 16033 (2016).
3. Zuo, W., Li, R., Zhou, C., Li, Y., Xia, J., Liu, J. "Battery- Supercapacitor Hybrid Devices: Recent Progress and Future Prospects." *Adv. Sci.* **4**, 1600539 (2017).
4. Zhi, M., Xiang, C., Li, J., Li, M., Wu, N. “Nanostructured Carbon-Metal Oxide Composite Electrodes for Supercapacitors: a Review.: Nanoscale 5, 72 (2013).
5. Jung, D., Saleh, L. M. A., Berkson, Z. J., El-Kady, M. F., Hwang, J. Y., Mohamed, N., Wixtrom, A. I., Titarenko, E., Shao, Y., McCarthy, K., Guo, J., Martini, I. B., Kraemer, S., Wegener, E. C., Saint-Cricq, P., Ruehle, B., Langeslay, R. R., Delferro, M., Brosmer, J. L., Hendon, C. H., Gallagher-Jones, M., Rodriguez, J., Chapman, K. W., Miller, J. T., Duan, X., Kaner, R. B., Zink, J. I., Chmelka, B. F. & Spokoyny, A. M. A Molecular Cross-Linking Approach for Hybrid Metal Oxides. *Nat. Mater*. **17**, 341−348 (2018).
6. Sun, W., Yeung, M. T., Lech, A. T., Lin, C.-W., Lee, C., Li, T., Duan, X. Zhou, J., Kaner, R. B. *Nano Lett*. **15**, 4834-4838 (2015).
7. Jain, A.,* Ong, S.P.,* Hautier, G., Chen, W., Richard, W.D., Dacek, S., Cholia, S., Gunter, D., Skinner, D., Ceder, G., Persson, K. A. (*= equal contributions) *APL Materials*, **1**, 011002 (2013).
8. Cong, S., Tian, Y., Li, Q., Zhao, Z., Feng, F. *Adv. Mater.* **26**, 4260-4267 (2014).
9. Wixtrom, A. I., Shao, Y., Jung, D., Machan, C. W., Kevork, S. N., Qian, E. A., Axtell, J. C., Khan, S. I., Kubiak, C. P., Spokoyny, A. M. *Inorg. Chem. Front.*, **3**, 711–717 (2016).
10. Jaeger, C., Hemmann, F. *Solid State Nucl. Mag.* **57**, 22–28 (2014).

CHAPTER 4

CROSS-LINKED POROUS POLYURETHANE MATERIALS FEATURING DODECABORATE CLUSTERS AS INORGANIC POLYOL EQUIVALENTS

This chapter is a version of Jung, D.; Raffan-Montoya, F.; Ramachandran, R.; Zhang, Y.; Islamoglu, T.; Marin, G.; Qian, E. A.; Dziedzic, R. M.; Farha, O. K.; Stoliarov, S. I.; Spokoyny, A. M. "Cross-linked Porous Polyurethane Materials Featuring Dodecaborate Clusters as Inorganic Polyol Equivalents", *Chem. Commun. In press* (Special Issue on Emerging Investigators).

Abstract

We report the discovery that a perhydroxylated dodecaborate cluster ($[B_{12}(OH)_{12}]^{2-}$) can act as an inorganic polyol, serving as a molecular cross-linker in the synthesis of polyurethane-based materials. We further demonstrate how the inherent robustness of the utilized boron cluster can effectively enhance the thermal stability of the produced polyurethane materials incorporating $[B_{12}(OH)_{12}]^{2-}$ building blocks compared to analogous polymers made from carbon-based polyols. Ultimately, this approach provides a potential route to tune the chemical and physical properties of soft materials through incorporation of polyhedral boron-rich clusters into the polymer network.

Introduction

Since the discovery of the vulcanization of natural rubber, cross-linking has been essential in polymer chemistry to improve the thermal, physical and mechanical properties of synthetic macromolecules.[1] Specifically, adding cross-linkers to polymer chains can affect several features in polymers such as elasticity, solubility, and mechanical strength, depending on the cross-linker density and its chemical nature.[2-4] Over the past several decades, researchers have developed numerous cross-linking approaches including the use of linker agents that can interact with the polymer chains in a non-covalent and covalent manner. The latter approach was previously shown to increase chemical and physical stability in polymer networks due to the robust and irreversible nature of covalent cross-linking agents.[5-7]

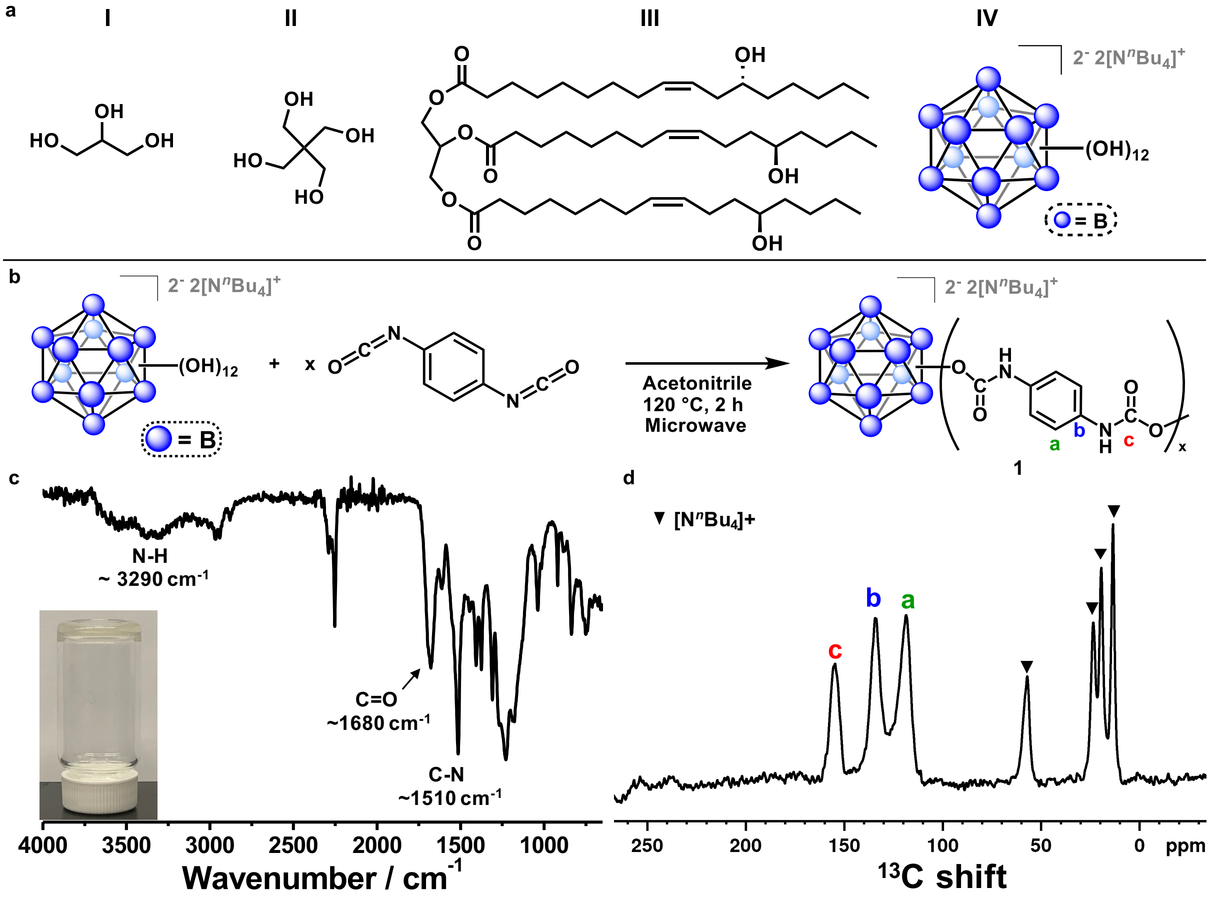

Figure 4.1 (a) Overview of existing polyols for the synthesis of polyurethane materials: glycerol (**I**); pentaerythritol (**II**); castor-oil (**III**), and, in this work, a dodecaborate cluster (**IV**), (b) Synthetic route to produce densely cross-linked polyurethanes, utilizing the polyhedral boron cluster $[N^{n}Bu_4]_2[B_{12}(OH)_{12}]$ as a robust inorganic polyol, (c) FT-IR and (inset) photo of **1**, (d) Solid-state 1D single-pulse ^{13}C MAS NMR of **1**.

Polyurethanes represent one of the most extensively studied classes of polymers due to their versatile properties offering a wide range of applications ranging from rigid foam insulation panels to high performance adhesives.[8-10] Polyurethanes are prepared via condensation of diisocyanates and polyols to form urethane linkages. Consequently, the chemical and physical properties of polyurethanes can be altered by employing different types of isocyanates and polyols. In addition, covalent cross-linking has been shown to play an important role in determining the properties of polyurethane materials.[11,12] Recently, bio-derived polyols obtained from vegetable oils have attracted significant interest as cross-linkable polyols, with the potential to replace petroleum-based polyols. Although these bio-based polyols exhibit reduced impacts on the environment, the lower reactivity of their hydroxyl groups relative to the primary hydroxyl groups in the petroleum-based polyols and high flammability of the resulting bio-based polyurethanes necessitate significant structural modifications to bio-derived polyols.[14,15] While a vast amount of research has been carried out on organic-based polyols such as glycerol (**I**), pentaerythritol (**II**) and castor oil (**III**) (Fig. 4.1a),[13-15] surprisingly, there has been no reported effort in assessing purely inorganic-based molecular polyols for producing cross-linked polyurethanes. In this work, we introduce a perhydroxylated dodecaborate cluster, $\mathbf{[B_{12}(OH)_{12}]^{2-}}$, (referred to as **IV**)[16] as an inorganic polyol equivalent, which serves as a hyper cross-linker possessing multiple cross-linking sites to generate porous polymers.[6] We show that upon reaction with a model diisocyanate linker, boron-rich **IV** can form multiple urethane linkages to produce a porous polyurethane-based material with enhanced thermal stability compared to an analogue containing a carbon-rich cross-linker.

Results & Discussion

Our group recently developed a "molecular cross-linking" approach to create hierarchical hybrid metal oxide materials using **IV**.[17] Based on these observations, we envisioned that the molecular cross-linking approach can be further expanded to organic molecules to form densely cross-linked polymeric networks.[18-21] Specifically, we hypothesized that **IV** can be a suitable polyol system that can potentially react with isocyanates to generate urethane linkages. Given that the molecular scaffold of **IV** can withstand harsh thermal and oxidizing conditions,[22-24] we further hypothesized that cross-linking these clusters in polyurethane materials would enhance thermal stability and potentially improve other properties of the resulting polymeric materials. To test our hypothesis, we conducted a model reaction between **IV** and *p*-tolyl isocyanate using a bench-top microwave reactor (see ESI†). When 60 equivalents of *p*-tolyl isocyanate were mixed with **IV** and heated for 2 hours at 100 °C in acetonitrile, a complete substitution of the starting cluster material was observed by nuclear magnetic resonance (NMR) spectroscopy, Fourier-transform infrared spectroscopy (FT-IR), and electrospray ionization mass spectrometry (ESI-MS) (see ESI†). This model experiment

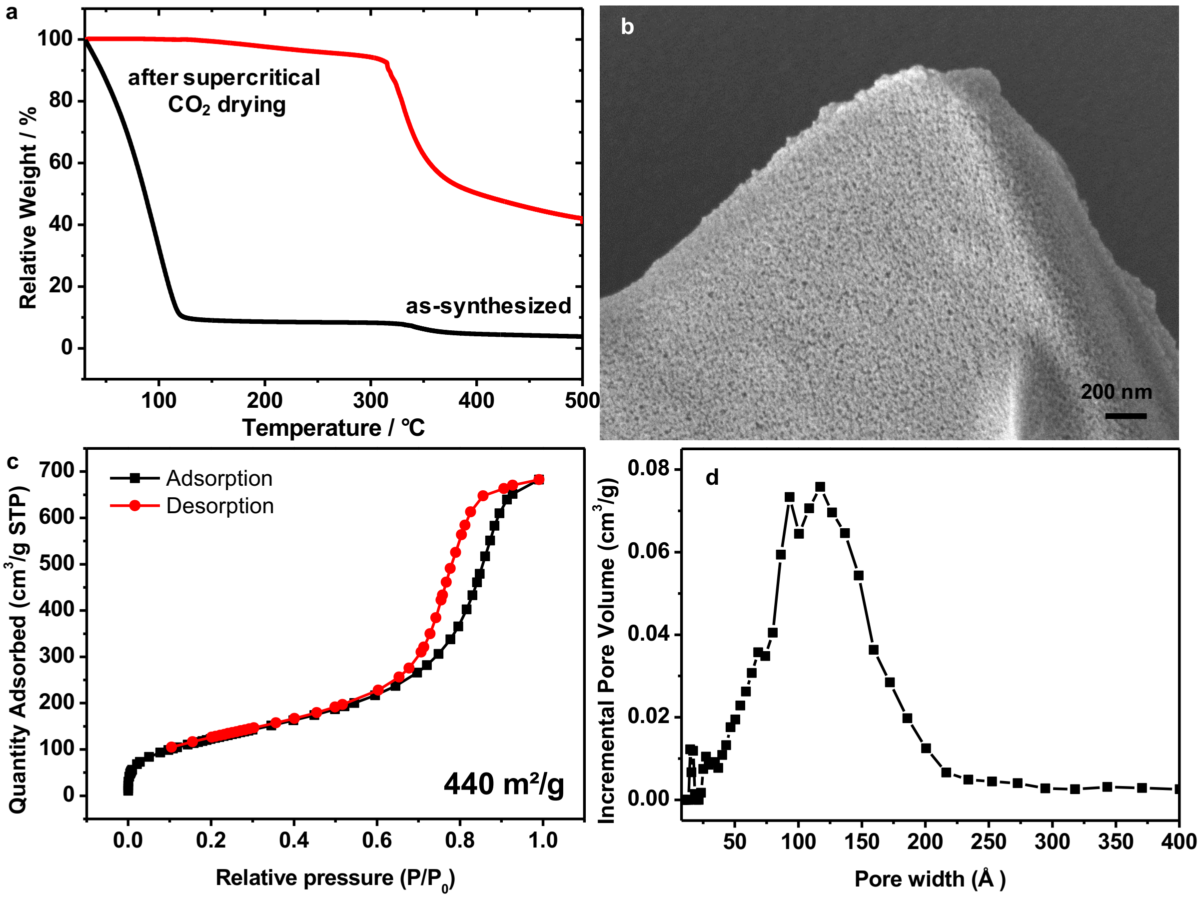

Figure 4.2 (a) TGA results of **1**, (b) SEM image, (c) N_2 adsorption and desorption isotherms

at 77 K, (d) Pore size distribution of **1** following supercritical CO_2 activation.

suggested that B-OH groups in **IV** could indeed behave as competent nucleophiles to form urethane linkages with isocyanates. We then performed condensation polymerizations utilizing 1,4-phenylene diisocyanate (PDI) with **IV** to ascertain whether this cluster can be used as a polyol equivalent in the synthesis of a model polyurethane-based material (Fig. 4.1b). We used stoichiometric amounts of functional groups (NCO:OH=1:1) to produce the cross-linked polymer, **1**. The reaction produced a viscous mixture and a gel (referred to herein as **1**) was formed within 24 hours, suggesting the likely formation of a cross-linked polymer network (Fig. 4.1c inset and ESI†). The FT-IR spectrum of **1** displayed the characteristic features of N-H (3290 cm^{-1}), C=O (1680 cm^{-1}), and C-N stretching (1510 cm^{-1}) coupled with N-H bending, which corroborated the formation of the urethane linkage (Fig. 4.1c).[25] More importantly, there was no unreacted isocyanate present in the product based on the absence of a peak at 2270 cm^{-1}, corresponding to the free isocyanate (ESI†). Further structural characterization of **1** was obtained using 1D solid-state ^{11}B and ^{13}C magic-angle-spinning (MAS) NMR spectroscopy. The 1D ^{11}B MAS NMR spectrum of **1** showed a sharp signal at -17 ppm, which can be assigned to intact B_{12}-based clusters (ESI†). The ^{13}C MAS NMR showed four signals at 13.3, 19.2, 23.3, and 57.0 ppm corresponding to the alkyl carbon-based resonances of the butyl groups in $[N^{n}Bu_4]^+$ cation. Two signals in the aromatic carbon region (118.6 and 134.2 ppm) arise from the aryl ring in PDI, and the characteristic peak at 154.7 ppm can be assigned to the carbonyl group in the urethane linkage (Fig. 4.1d). These combined structural characterizations of the material validate the successful formation of cross-linked polyurethane networks and the incorporation of **IV** into the polymer. The thermal stability of **1** was investigated using thermogravimetric analysis (TGA). The TG curve of the as-synthesized gel showed a significant weight loss (90%) around 80 °C due to the trapped solvent, acetonitrile, suggesting a highly porous network of the gel (Fig. 4.2a). The hypothesized porous morphology of the material **1** prompted us to collect N_2 isotherm at 77 K which then was used for Brunauer-Emmett-Teller (BET) surface area and pore size distribution calculations. For this analysis, we activated the polymer gel using a supercritical CO_2 drying method to avoid a collapsing of the structure upon solvent removal (ESI†).[26] The shape of the N_2 isotherm in Figure 2c is representative of a Type IV isotherm, indicating a mesoporous structure with a calculated BET surface area of 440 m^2/g (Fig. 4.2c). The surface morphology obtained by scanning electron microscopy (SEM) and the pore size distribution obtained from N_2 isotherm further confirmed the mesoporous structure of the material (Fig. 4.2b, d). We then examined the thermal stability of the dried polymer using TGA and observed the decomposition of urethane groups at 330 °C (Fig. 4.2a). This result demonstrates the notably enhanced thermal stability of material **1**

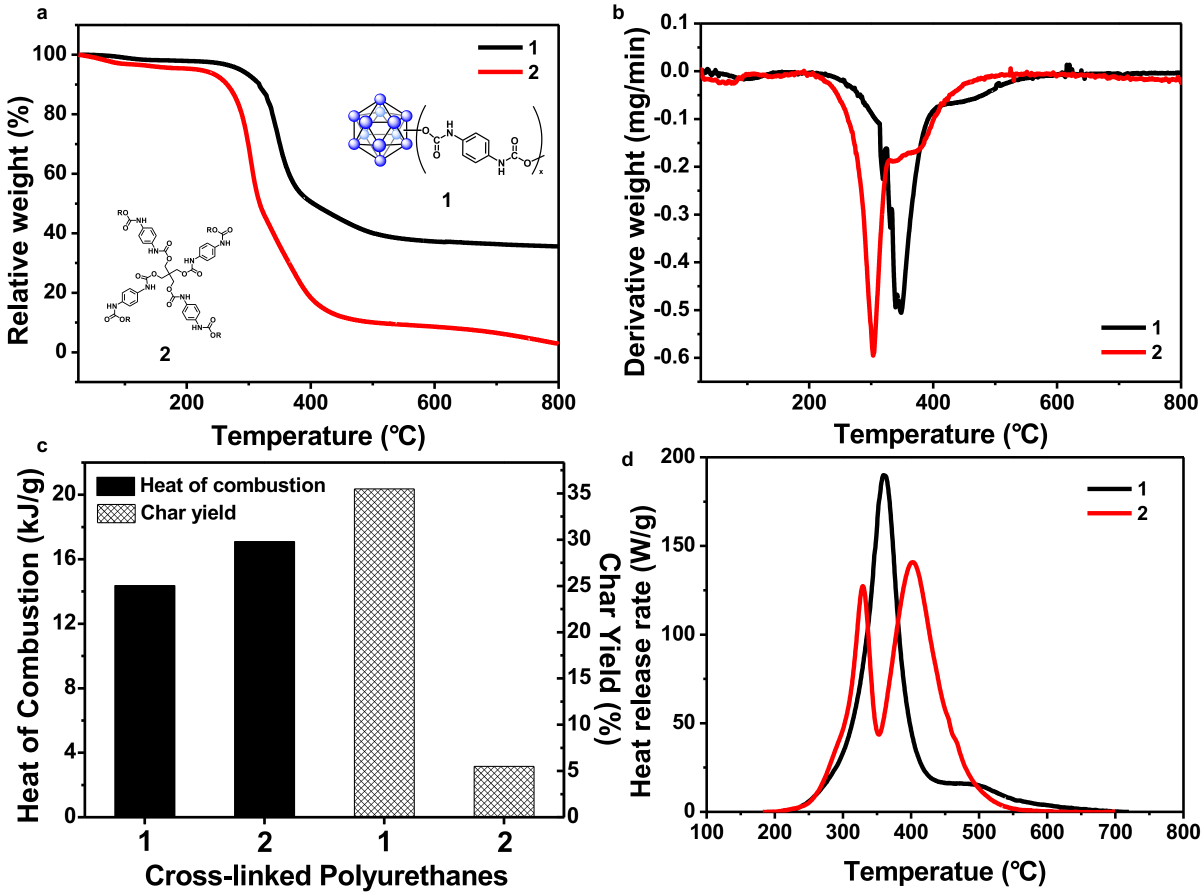

Figure 4.3 (a) Thermogravimetric, (b) derivative thermogravimetric results of **1** and **2**, (c) micro combustion calorimetry (MCC) results, (d) comparison of heat release rate of **1** and **2**.

compared to the reported thermal decomposition temperature range (120–250 °C) for polyurethanes obtained using organic polyols.[27]

We then compared the thermal behavior of **1** with an analogue (referred to herein as **2** and see ESI†) containing carbon-rich cross-linker **II**. The TGA and the derivative thermogravimetric (DTG) results showed that **1** possesses higher initial and maximum decomposition temperatures and % residual mass at 800 °C than **2**, highlighting the enhanced thermal stability of **1** in comparison to organic cross-linked analogue **2** (Fig. 4.3a, b and ESI†). These improved thermal properties of **1** can be attributed to the robust cross-linker, **IV,** present in **1** which provides more cross-linking sites than **II**, and consequently results in a higher density of cross-linking.[28,29] Flammability has been a major issue in the polyurethane industry for certain applications such as polyurethane-based memory foams as they are highly combustible and produce toxic chemicals. Therefore, many efforts have been made to improve the thermal combustion properties of polyurethane foams by physically blending additive type flame-retardants[30] or incorporating reactive type flame-retardants, which interact with the polymer during the pyrolysis, into the polymeric network through copolymerization.[31] In general, polyurethanes copolymerized with flame-retardant monomers exhibit improved thermal stability compared to those with additive types since they form robust covalent bonds with urethane linkages. Given the enhanced thermal stability of **1**, we hypothesized **IV** could function as a flame-retardant polyol in this system. The potential competence of **IV** as a flame-retardant monomer was investigated through micro combustion calorimetry (MCC). In a MCC test, the sample is pyrolyzed at a linear heating rate of 1 °C/s in a N_2 atmosphere and the volatiles are premixed with O_2, resulting in a complete combustion of the material.[32] MCC results show a drastically higher char yield for **1** compared to **2**, along with a corresponding decrease in heat of combustion for **1** (Fig. 4.3c). The two-peak heat release rate behavior of **2** is also eliminated, resulting in a single, higher heat release rate peak for **1** (Fig. 4.3d). The increased char yield, along with the decrease in heat of combustion suggest that, at this heating rate, **1** may offer improved condensed phase flame retardancy. However, given the potential dependence of the char yield on the heating rate, this flame retardancy effect should be characterized at higher heating rates that are more representative of realistic fire scenarios. Nevertheless, for applications where the initial heating rate is on the order of **1** °C/s or lower, **1** shows promising performance as a char-forming fire retardant material.

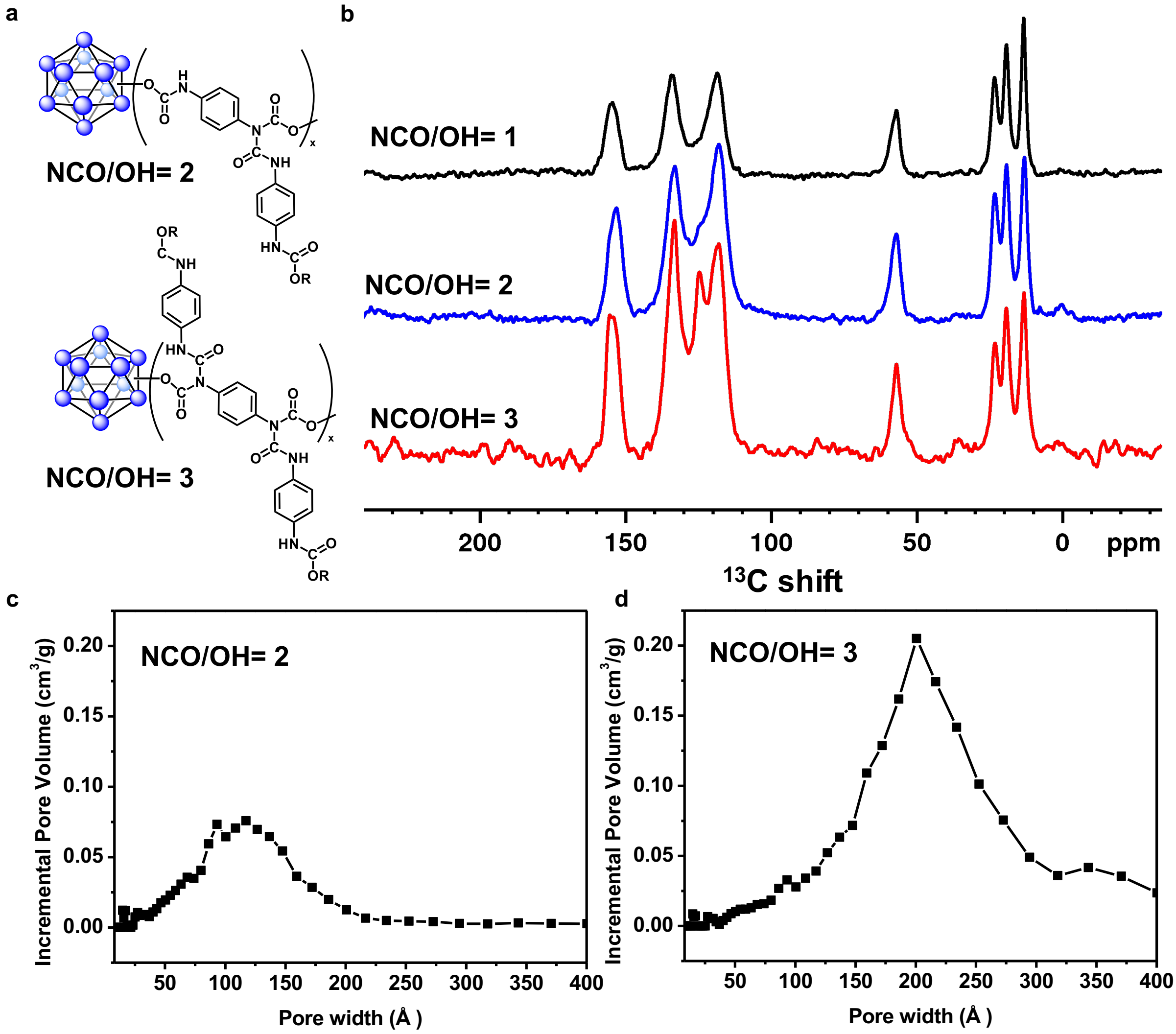

Figure 4.4 (a) Branched polymers which possess allophanate linkages, (b) Solid-state 1D single pulse ^{13}C MAS NMR of the branched polymers. (c,d) Pore size distribution of the branched polyurethanes shown in (a).

Finally, in the synthesis of polyurethanes, the presence of excess isocyanates can create allophanate linkages in which the newly formed secondary amine of a urethane linkage reacts with an isocyanate substrate (ESI†).[33] We envisioned the surface area and the pore size of the resulting polymer could be tailored by introducing allophanates into the network as they form branched structures. Accordingly, we prepared three different cross-linked polyurethanes by employing various ratios of isocyanates to polyol hydroxyl groups (NCO/OH) (Fig. 4.4a). The formation of allophanate linkages was confirmed through ^{13}C MAS SSNMR. As more diisocyanates are employed, the shoulder around 120 ppm appears more prominent, indicating an increased amount of aromatic carbon close to the allophanate linkages (Fig. 4.4b and ESI†). Moreover, the gradual increase in the intensity of the C=O carbon signal (154 ppm) from NCO/OH=1 to 3 further suggests the formation of allophanate linkages. Indeed, the material containing more allophanate groups, which possesses more branched structures with fewer cross-linkers, exhibits increased surface area and pore sizes (Fig. 4.4c,d and ESI†). This modification of the polyurethane structure demonstrates the value of **IV** to generate polyurethane materials that possess porous structures and to potentially alter their thermal properties (ESI†).[34]

Conclusion

In summary, we have reported a new class of cross-linked porous polyurethanes utilizing polyhedral boron clusters as an inorganic polyol equivalent. The incorporation of these building blocks into the polyurethane results in a porous morphology and enhanced thermal stability of the material compared to analogous polymers produced from carbon-based polyols. These results highlight the value of the molecular cross-linking with the dodecaborate cluster as a novel and effective strategy to alter the chemical and physical properties of polymeric materials. This work further showcases how molecular main group chemistry can be harnessed to improve the properties of polymeric materials.[35-45]

References

1. M. Akiba and A. S. Hashim, *Prog. Polym. Sci.*, 1997, **22**, 475−521.
2. J. Maitra and V. K. Shuka, *J. Polym. Sci.*, 2014, **4**, 25−31.
3. T. G. Fox and S. Loshaek, *J. Polym. Sci.*, 1955, **15**, 371−390.
4. E. A. Kamoun, X. Chen, M. S. M. Eldin and E-R. S. Kenawy, *Arab. J. Chem.*, 2015, **8**, 1−14.
5. P. Wang, H. Xing, D. Xia and X. Ji, *Chem. Commun.*, 2015, **51**, 17431−17434.
6. L. Tan and B. Tan, *Chem. Soc. Rev.*, 2017, **46**, 3322−3356.
7. R. Ramachandran, D. Jung and A. M. Spokoyny, *NPG Asia Mater.*, https://doi.org/10.1038/s41427-019-0119-9
8. J. O. Akindoyo, M. D. H. Beg, S. Ghazali, M. R. Islam, N. Jeyaratnam and A. R. Yuvaraj, *RSC Adv.*, 2016, **6**, 114453−114482.
9. R. B. Seymour and G. B. Káuffman, *J. Chem. Educ., 1992*, **69**, 909−910.
10. D. Chattopadhyay and K. Raju, *Prog. Polym. Sci.*, 2007, **32**, 352–418.
11. M. Heinen, A. E. Gerbase and C. L. Petzhold, *Polym. Degrad. Stab.*, 2014, **108**, 76–86.
12. P. Singhal, J. N. Rodriguez, W. Small, S. Eagleston, J. V. de Water, D. J. Maitland and T. S. Wilson, *J. Polym. Sci. B*, 2012, **50**, 724–737.
13. S. Oprea, *J. Am. Oil Chem. Soc.*, 2010, **87**, 313–320.
14. L. Zhang, M. Zhang, L Hu and Y. Zhou, *Ind Crops Prod.*, 2014, **52**, 380−388.
15. M. Fleischer, H. Blattmann and R. Mulhaupt, *Green Chem.*, 2013, **15**, 934−942.
16. T. Peymann, C. B. Knobler, S. I. Khan and M. F. Hawthorne, *J. Am. Chem. Soc.*, 2001, **123**, 2182–2185.
17. D. Jung, L. M. A. Saleh, Z. J. Berkson, M. F. El-Kady, J. Y. Hwang, N. Mohamed, A. I. Wixtrom, E. Titarenko, Y. Shao, K. McCarthy, J. Guo, I. B. Martini, S. Kraemer, E. C. Wegener, P. Saint-Cricq, B. Ruehle, R. R. Langeslay, M. Delferro, J. L. Brosmer, C. H.

Hendon, M. Gallagher-Jones, J. Rodriguez, K. W. Chapman, J. T. Miller, X. Duan, R. B. Kaner, J. I. Zink, B. F. Chmelka and A. M. Spokoyny, *Nat. Mater.*, 2018, **17**, 341–348.

18. A. I. Wixtrom, Y. Shao, D. Jung, C. W. Machan, S. N. Kevork, E. A. Qian, J. C. Axtell, S. I Khan, C. P. Kubiak and A. M. Spokoyny, *Inorg. Chem. Front.*, 2016, **3**, 711–717.
19. M. S. Messina, J. C. Axtell, Y. Wang, P. Chong, A. I. Wixtrom, K. O. Kirlikovali, B. M. Upton, B. M. Hunter, O. S. Shafaat, S. I. Khan, J. R. Winkler, H. B. Fray, A. N. Alexandrova, H. D. Maynard and A. M. Spokoyny, *J. Am. Chem. Soc.* 2016, **138**, 6952–6955.
20. K. Su and L. G. Sneddon, *Chem. Mater.,* 1993, **5**, 1659–1668.
21. R. Núñez, I. Romero, F. Teixidor and C. Viñas *Chem. Soc. Rev.,* 2016, **45**, 5147–5173.
22. A. M. Spokoyny, *Pure Appl. Chem.,* 2013, **85**, 903–919.
23. A. R. Pitochelli and M. F.Hawthorne, *J. Am. Chem. Soc*., 1960, **82**, 3228−3229.
24. J. C. Axtell, L. M. A. Saleh, E. A. Qian, A. I. Wixtrom and A. M. Spokoyny, *Inorg. Chem*., 2018, **57**, 2333−2350.
25. D. Rosu, L. Rosu and C. N. Cascaval, *Polym. Degrad. Stabil.,* 2009, **94**, 591–596.
26. A. P. Nelson, O. K. Farha, K. L. Mulfort and J. T. Hupp, *J. Am. Chem. Soc*., 2009, **131**, 458–460.
27. W. P. Yang, E. W. Macosko and S. T. Wellinghoff, *Polymer*, 1986, **27**, 1235–1240.
28. T. Gupta and B. Adhikari, *Thermochim. Acta,* 2003, **402**, 169–181.
29. M. L. Matuszak and K. C. Frisch, J. *Polym. Sci. Polym. Chem. Ed*., 1973, **11**, 637–648.
30. M. –J. Chen, X. Wang, M. –C. Tao, X. –Y, Liu, Z. –G, Liu, Y. Zhang, C. –S. Zhao and J. –S. Wang, *Polym. Degrad. Stabil.,* 2018, **154**, 312–322.
31. R. Yang, W. Hu, L. Xu, Y. Song and J. Li, *Polym. Degrad. Stabil.,* 2015, **122**, 102–109.
32. F. Raffan-Montoya, S. I. Stoliarov, S. Levchik and Eden, E. *Polym. Degrad. Stab.* 2018, **151**, 12−24.
33. A. Lapprand, F. Boisson, F. Delolme, F. Méchín and J. –P. Pascault, *Polym. Degrad. Stabil.*,

2005, **90**, 363–373.

34. R. Pirard, A. Rigacci, J. C. Maréchal, D. Quenard, B. Chevalier, P. Achard and J. P. Pirarda, *Polymer*, 2003, **44**, 4881−4887.
35. I. Manners, *J. Polym. Sci. A: Polym. Chem.*, 2002, **40**, 179–191.
36. J. D. Lichtenhan, Y. A. Otonari and M. J. Carr, *Macromolecules*, 1995, **28**, 8435−8437.
37. F. Vidal and F. Jäkle, *Angew. Chem. Int. Ed.*, 2019, **58**, 5846−5870.
38. B. P. Dash, R. Satapathy, J. A. Maguire and N. S. Hosmane, *New J. Chem.*, 2011, **35**, 1955−1972.
39. S. P. Fisher, A. W. Tomich, S. O. Lovera, J. F. Kleinsasser, J. Guo, M. J. Asay, H. Nelson and V. Lavallo, *Chem. Rev.,* DOI: 10.1021/acs.chemrev.8b00551
40. Y. -S. Bae, O. K. Farha, A. M. Spokoyny, C. A. Mirkin, J. T. Hubb and R. Q. Snurr, *Chem. Commun.*, 2008, 4135−4137.
41. A. A. Jahnke and D. S. Seferos, *Macromol. Rapid Commun.*, 2011, **32**, 943−951.
42. Y. Zhang, L. Yang, L. Wang, S. Duttwyler and H. Xing, *Angew. Chem. Int. Ed.*, https://doi.org/10.1002/anie.201903600
43. M. A. Fox and K. Wade, *J. Mater. Chem.*, 2002, **12**, 1301−1306.
44. K. Kokado, Y. Tokoro and Y. Chujo, *Macromolecules*, 2009, **42**, 2925−2930.
45. W. –M. Wan, A. W. Baggett, F. Cheng, H. Lin, S. –Y. Liu and F. Jäkle, *Chem. Commun.*, 2016, **52**, 13616–13619

SUPPORTING INFORMATION

General Considerations

Dry-box manipulations were carried out under an atmosphere of dinitrogen in a Vacuum Atmospheres NexGen dry-box. Acetonitrile was dried prior to use by sparging with argon, and then loaded on a SciMatCo Solvent Purification System. Acetonitrile was then collected and stored over activated 4 Å molecular sieves in a dry-box under dinitrogen atmosphere.

Materials

Deuterated solvents were purchased from Cambridge Isotope Laboratories and used as received. The following chemicals were purchased from commercial vendors: 1,4-phenylene diisocyanate (Sigma Aldrich), pentaerythritol (Sigma Aldrich), *p*-tolyl isocyanate (Oakwood). Cesium and $[N^{n}Bu_4]^+$ salts of $[B_{12}(OH)_{12}]^{2-}$ were synthesized by previously reported methods.[1]

Microwave synthesis

Microwave reactions were carried out using a CEM Discover SP microwave synthesis reactor. 10 ml reaction vials were used for all reactions and sealed with silicone/PTFE caps. Flea micro PTFE-coated stir bars were used in the vials with magnetic stirring set to high and 15 seconds of premixing prior to the temperature ramping. All microwave reactions were carried out at 100-120 °C with the pressure release limit set to 250 psi (no reactions exceeded this limit to trigger venting) and the maximum wattage set to 250W.

Synthesis of non-cross-linked urethanes

The preparation of the microwave reaction was performed in an inert atmosphere dry-box. In a 10 ml glass microwave vial, *p*-tolyl isocyanate (244 mg, 1.83 mmol) in acetonitrile (1 ml) was added to a stirring suspension of $[N^{n}Bu_4]_2[B_{12}(OH)_{12}]$ (25 mg, 0.0305 mmol) in acetonitrile

(0.5 ml). The reaction vial was sealed with a PTFE/silicone cap and then brought outside of the dry-box. The mixture was heated at 100 °C with stirring in the microwave for 2 hours. The excess acetonitrile was removed by rotary evaporation and the excess starting reagents were removed through a slurry-packed silica gel column with 3:1 (v/v) hexane:ethyl acetate. The excess solvent was evaporated by rotary evaporation, the residue was dried under high vacuum.

Synthesis of 1

The preparation of the microwave reaction was performed in an inert atmosphere dry-box. In a 10 ml glass microwave vial, 1,4-phenylene diisocyanate (59 mg, 0.366 mmol) in acetonitrile (1 ml) was added to a stirring suspension of $[N^{n}Bu_4][B_{12}(OH)_{12}]$ (50 mg, 0.0611 mmol) in acetonitrile (0.5 ml). The reaction vial was sealed with a PTFE/silicone cap and then brought outside of the dry-box. The mixture was heated at 120 °C with stirring in the microwave for 2 hours. The reaction mixture was transferred to a 20 ml glass scintillation vial. The NCO/OH ratio of 2 and 3 were used to produce allophanate linkages.

Note: The gelation time can be shortened by using a 1,4-diazabicyclo[2.2.2]octane (DABCO) as a catalyst without affecting the structure and thermal stability of the product (Fig. S6, S7).

Synthesis of 2

The preparation of the microwave reaction was performed in an inert atmosphere dry-box. In a 10 ml glass microwave vial, 1,4-phenylene diisocyanate (118 mg, 0.734 mmol) in acetonitrile (2 ml) was added to a stirring suspension of pentaerythritol (50 mg, 0.367) in acetonitrile (0.5 ml). The reaction vial was sealed with a PTFE/silicone cap and then brought outside of the dry-box. The mixture was heated at 120 °C with stirring in the microwave for 2 hours. The product was washed with ethanol and vacuum dried on a lyophilizer.

Instrumentation

^1H solution NMR spectra were recorded in $(CD_3)_2CO$-*d6* on AV 400 spectrometers in ambient conditions and referenced internally to residual solvent resonances in deuterated solvents (δ 2.05 for $(CD_3)_2CO$-*d6*). ^{13}C NMR spectra were obtained on AV 500 spectrometers with a cryoprobe.

Infrared (IR) spectra were obtained with a PerkinElmer Spectrum One instrument equipped with a universal ATR assembly.

Scanning electron microscopy (SEM) images were obtained with a field-emission SEM (JEOL JSM 6700F).

Thermogravimetric analysis (TGA) was carried out on a PerkinElmer Pyris Diamond TG/DTA under a constant flow of Argon (200 mL/min). Samples were heated in alumina oxide trays from 25 °C to 1000 °C at 10 °C/min.

^{11}B and ^{13}C solid-state magic angle spinning (MAS) nuclear magnetic resonance (NMR) spectra were obtained on a 600 MHz (14.1 T) Bruker AVANCE III HD spectrometer using a 3.2 mm HXY MAS probe. The MAS frequency used was 20 kHz for ^{11}B and 18 kHz for ^{13}C. The ^{11}B background signal from the MAS probe was suppressed using the EASY sequence.[2] The ^{11}B chemical shift was indirectly referenced to $BF_3O(CH_2CH_3)_2$ in $CDCl_3$ by using $Cs_2[B_{12}(OH)_{12}]$ (δ=-17.4 ppm).[3] The RF field for the ^{11}B central transition selective pulse was 66 kHz.

Mass spectrometry data was acquired using a Thermo Scientific Q-Exactive Plus instrument with a quadrupole mass filer and Orbitrap mass analyzer.

Supercritical CO_2 activation was carried out on as Tousimis^{TM} Samdri® PVT-30 critical point dryer. The solvent contained in the polymer gel was firstly exchanged with ethanol overnight and then with liquid CO_2 for 10 hours. Then, the sample was taken beyond the critical point of CO_2 (T= 31 °C; P= 1071 psi) and slowly vented overnight.

N_2 isotherms were measured at 77 K on a micromeritics Tristar after activation at 40 °C under vacuum 4 h.

Micro Combustion Calorimetry (MCC)

1 and **2** were tested using Micro Combustion Calorimetry (MCC).[4] In MCC, a 3-5 mg sample is pyrolyzed under anaerobic conditions (N_2 atmosphere). The volatiles are then premixed with O_2 and the N_2-fuel-O_2 mixture enters an annular reactor where the fuel is fully oxidized (complete combustion products). Using O_2 consumption calorimetry methods,[5] the heat release rate is obtained. Integration of the heat release rate curve provides the heat of combustion of the sample. The values for the heat of combustion were normalized by the initial sample mass. Solid residue is measured in order to provide char yield data. For the current work, duplicate samples of **1** and **2** were tested. In MCC, the sample was heated at the standard heating rate of 1 °C/s, and the combustor temperature was 925 °C.

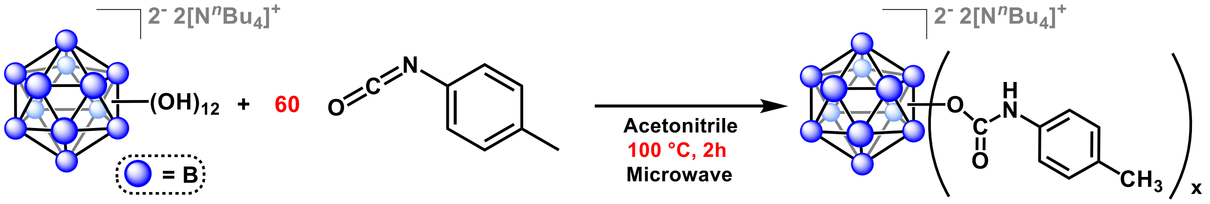

Figure S1. Synthetic route to produce non-cross-linked urethane linkages using $[N^{n}Bu_4]_2[B_{12}(OH)_{12}]$ and *p*-toly isocyanate.

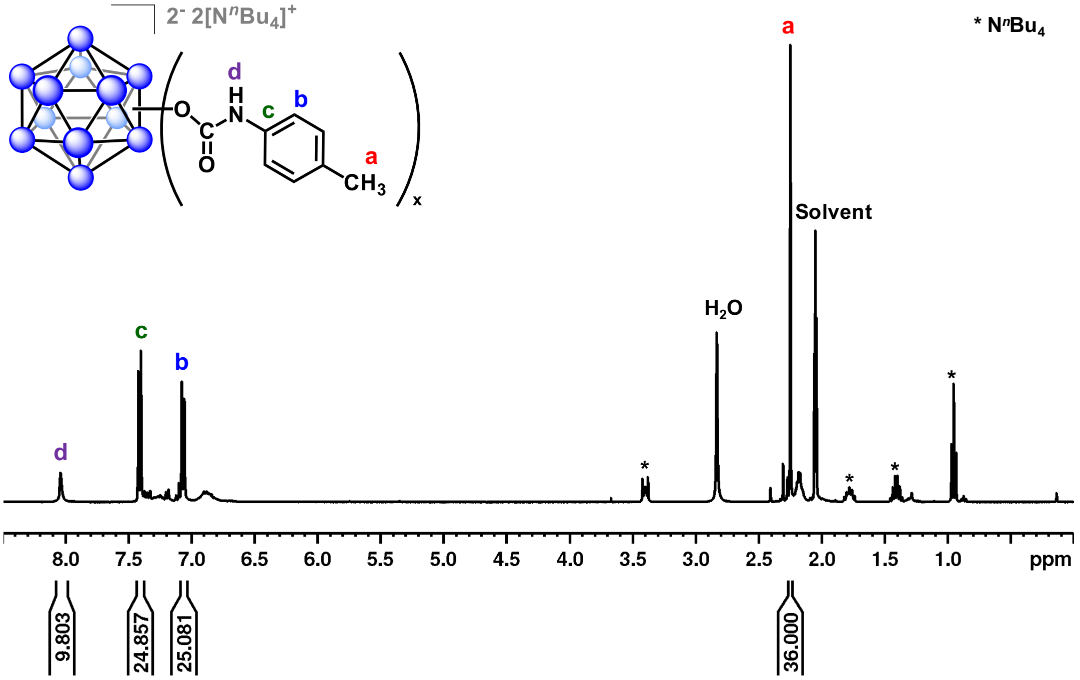

Figure S2. ^{1}H NMR spectrum of the test reaction of *p*-tolyl isocyanate with $[N^{n}Bu_4]_2[B_{12}(OH)_{12}]$ in $(CD_3)_2CO$. Peaks associated with the product are observed, indicating formation of urethane linkages.

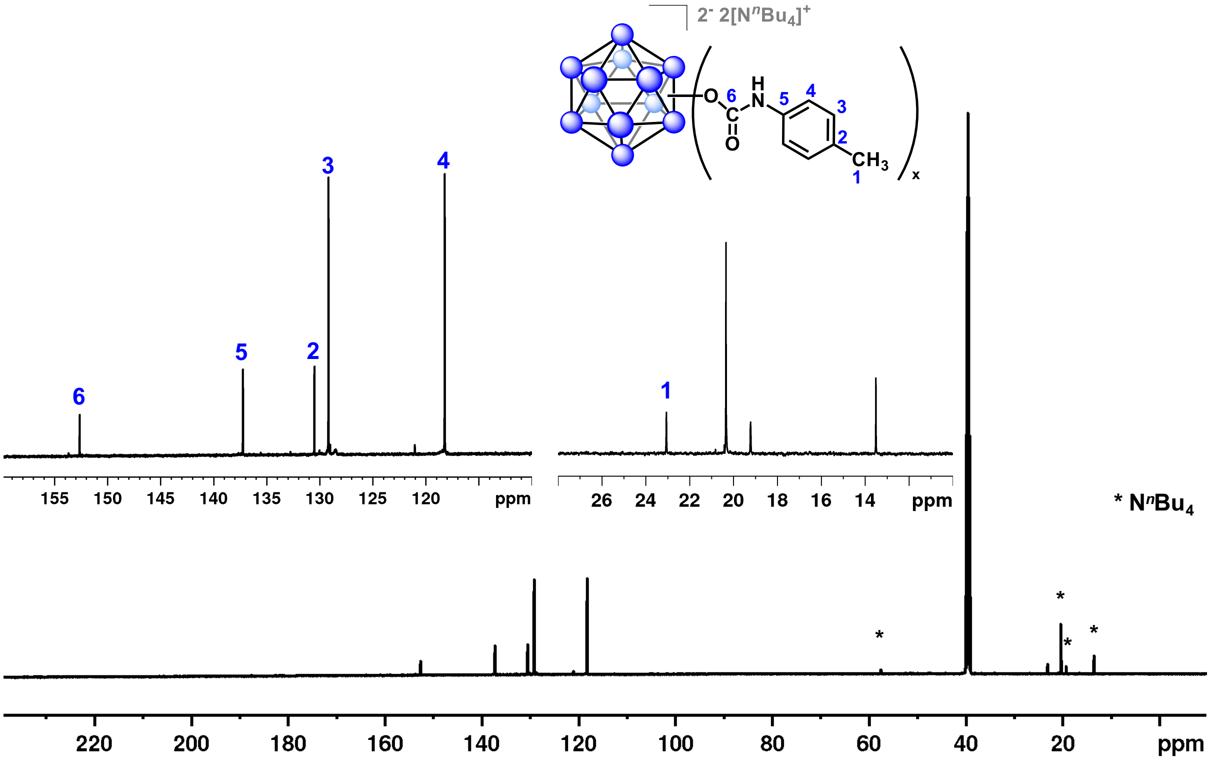

Figure S3. ^{13}C NMR spectrum of the test reaction of *p*-tolyl isocyanate with $[N^nBu_4]_2[B_{12}(OH)_{12}]$ in $(CD_3)_2SO$. Peaks associated with the product are observed, indicating formation of urethane linkages.

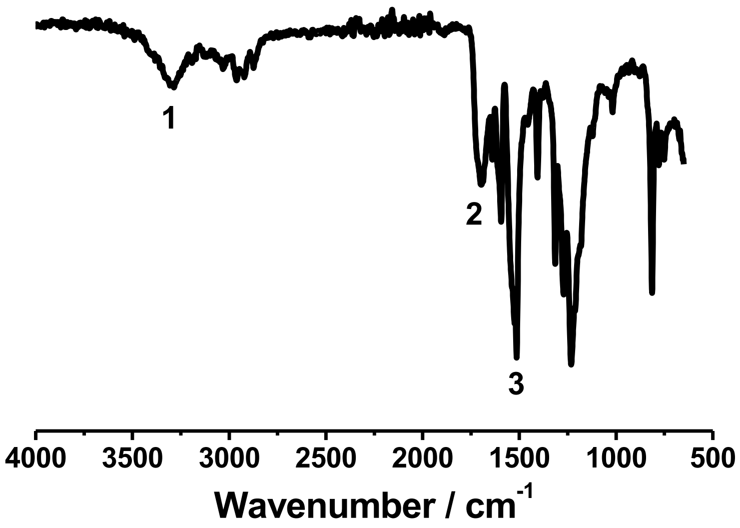

	Functional group	Absorption (cm^{-1})
1	N-H stretching	3286
2	C=O stretching	1699
3	C-N stretch coupled with N-H bending	1517

Figure S4. FT-IR spectrum of the test reaction of *p*-tolyl isocyanate with $[N^{n}Bu_4]_2[B_{12}(OH)_{12}]$

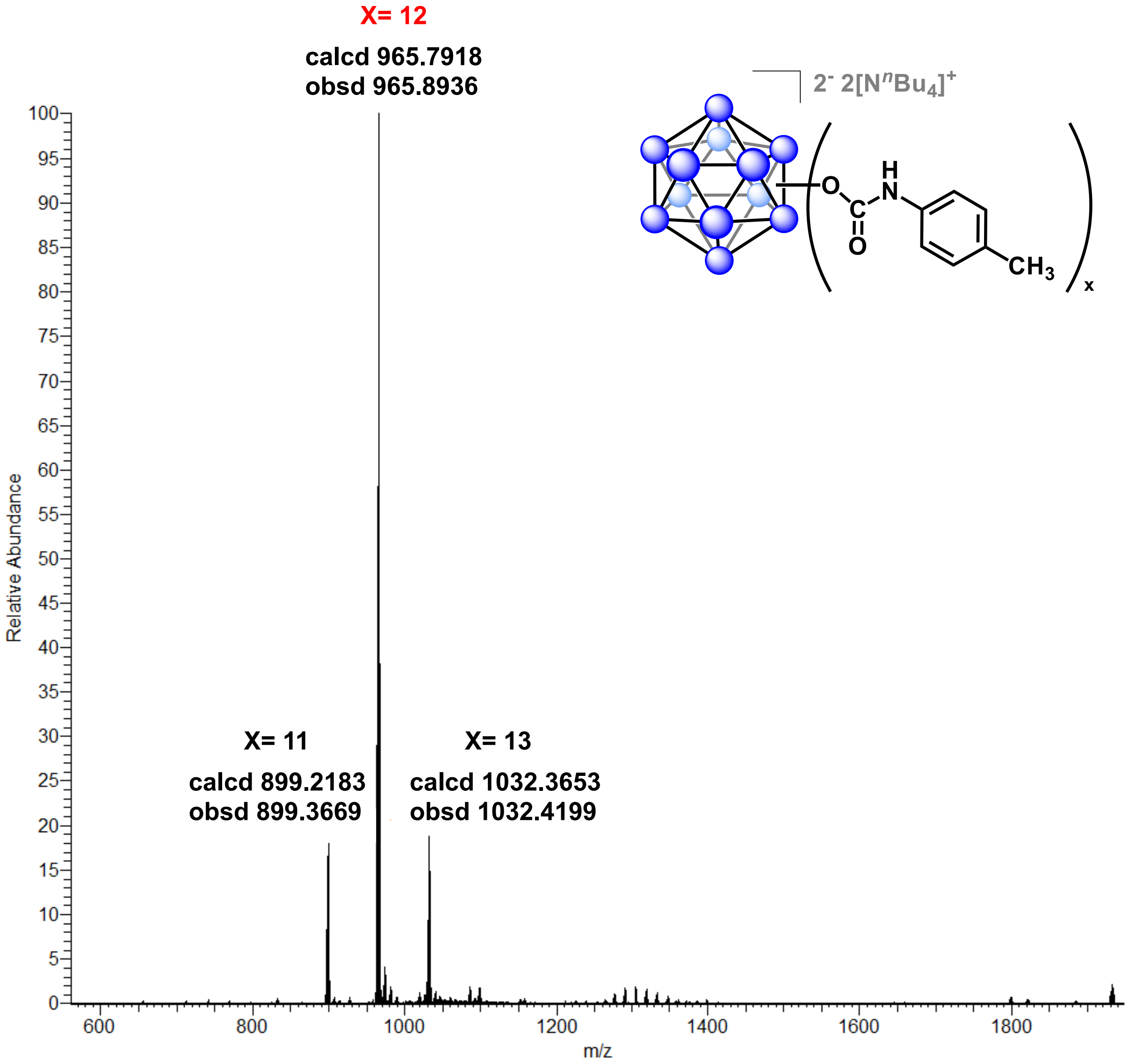

Figure S5. ESI-HRMS of the test reaction of *p*-tolyl isocyanate with $[N^{n}Bu_4]_2[B_{12}(OH)_{12}]$, supporting the complete substitution of $[B_{12}(OH)_{12}]^{2-}$ clusters. The over-substituted compound (X=13) represents the presence of an allophanate linkage in the product which arises from the reaction of the amine of a urethane linkage with an excess isocyanate substrate.

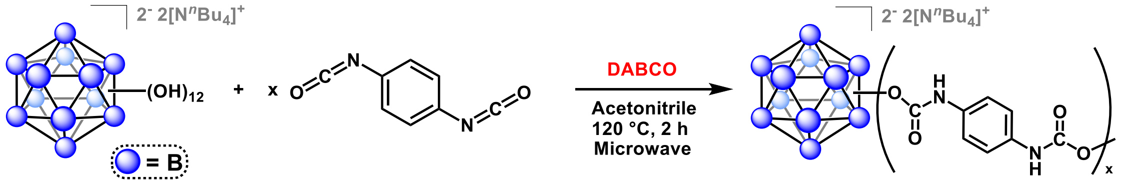

	Catalyst	Gelation time
Trial 1	None	24 h
Trial 2	5.6 mg DABCO	2 h

Figure S6. Synthetic route to produce the cross-linked polyurethane materials using 1,4-diazabicyclo [2.2.2] octane (DABCO) as a catalyst.

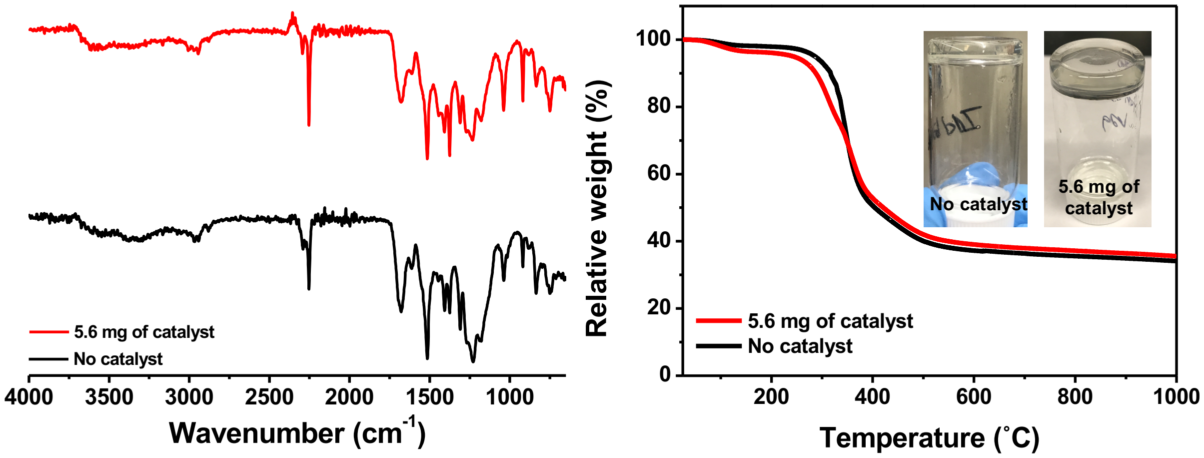

Figure S7. (a) FT-IR spectra and (b) TGA results of the polyurethane gel depending on the use of catalysts. While the use of the catalyst affects the gelation time, there was no noticeable change in the structure and the thermal properties of the cross-linked polyurethane gels.

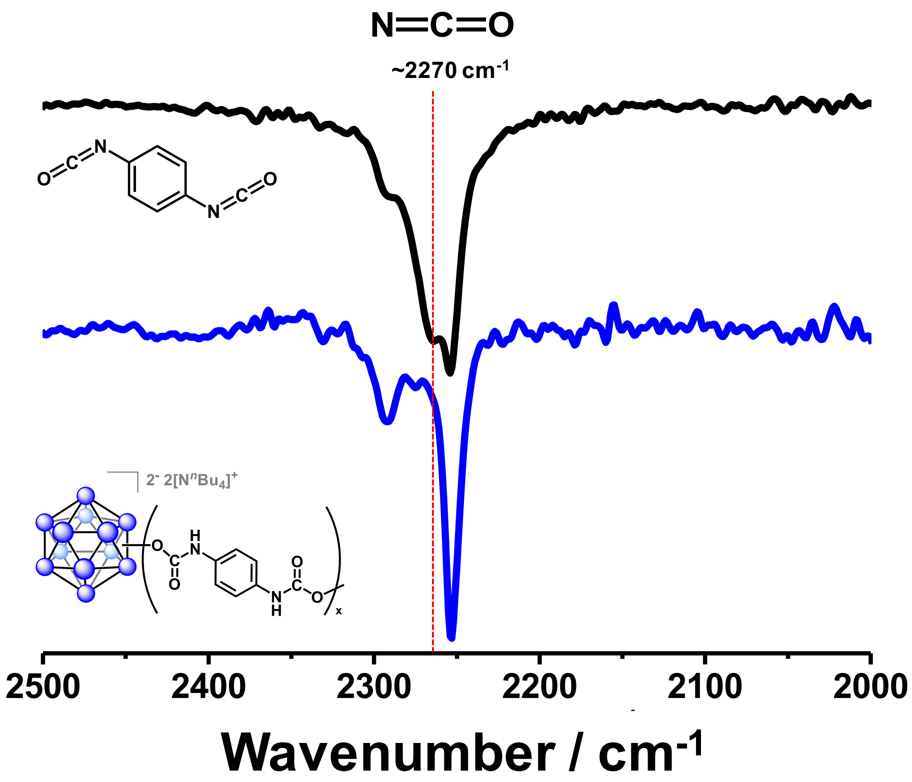

Figure S8. FT-IR spectra of **1** and 1,4-phenylene diisocyanate in acetonitrile. The absence of the peak at 2270 cm^{-1}, which corresponds to the free isocyanates, indicates the complete reaction of $[N^nBu_4]_2[B_{12}(OH)_{12}]$ with 1,4-phenylene diisocyanate. The sharp peak at 2240 cm^{-1} arises from the solvent, CH_3CN.

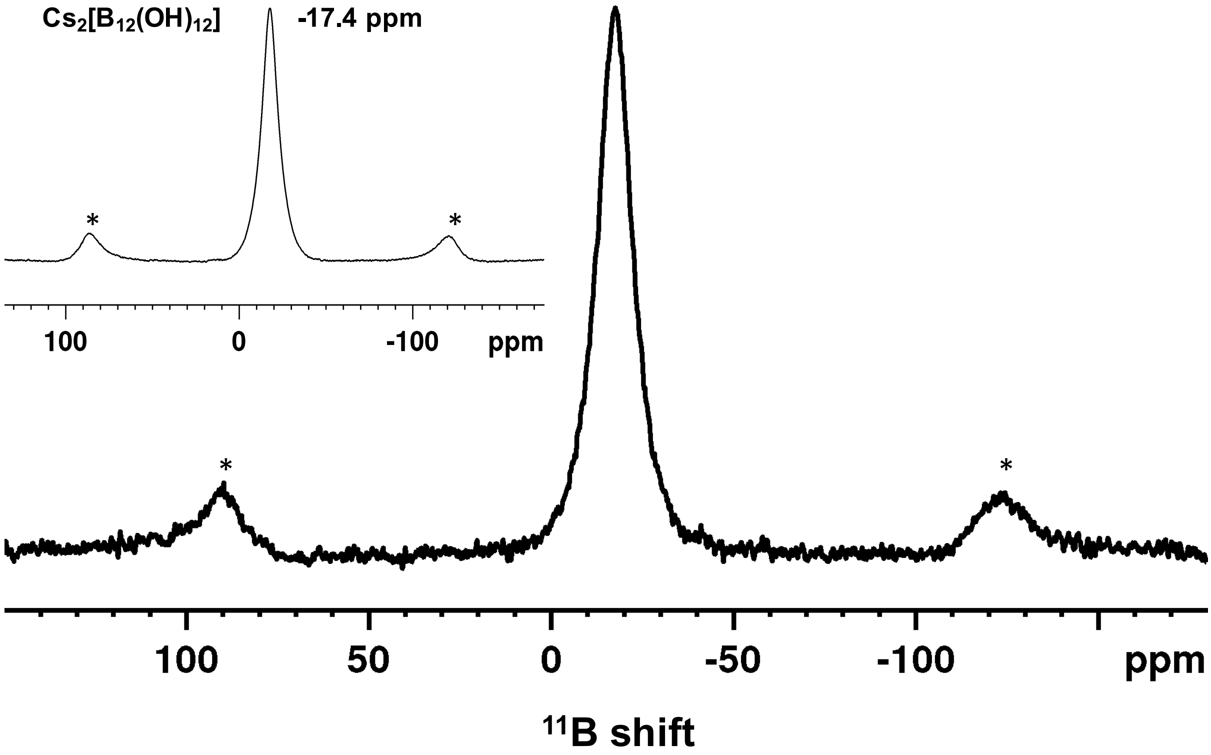

Figure S9. Solid-state 1D single-pulse ^{11}B MAS NMR of **1** and reference $Cs_2[B_{12}(OH)_{12}]$ (inset).

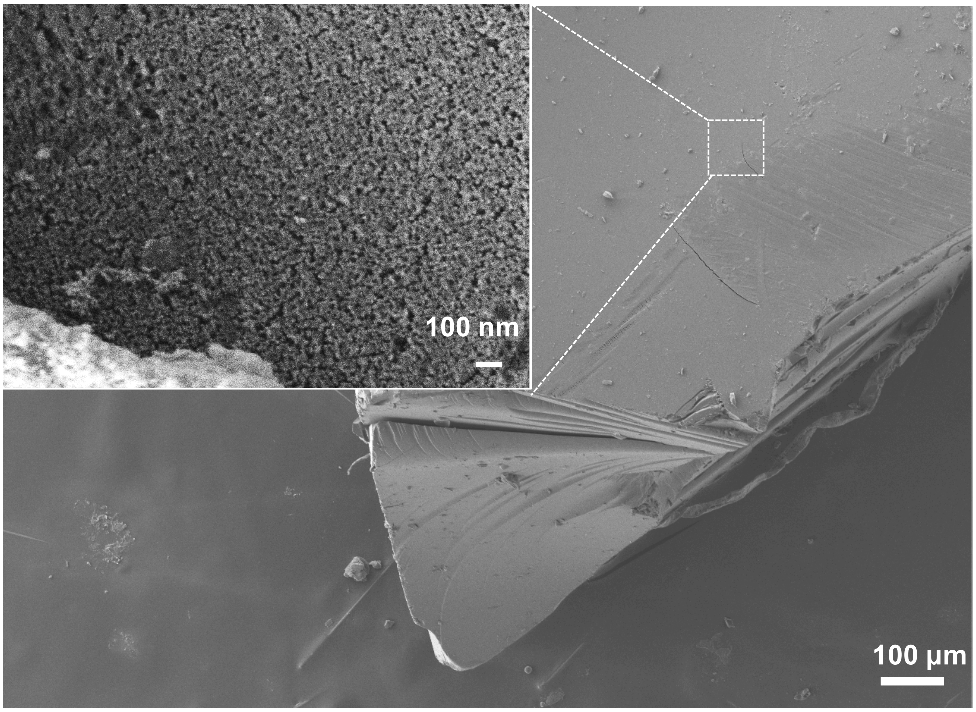

Figure S10. SEM image of **1** after supercritical CO_2 activation.

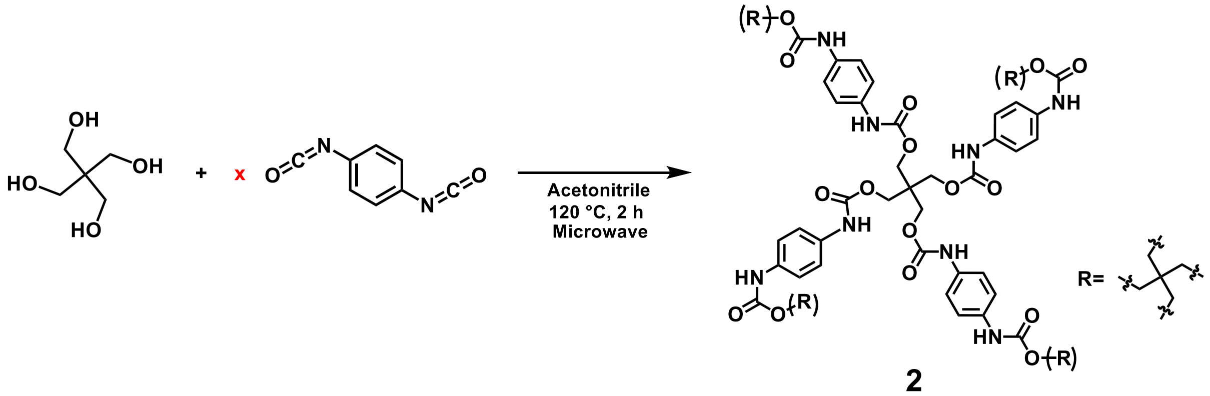

2

Figure S11. Synthetic route to produce **2** utilizing pentaerythritol as a cross-linker.

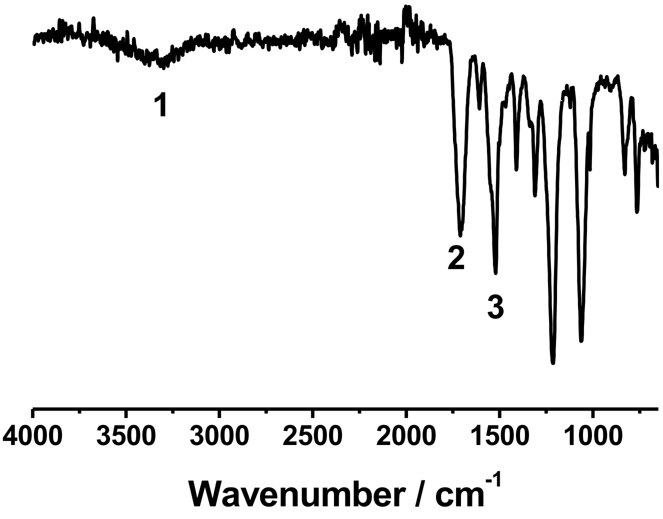

	Functional group	Absorption (cm^{-1})
1	N-H stretching	3300
2	C=O stretching	1698
3	C-N stretch coupled with N-H bending	1520

Figure S12. FT-IR spectrum of **2**, confirming the formation of the urethane linkage in **2**.

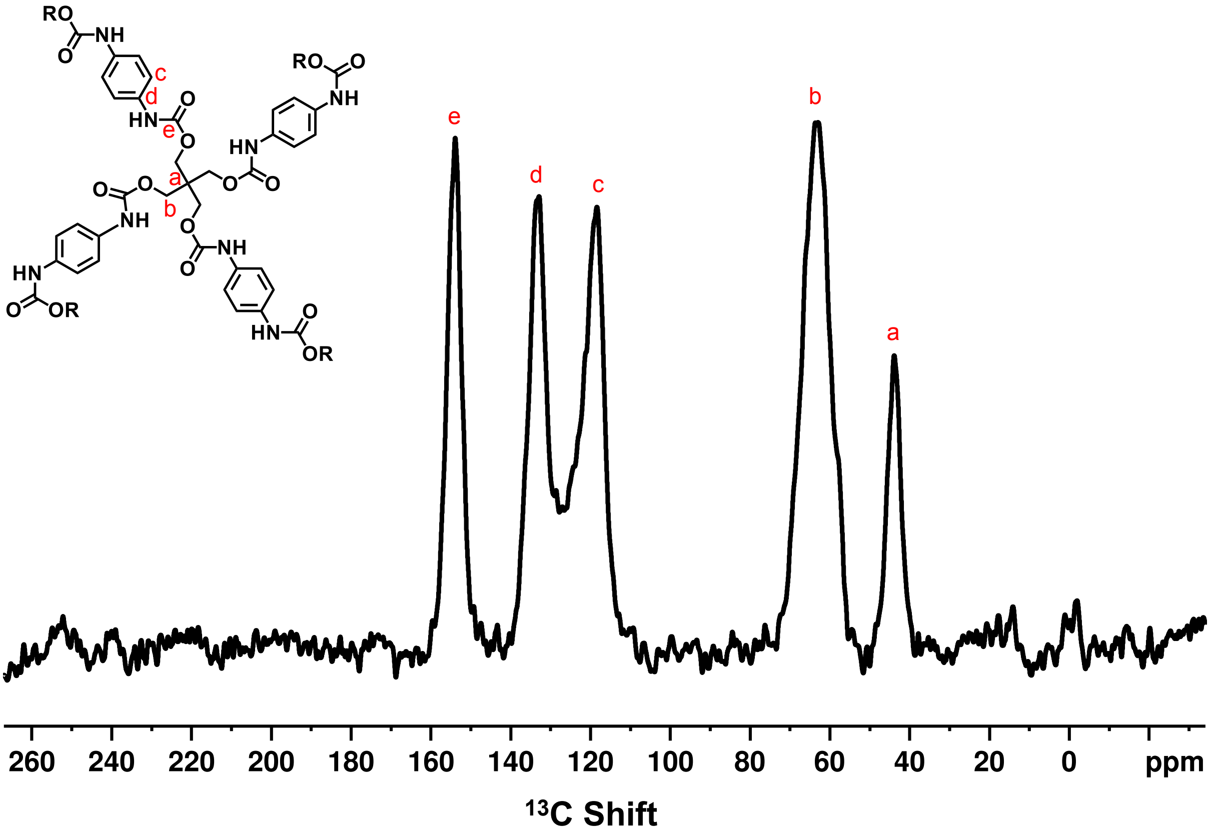

Figure S13. Solid-state 1D single-pulse ^{13}C NMR of **2**. Peaks associated with the product can be observed.

Samples	**$T_{d\ 5\%}$(°C)**	**$T_{d\ max}$ (°C)**	**Residue (%)**
1	286	346	35.0
2	218	303	2.9

Table 1. TGA results of **1** and **2** at the heating rate of 10 °C/min in Ar. $T_{d5\%}$ denotes the temperature at 5 % weight loss; T_{dmax} refers to the temperature at the maximum decomposition; residue % denotes the weight of the char residue at 800 °C.

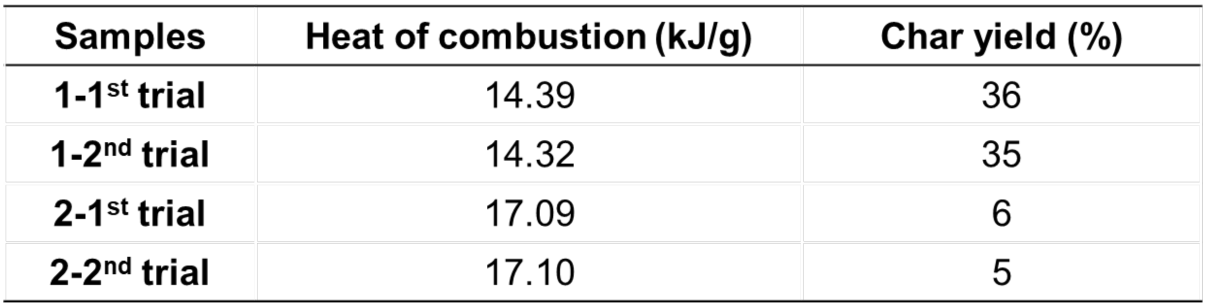

Samples	**Heat of combustion (kJ/g)**	**Char yield (%)**
1-1st trial	14.39	36
1-2nd trial	14.32	35
2-1st trial	17.09	6
2-2nd trial	17.10	5

Table 2. Micro combustion calorimetry (MCC) test results. The tests were duplicated.

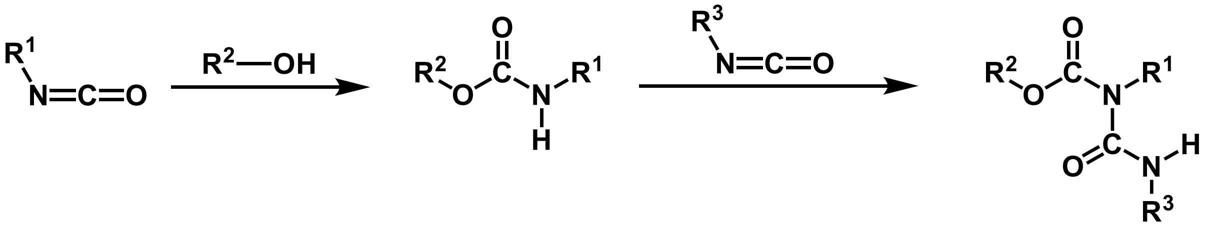

Figure S14. Synthetic route to create allophanate linkages in the polymer network.

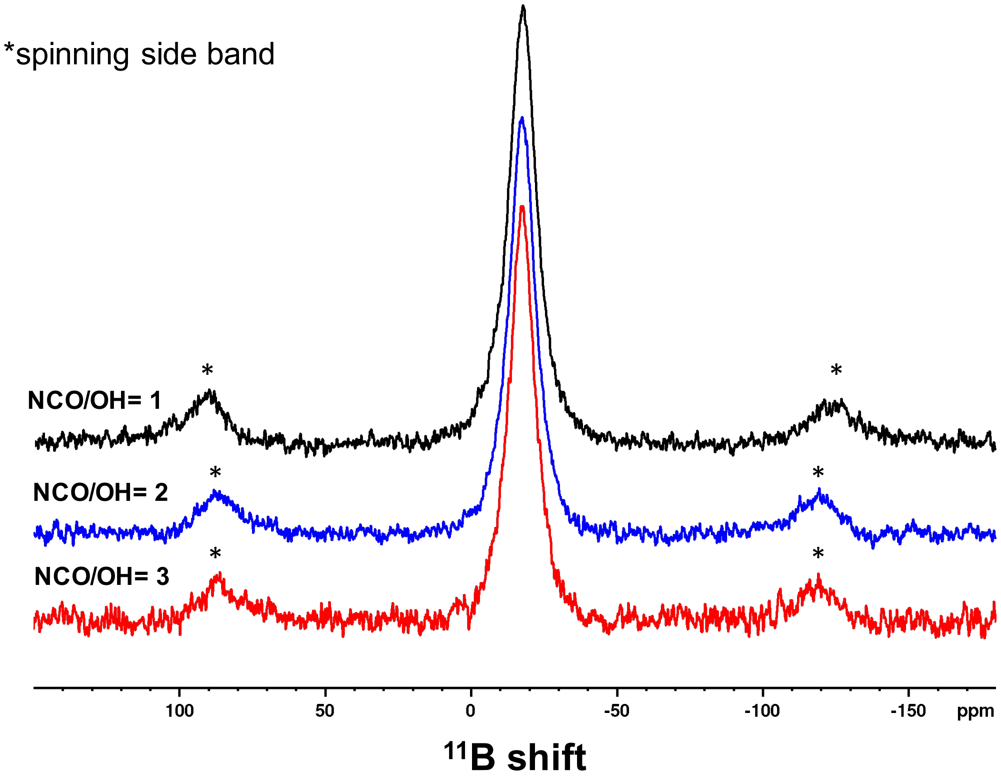

Figure S15. Solid-state 1D single-pulse ^{11}B NMR of the cross-linked polyurethane materials obtained from different ratios of NCO/OH.

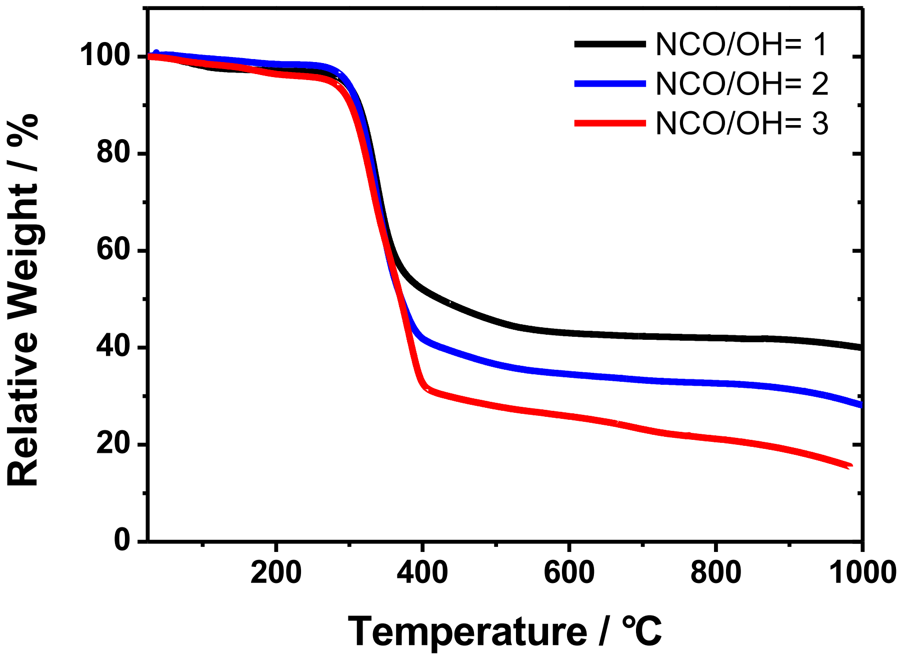

Figure S16. TGA of the cross-linked polyurethane materials obtained from different ratios of NCO/OH.

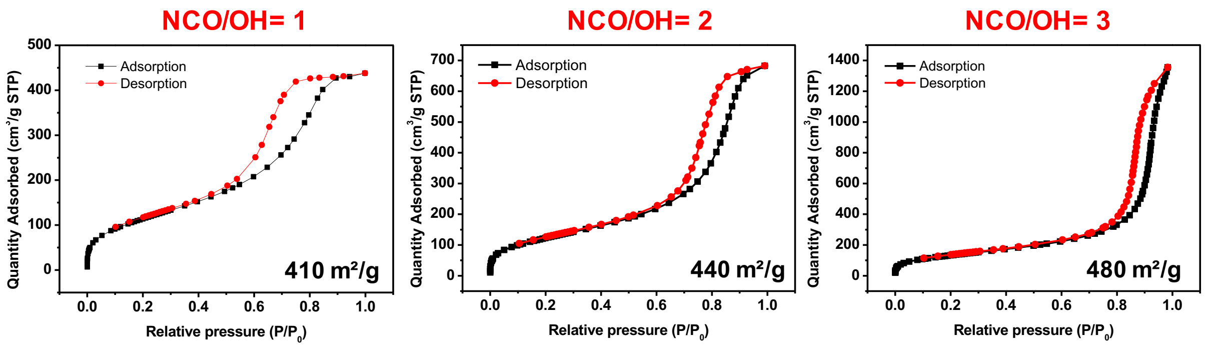

Figure S17. N_2 adsorption and desorption isotherms at 77 K of the cross-linked polyurethane materials obtained from different ratios of NCO/OH.

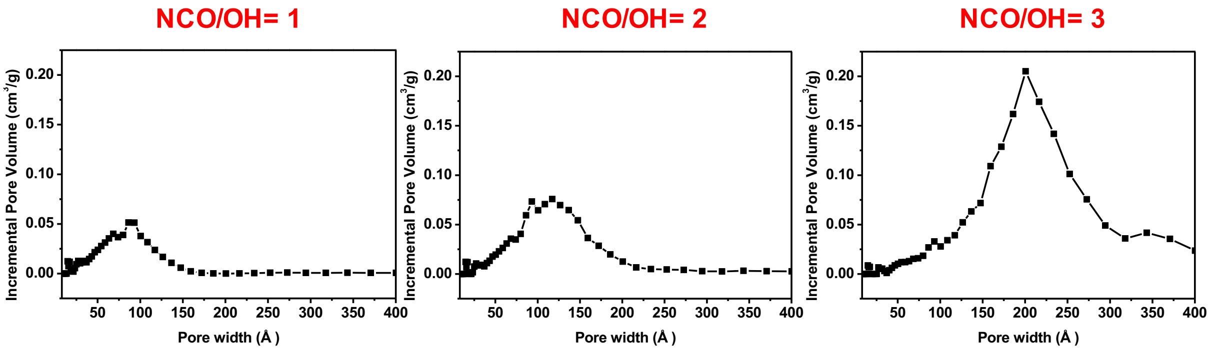

Figure S18. Pore size distribution of the cross-linked polyurethane materials obtained from different ratios of NCO/OH.

References:

1. A. I. Wixtrom, Y. Shao, D. Jung, C. W. Machan, S. N. Kevork, E. A. Qian, J. C. Axtell, S. I Khan, C. P. Kubiak and A. M. Spokoyny, *Inorg. Chem. Front.*, 2016, **3**, 711–717.
2. C. Jaeger and F. Hemmann, *Solid State Nucl. Mag.,* 2014, **57**, 22–28.
3. D. Jung, L. M. A. Saleh, Z. J. Berkson, M. F. El-Kady, J. Y. Hwang, N. Mohamed, A. I. Wixtrom, E. Titarenko, Y. Shao, K. McCarthy, J. Guo, I. B. Martini, S. Kraemer, E. C. Wegener, P. Saint-Cricq, B. Ruehle, R. R. Langeslay, M. Delferro, J. L. Brosmer, C. H. Hendon, M. Gallagher-Jones, J. Rodriguez, K. W. Chapman, J. T. Miller, X. Duan, R. B. Kaner, J. I. Zink, B. F. Chmelka and A. M. Spokoyny, *Nat. Mater.*, 2018, **17**, 341–348.
4. ASTM D7309-13. Standard Test Method for Determining Flammability Characteristics of Plastics and Other Solid Materials Using Microscale Combustion Calorimetry. ASTM International, West Conshohocken, PA 2013.
5. C. Hugett, *Fire Mater.*, 1980, **4**, 61–65.

APPENDIX

METAL SALTS OF PERHYDROXYLATED DODECABORATE CLUSTERS

We explored several redox-active B_{12}-based cluster derivatives for use as noble cathode materials for lithium ion battery. Specifically, we focused on inorganic metal salts perhydroxylated dodecaborate cluster.

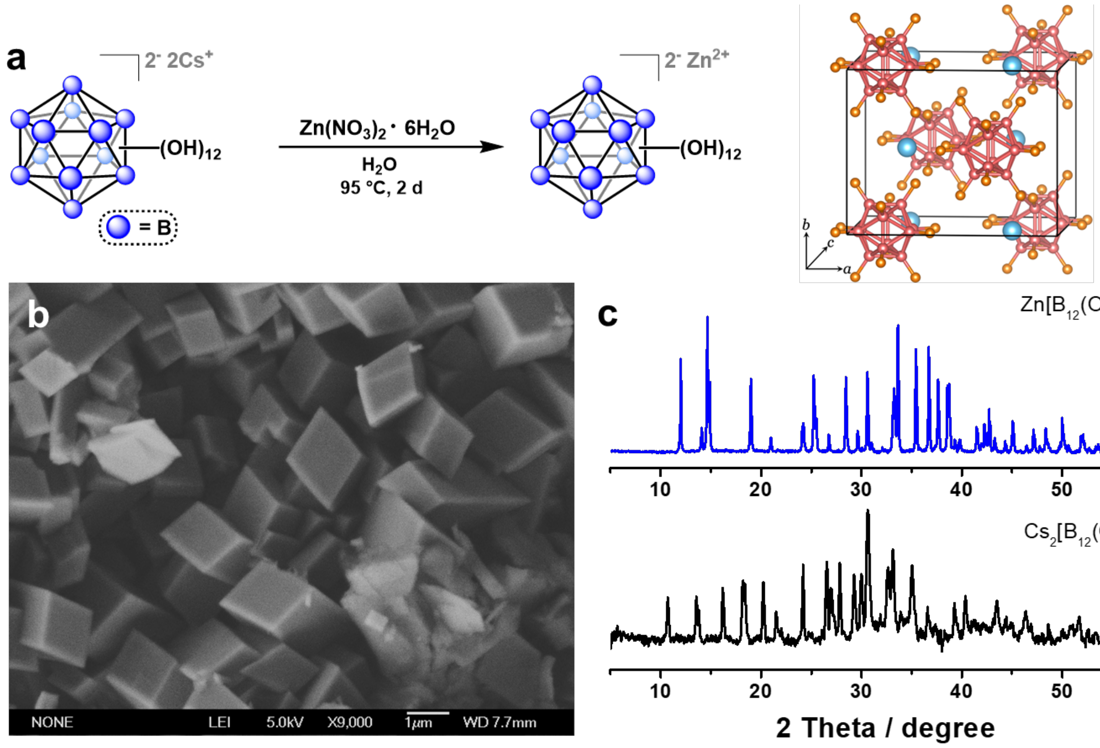

Figure I. (a) Synthetic route toward producing Zn[$B_{12}(OH)_{12}$] salt. SEM (b) and PXRD pattern (c) of Zn[$B_{12}(OH)_{12}$] salt.

Synthesis of Zn[$B_{12}(OH)_{12}$] cluster: In a pyrex tube, $Zn(NO_3)_2$•$6H_2O$ (238 mg, 0.800 mmol) in deionized water (1.5 ml) was added to a suspension of $Cs_2[B_{12}(OH)_{12}]$ (40 mg, 0.0667 mmol) in deionized water (1.5 ml). The reaction tube was heated at 90 °C in an oil bath for 2 days. The product was recovered as white powder and washed with deionized water three times and vacuum dried on a lyophilizer.

Structure determination of $Zn[B_{12}(OH)_{12}]$ cluster:

The refinement of the structure from PXRD data was performed by Emily Schueller in Professor Ram Seshadri group at University of California, Santa Barbara.

An XRD pattern was taken on a ground sample of the $Zn[B_{12}(OH)_{12}]$ compound from 5 to 120° 2θ on an Empyrean diffractometer with Cu-Kα radiation (λ=1.54 Å). The powder pattern was indexed using the EXPO2014 software with the N-TREOR09 indexing algorithm to obtain a unit cell with *P*–1 symmetry. This unit cell was put into TOPAS along with the diffraction data and a Pawley fit was performed to obtain refined cell, background, profile (peak shape), and sample displacement parameters.

These parameters were fixed and information about the atoms was imported into TOPAS. The borane clusters were fixed in shape as rigid bodies with the -OH groups replaced by -F atoms for simplicity, because they have the same X-ray scattering power. The clusters were allowed to rotate and translate, and the Zn atoms were allowed to translate. A simulated annealing algorithm was implemented in TOPAS which varied the atom positions in order to minimize the least squared error from the XRD pattern. When the cell parameters were also allowed to vary, the cell relaxed into monoclinic symmetry. FINDSYM was used on the resulting structure to obtain the new space group, which was monoclinic *C*2/*m*. Simulated annealing was performed on the new monoclinic structure to obtain the best fit to the XRD pattern. Density measurements on the powder in a pycnometer confirmed that the experimental density of 2.27 g/cm^3 was close to the predicted density of 2.10 g/cm^3.

Finally, a Rietveld refinement was performed in order to obtain atomic displacement parameters and statistical information about the quality of the fit. The final structure is monoclinic but pseudo-tetragonal, with β close to 90° and *a* and *c* close in length. Each Zn is coordinated to 3 clusters by 4 bonds.

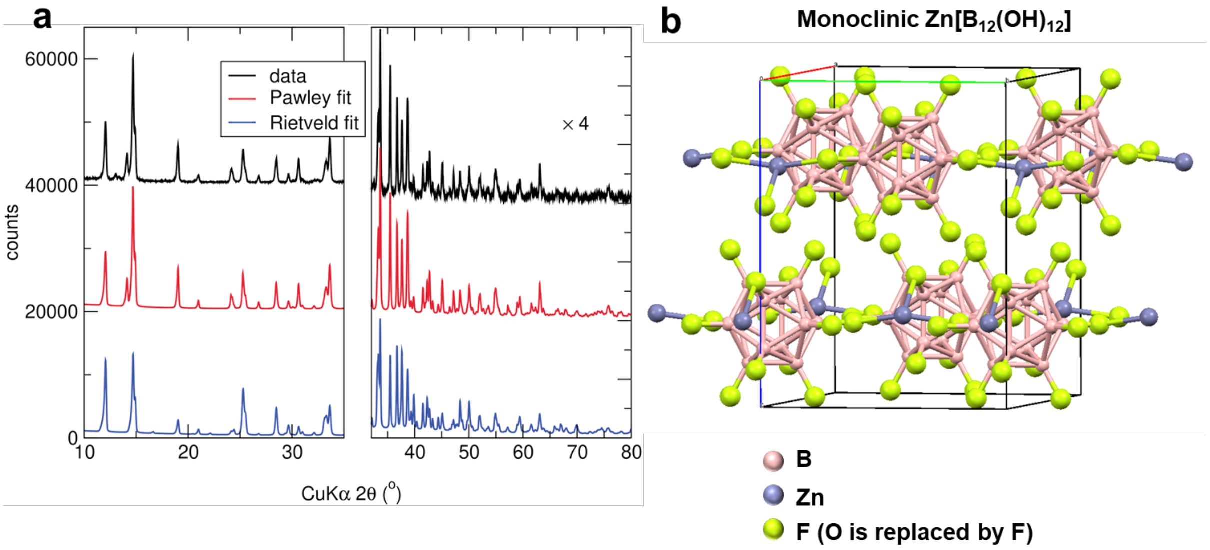

Figure II. (a) Comparison of experimental PXRD data with calculated patterns.

Space group	*C*2/*m*
Lattice parameters (*a*, *b*, *c* (Å), α, β, γ)	11.88, 9.33, 12.05, 90, 90.05, 90
Theoretical density (g/cm^3)	2.10
R_{wp} (%)	25.98
Goodness of fit	6.63
Zn ADP (Å^2)	3.90
B ADP (Å^2)	2.35
F ADP (Å^2)	4.97

Table I. Parameters for the crystal structure of $Zn[B_{12}(OH)_{12}]$ salt.

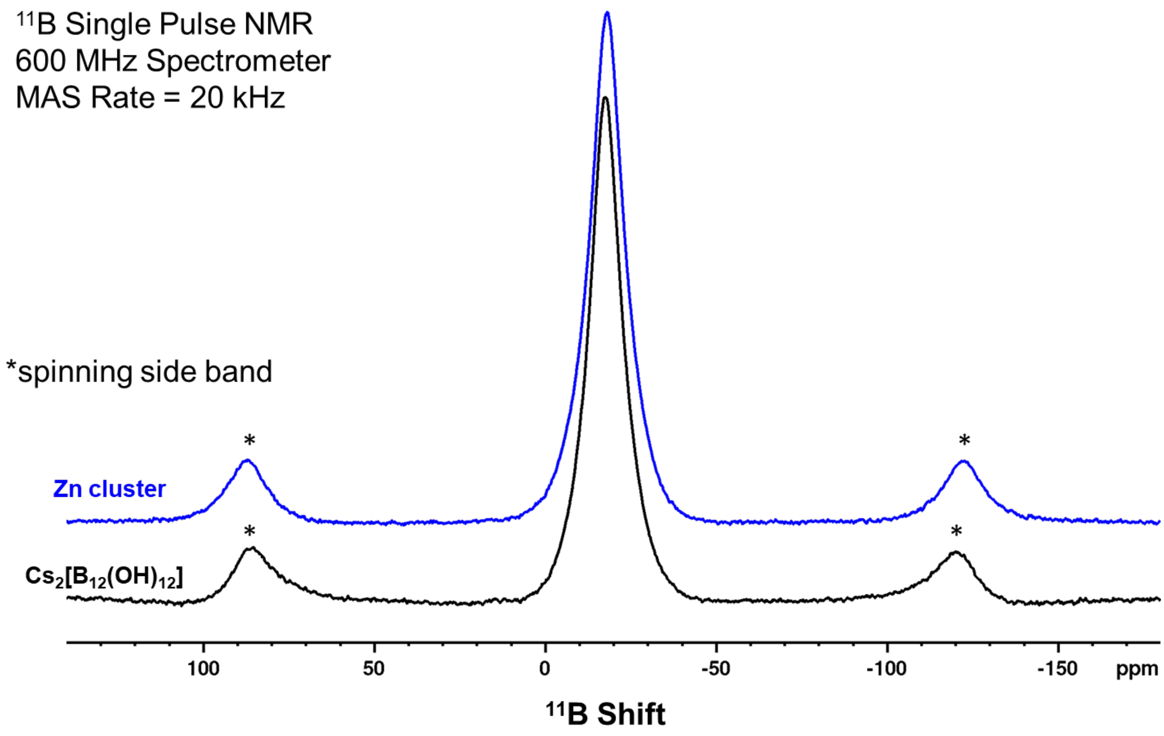

Figure III. 1D solid-state ^{11}B MAS NMR of Zn[$B_{12}(OH)_{12}$] salt.

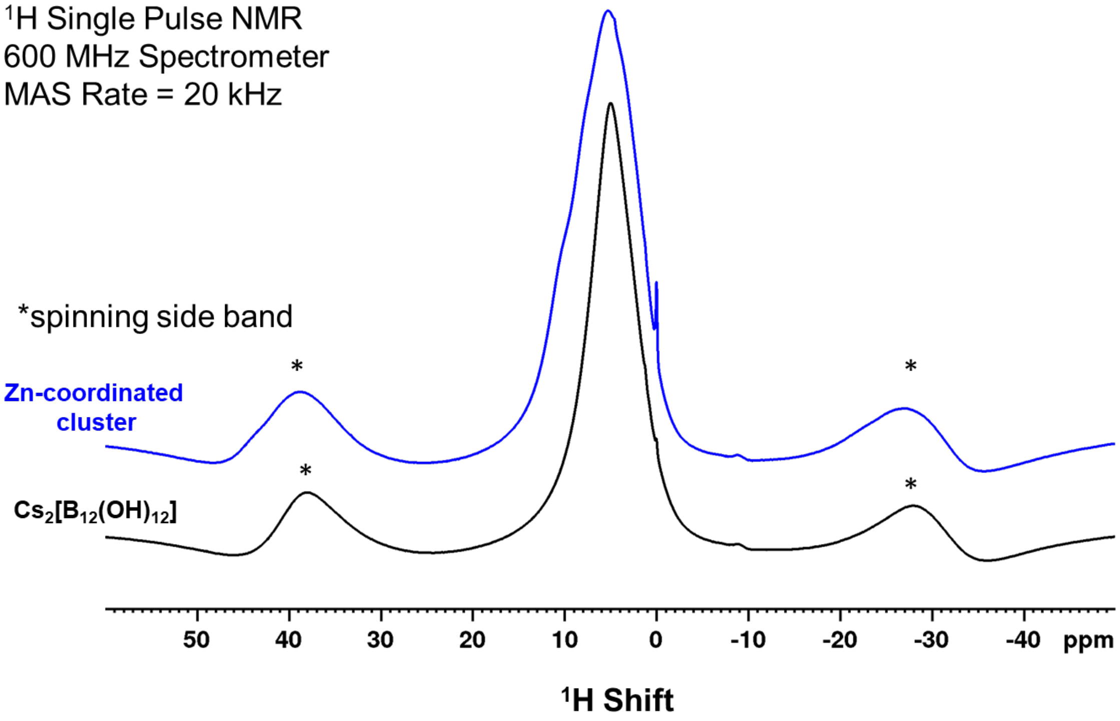

Figure IV. 1D solid-state ^{1}H MAS NMR of Zn[$B_{12}(OH)_{12}$] salt.

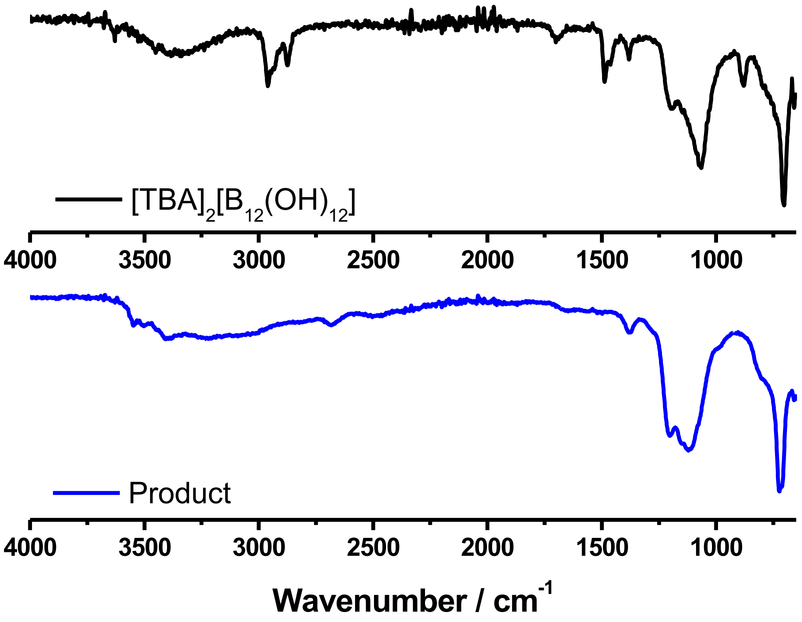

Figure V. FT-IR spectra of [N^{n}Bu$_4$]$_2$[B$_{12}$(OH)$_{12}$] and Zn[B$_{12}$(OH)$_{12}$] salt.

Structural characterization: The structure of Zn[B$_{12}$(OH)$_{12}$] salt was characterized by PXRD, SEM, and SSNMR. The PXRD and SEM results of the material exhibit the highly crystalline nature of the cluster (Fig. I (b) and (c)). The structural refinement was performed from PXRD patterns and revealed that the Zn[B$_{12}$(OH)$_{12}$] salt possesses monoclinic crystal structure (Fig. II and Table I). The 1D solid-state ^{11}B magic-angle-spinning (MAS) NMR confirmed the presence of B$_{12}$-based cluster in 2- oxidation state based on the comparison with reference Cs$_2$[B$_{12}$(OH)$_{12}$] cluster (Fig. III). Moreover, 1D ^{1}H MAS SSNMR detected attached hydroxyl groups to the cluster (Fig. IV). Fourier-transform infrared spectroscopy (FT-IR) spectra also show multiple hydroxyl groups in the cluster, proving the formation of the Zn[B$_{12}$(OH)$_{12}$] salt (Fig. V). TGA was carried out to investigate the thermal stability of the cluster. The result shows a two-step weight loss which can be attributed to the loss of trapped solvent at 220 °C, and decomposition of the cluster at 450 °C (Fig. VI). In order to remove the trapped solvent in the cluster, we activated the material at 220 °C under high vacuum. Interestingly, while the morphology of the cluster maintains the monoclinic crystal structure confirmed by SEM, the X-ray diffraction pattern is significantly changed (Fig. VII and VIII). Further study is necessary to understand the change in PXRD pattern upon activating the cluster.

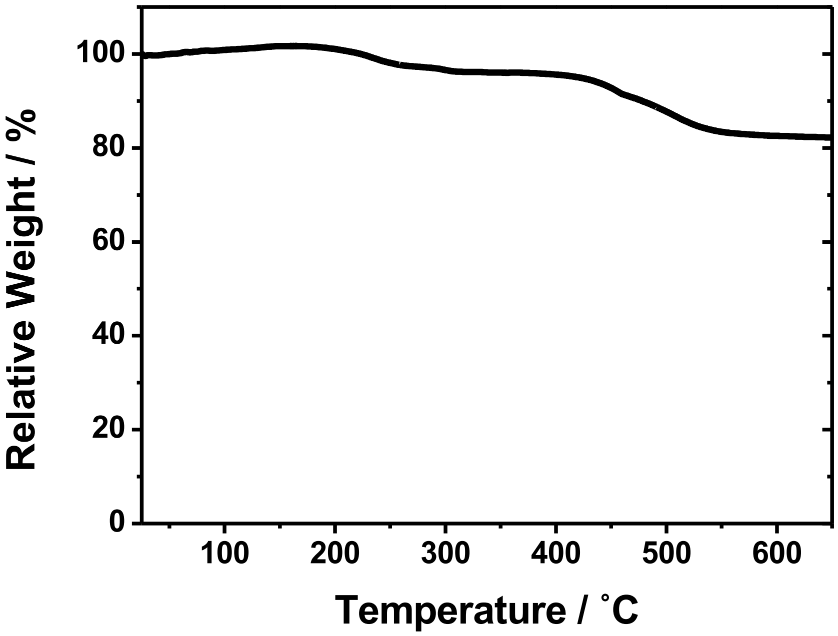

Figure VI. TGA of Zn[$B_{12}(OH)_{12}$] salt.

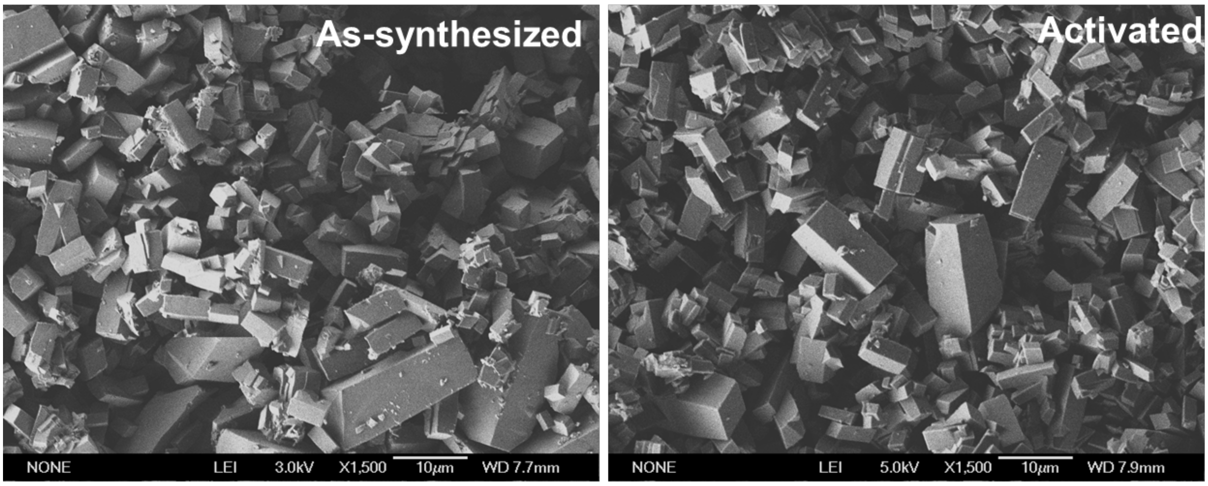

Figure VII. SEM images of as-synthesized (left) and activated (right) Zn[$B_{12}(OH)_{12}$] salt.

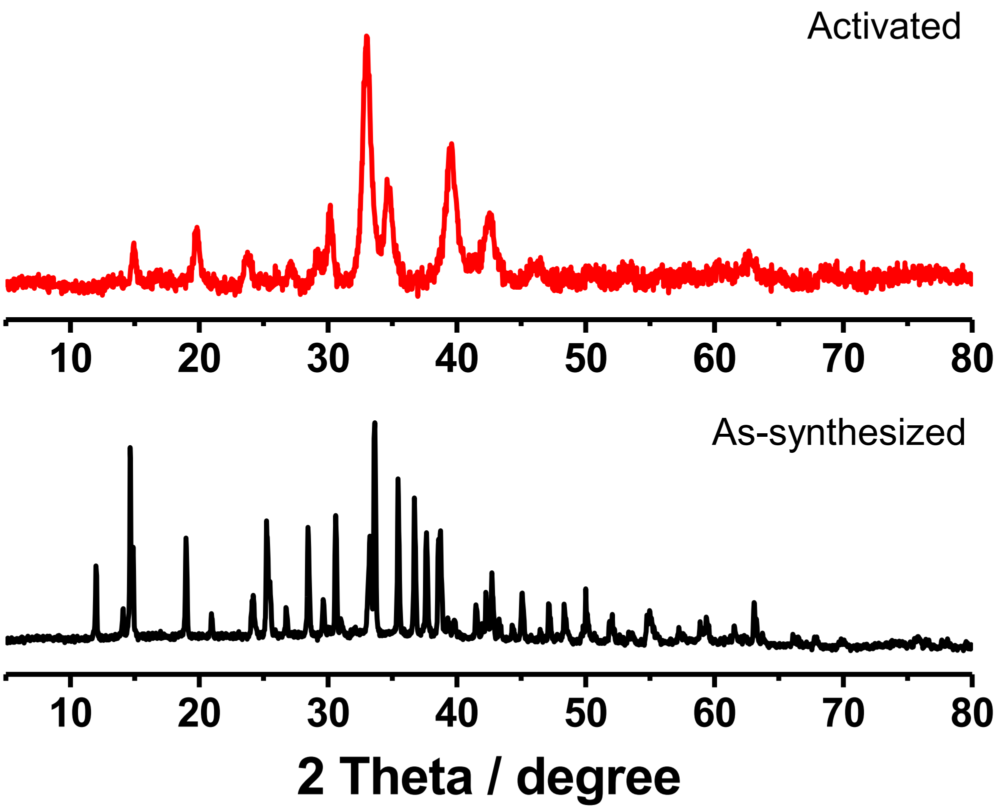

Figure VIII. PXRD patterns of (top) activated and (bottom) as-synthesized Zn[$B_{12}(OH)_{12}$] salt.

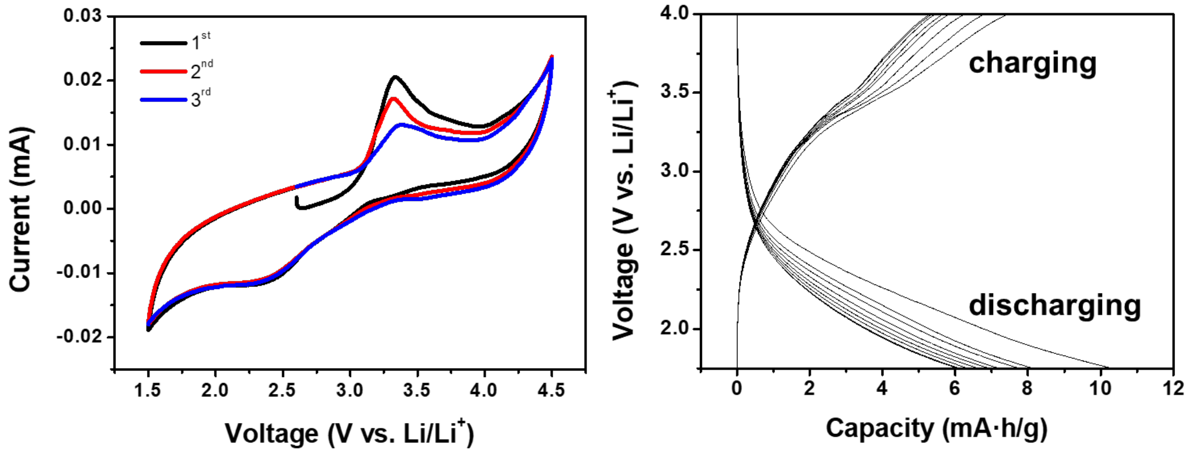

Figure IX. Cyclic voltammogram (left) and galvanostatic charge/discharge curves of Zn[$B_{12}(OH)_{12}$] salt.

Electrochemical property of Zn[$B_{12}(OH)_{12}$] salt:

The measurements of electrochemical properties of metal salts of $[B_{12}(OH)_{12}]^{2-}$ clusters were performed by Andrew Dawson in Professor Sarah H. Tolbert group at University of California, Los Angeles.

We assembled Swagelok-type electrochemical half cells using the B_{12}-based cluster as an active material and $LiPF_6$-based electrolytes. The CV curve of the cluster shows distinct reversible oxidation/reduction features at 3.3 V/2.4 V (Fig. IX (a)). Given the potential redox activity of the cluster, we further performed galvanostatic charge/discharge voltammetry (GV) to investigate the cyclability (Fig. IX (b)). The stable performance was achieved after 5th cycle and the reversible capacity was reached to 5 mA•h/g. While the preliminary data show a promising capability of Zn[$B_{12}(OH)_{12}$] salt as a cathode material for the lithium ion battery, further study on the detailed mechanism involving Li intercalation into the material is necessary.

Synthesis of $Li_2[B_{12}(OH)_{12}]$ cluster: In a pyrex tube, LiCl (71 mg, 1.68 mmol) in deionized water (1.5 ml) was added to a suspension of $Cs_2[B_{12}(OH)_{12}]$ (100 mg, 0.1675 mmol) in deionized water (1.5 ml).[1] The reaction tube was heated at 90 °C in an oil bath for 2 days. The product was recovered as white powder and washed with deionized water three times and vacuum dried on a lyophilizer. The product was further activated in a vacuum oven at 150 °C overnight.

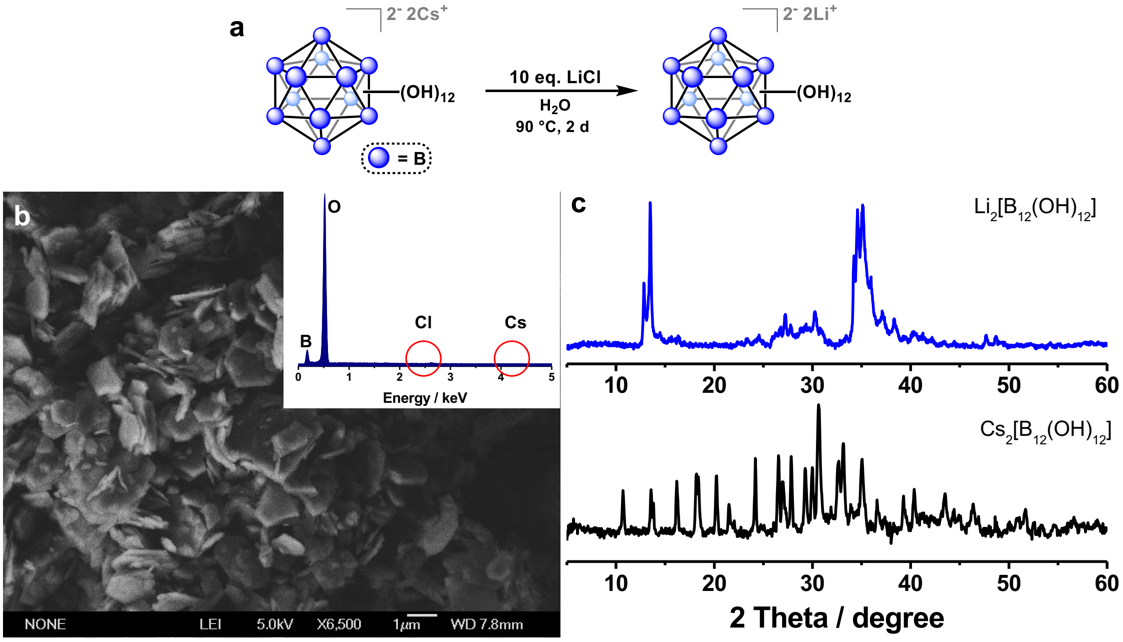

Figure X. (a) Synthetic route to produce $Li_2[B_{12}(OH)_{12}]$ salt.[1] (b) SEM image (inset) EDX results, (c) PXRD of $Li_2[B_{12}(OH)_{12}]$.

Structural characterizations of $Li_2[B_{12}(OH)_{12}]$ cluster: The structure of $Li_2[B_{12}(OH)_{12}]$ salt was revealed by PXRD, SEM, and SSNMR. The SEM image shows a plate-like morphology of $Li_2[B_{12}(OH)_{12}]$ cluster (Fig. X(a)). There were no cesium and chlorine present in the product, suggesting a complete exchange from Cs+ to Li+ (Fig. X(a) inset). The PXRD results suggest crystalline nature of the cluster (Fig. X(b)). The presence of B_{12}-based cluster was confirmed by the 1D solid-state ^{11}B magic-angle-spinning (MAS) NMR based on the comparison with reference $Cs_2[B_{12}(OH)_{12}]$ cluster (Fig. XI). Attached hydroxyl groups to the cluster were detected through 1D ^{1}H SSNMR (Fig. XII). Overall, the combined structural characterization of the product supports the formation of $Li_2[B_{12}(OH)_{12}]$ salt.

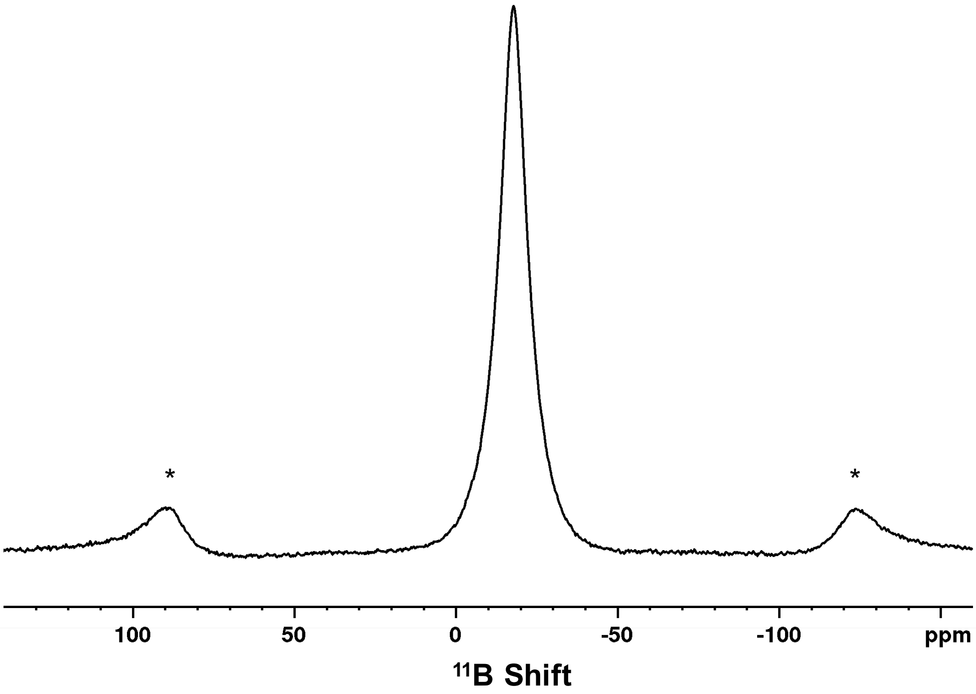

Figure XI. 1D solid-state ^{11}B MAS NMR (b) ^{1}H MAS NMR of $Li_2[B_{12}(OH)_{12}]$ salt.

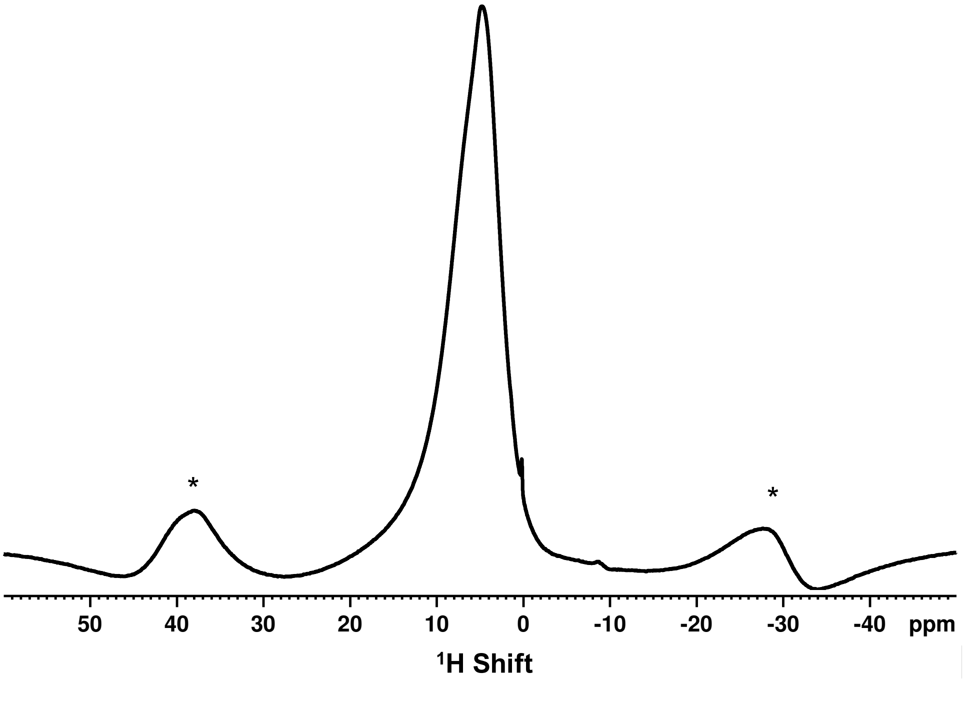

Figure XII. 1D solid-state ^{1}H MAS NMR of $Li_2[B_{12}(OH)_{12}]$ salt.

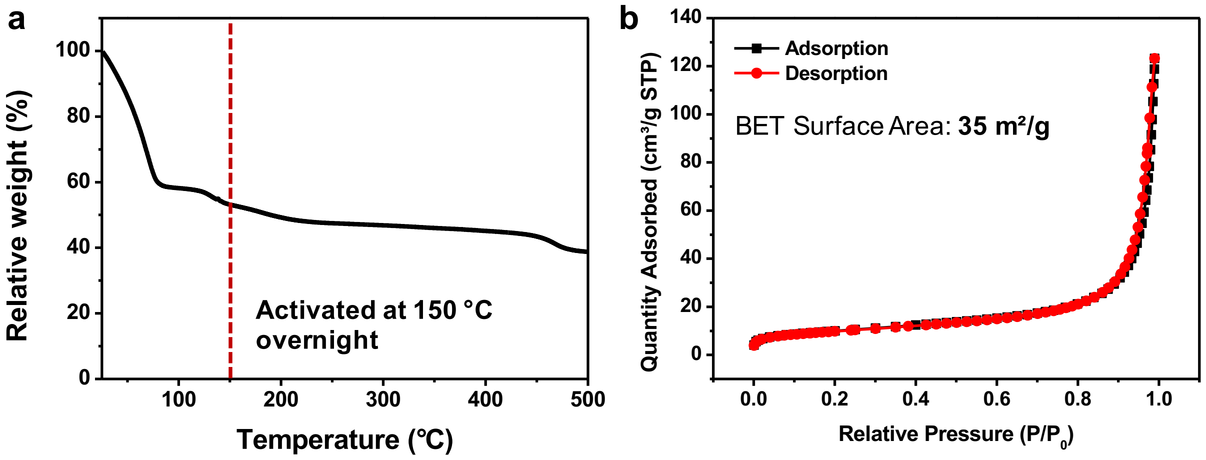

Figure XIII. 1D solid-state ^{1}H MAS NMR of $Li_2[B_{12}(OH)_{12}]$ salt.

The TGA result of $Li_2[B_{12}(OH)_{12}]$ shows a 50 % of mass loss around 100 °C, which can be attributed to the trapped water in the cluster. Therefore, the product was further dried using a vacuum oven at 150 °C overnight and the activated cluster was subsequently used to collect N_2 isotherm at 77 K (Fig. XIII). The calculated surface area from N_2 isotherm is 35 m^2/g. We carried out PXRD on the activated cluster to identify whether the crystallinity remains after removing the trapped solvent. As we previously observed in $Zn[B_{12}(OH)_{12}]$ cluster, the morphology remains similar between as-synthesized and activated clusters by SEM whereas PXRD shows completely different patterns (Fig. XIV and XV). We plan to carry out the structure refinement from PXRD data of the as-synthesized and activated cluster to obtain comprehensive information on the crystal structure.

Electrochemical property of $Li_2[B_{12}(OH)_{12}]$ salt: We assembled Swagelok-type electrochemical half cells using the B_{12}-based cluster as an active material and $LiPF_6$-based electrolytes. We performed galvanostatic charge/discharge voltammetry (GV) to investigate the cycling performance of the as-synthesized and activated cluster (Fig. XVI). While the reversible capacity was only reached to 7 mA·h/g for the as-synthesized cluster, the capacity was significantly improved to 30 mA·h/g in the activated cluster.

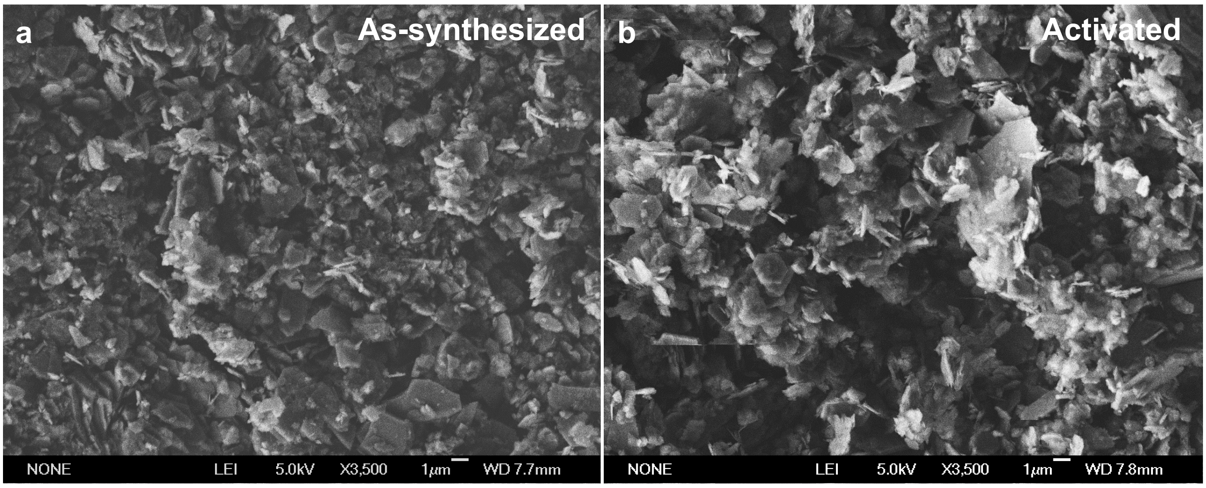

Figure XIV. SEM images of the activated (a) and as-synthesized (bottom) $Li_2[B_{12}(OH)_{12}]$ salt.

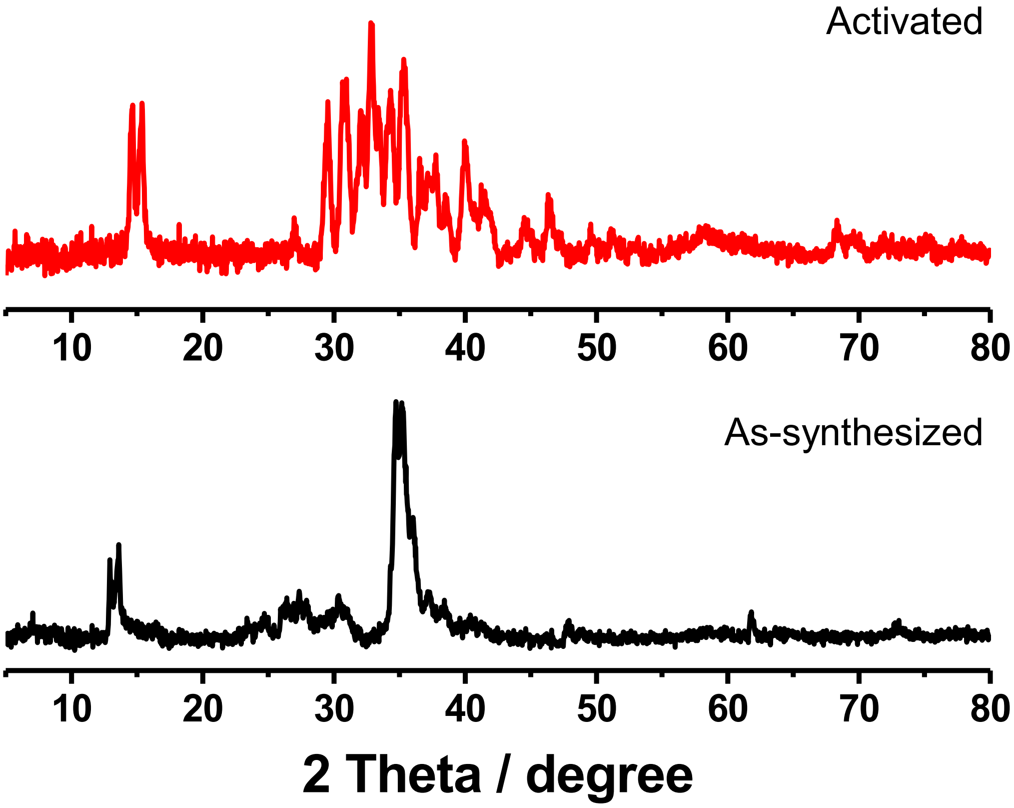

Figure XV. PXRD of the activated (top) and as-synthesized (bottom) $Li_2[B_{12}(OH)_{12}]$ salt.

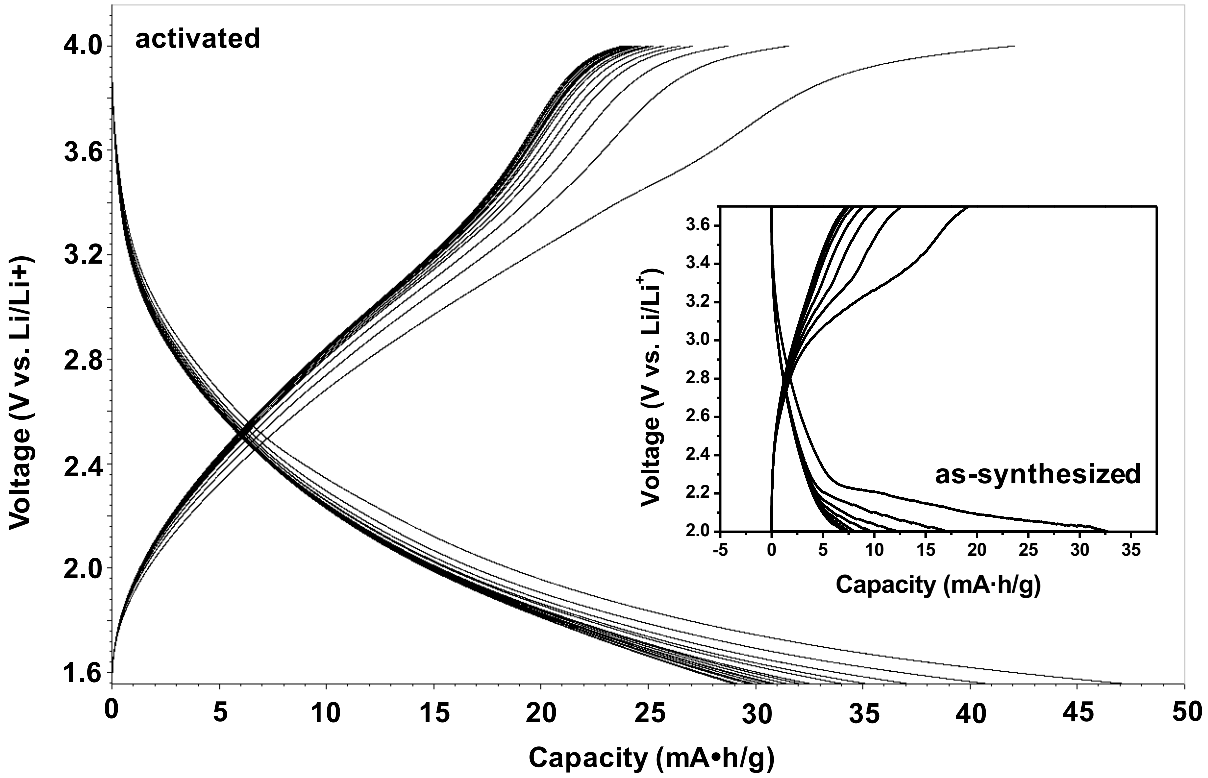

Figure XVI. Galvanostatic charge/discharge curves of the activated and as-synthesized (inset) $Li_2[B_{12}(OH)_{12}]$ salt.

It clearly demonstrates water impurity in the material deteriorates its cycling performance as water can react with both the Li foils and electrolytes.[2-5] In summary, we have reported B_{12}-based cluster as a new class of cathode materials for the lithium ion battery. Further study is necessary to enhance the reversible capacity by incorporating conductive groups into the cluster and also to understand the fundamental aspects of the lithium intercalation in the material.

References:

1. Peymann, T.; Knobler, C. B.; Khan, S. I.; Hawthorne, M. F. *J. Am. Chem. Soc.* **2001**, *123,* 2182–2185.
2. Ren, X.; Wang, J.; Peng, Z.; Lu, L. *Chem. Sci.* **2018**, *9*, 231–237.
3. Li, Y.; Leung, K.; Qi, Y. *Acc. Chem. Res.* **2016**, *49*, 2363– 2370.
4. Zhuang, G.; Ross, P. N.; Kong, F.; McLarnon, F. *J. Electrochem. Soc.* **1998**, *145*, 159–164.
5. Ross, P. N. *Catal. Lett.* **2014**, *144*, 1370–1376.